

NATIONAL & INTERNATIONAL SCIENTIFIC EVENTS

10th International Conference on Computer Technology Applications

Venue: Hotel Ibis Wien Mariahilf
Location: Vienna, Austria

Begins: May 15 2024
Ends: May 17, 2024

12nd World Biomaterials Congress

Venue: EXCO
Location: Daegu, Korea

Begins: May 26 2024
Ends: May 31, 2024

22nd Triennial Congress of The International Ergonomics Association

Venue: Jeju International Convention Center
Location: Jeju Island, Korea

Begins: August 25 2024
Ends: August 29, 2024

18th European Conference on Soil Mechanics and Geotechnical Engineering

Venue: Altice Arena
Location: Lisbon, Portugal

Begins: August 26 2024
Ends: August 30, 2024

13th European Symposium on Martensitic Transformations

Venue: Lecco Campus
Location: Lecco, Italy

Begins: August 26 2024
Ends: August 30, 2024

49th International Conference on Infrared, Millimeter, and Terahertz Waves

Venue: Perth Convention and Exhibition Centre
Location: Perth, Australia

Begins: September 01 2024
Ends: September 06, 2024

38th International Conference on Coastal Engineering

Venue: The Pontifical Gregorian University
Location: Rome, Italy

Begins: September 08 2024
Ends: September 14, 2024

18th European Conference on Games Based Learning

Venue: Aarhus University
Location: Aarhus, Denmark

Begins: 03 October 2024
Ends: 04 October, 2024

69th IEEE Holm Conference on Electrical Contacts

Venue: Graduate Hotel
Location: Annapolis, Maryland, USA

Begins: 06 October 2024
Ends: 10 October, 2024

23rd European Conference on e-Learning

Venue: Universidade Portucalense
Location: Porto, Portugal

Begins: 24 October 2024
Ends: 25 October, 2024

4th International Conference on AI Research

Venue: Universidade Lusófona
Location: Lisbon, Portugal

Begins: 05 December 2024
Ends: 06 December 2024

20th International Conference on Cyber Warfare and Security

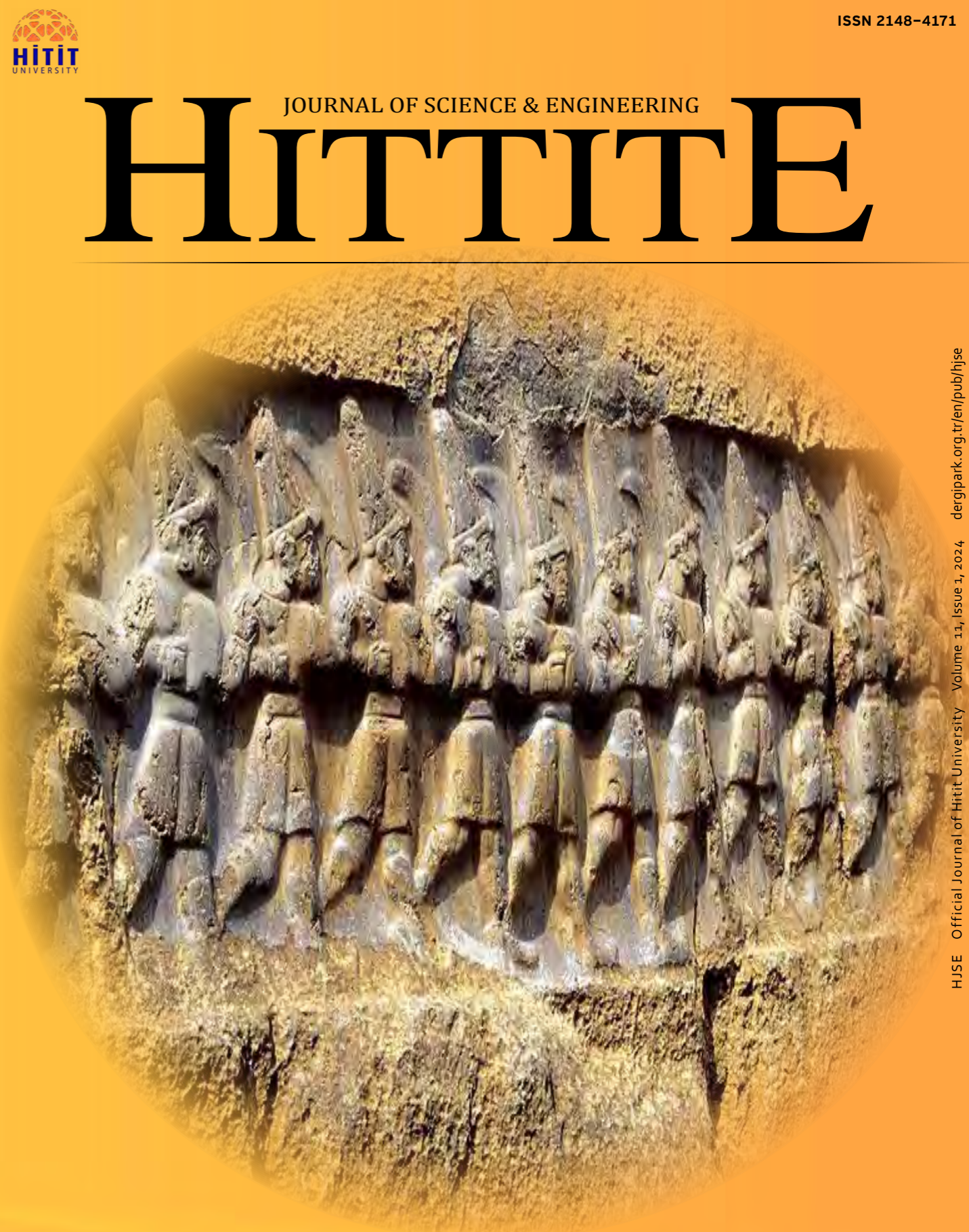
Venue: William & Mary Law School
Location: Williamsburg, Virginia, USA

Begins: March 2025
Ends: March 2025

HITTITE

JOURNAL OF SCIENCE & ENGINEERING

HJSE Official Journal of Hitit University Volume 11, Issue 1, 2024 dergipark.org.tr/en/pub/hjse



HJSE Official Journal of Hitit University Volume 11, Issue 1, 2024 dergipark.org.tr/en/pub/hjse



Abstracted & Indexed in:

TR Dizin Mühendislik ve Temel Bilimler Veri Tabanı | CrossRef | Google Scholar | MIP Database | StuartxChange | ResearchBib | Scientific Indexing Services (SIS)

HITTITE

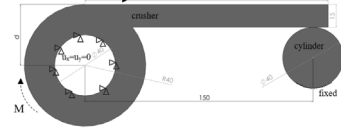
Volume 11, Issue 1, 2024

dergipark.org.tr/en/pub/hjse

Effect of Crusher Arm Position and Surface Friction on the Mechanical Behaviour of a Crusher under Static Conditions 1-6

Mustafa Murat Yavuz

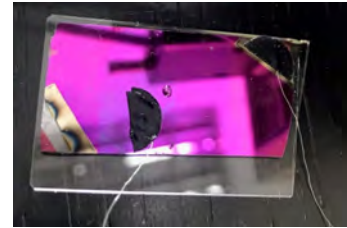
This study examined the connection of the crusher arm at various positions on the shaft and explored variations in stress.



A Fabrication Method for Memristors with Graphene Top Electrodes and their Characterization 7-14

Selin Onay, Omer Refet Caylan, Goknur Buke and Itir Koymen

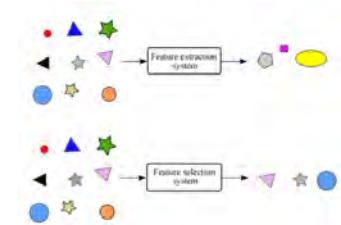
This study reports a novel fabrication method of utilizing graphene as a top electrode in memristive devices.



COVID-19 Diagnosis from Blood Gas Using Multivariate Linear Regression 15-23

Faruk Ayata and Ebubekir Seyyarer

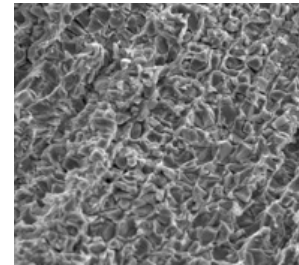
In this study, it is aimed to obtain a function that finds the positive or negative COVID-19 test from the blood gas values of individuals by using Machine Learning methods to contribute to the outbreak management.



Microstructural Evolution and Mechanical Properties of Y Added CoCrFeNi High-entropy Alloys Produced by Arc-melting 25-31

Gökhan Polat and Hasan Kotan

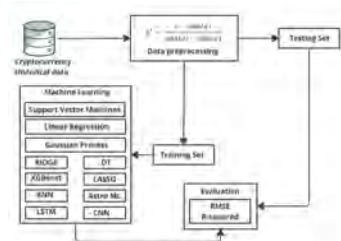
The systematic addition of yttrium (Y) into CoCrFeNi HEA was investigated in the present study to increase the strength by solid solution and second phase strengthening.



A Research: Investigation of Financial Applications with Blockchain Technology 33-40

Mohammed Ali Mohammed and Fuat Turk

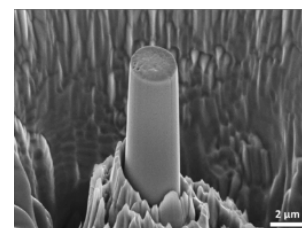
This article delves into applying machine learning techniques for predicting cryptocurrency prices, mainly focusing on Bitcoin, Ethereum, and Binance Coin.



Size Dependent Compressive Strength of FIB Machined Single Crystal Manganese Pillars 41-47

Halil Yılmaz, Bülent Alkan and Hasan Feyzi Budak

The deformation behavior of single crystals of manganese pillars generated by focused ion beam (FIB), with diameters ranging from ~1 nm to ~4.5 μm, has been studied as a function of specimen size using micropillar compression at ambient temperature.



Owner

Prof. Dr. Ali Osman ÖZTÜRK on behalf of
Hitit University

Editor-in-chief

Prof. Dr. Ali KILIÇARSLAN

Associate Editors

Prof. Dr. D. Ali KÖSE
Assoc. Prof. Dr. Öncü AKYILDIZ

Production

Assoc. Prof. Dr. Kazım KÖSE
Res. Asst. Dr. Erhan ÇETİN
Res. Asst. Dr. Mustafa Reşit HABOĞLU
Res. Asst. Harun Emre KİRAN
Res. Asst. Ömer Faruk TOZLU
Lect. Tugrul YILDIRIM

Editor's Office

Tel: +90 364 227 45 33 / 12 36

Fax: +90 364 227 45 35

Email: alikilicarslan@hitit.edu.tr

Subscription Service:

Tel: +90 364 227 45 33 / 12 82

Fax: +90 364 227 45 35

Email: hjse@hitit.edu.tr

EDITORIAL BOARD

Prof. Dr. İftikhar AHMAD

Prof. Dr. Mike BECKETT

Prof. Dr. İbrahim DİNÇER

Prof. Dr. Ali ELKAMEL

Prof. Dr. Mohamad S QATU

Prof. Dr. Saffa RIFFAT

Prof. Dr. Thanos SALIFOLOU

Prof. Dr. Yuehong SU

Dr. Wojciech NOGALA

Prof. Dr. Yusuf AYVAZ

Prof. Dr. Adil DENİZLİ

Prof. Dr. Ali GENÇER

Prof. Dr. Metin GÜRÜ

Prof. Dr. Murat HOŞÖZ

Prof. Dr. Sadık KAKAÇ

Prof. Dr. Tarık Ömer OĞURTANI

Prof. Dr. Ender SUVACI

Prof. Dr. Ali TOPÇU

Prof. Dr. Kazım Savaş BAHÇECİ

Prof. Dr. Cengiz BAYKASOĞLU

Prof. Dr. Naki ÇOLAK

Prof. Dr. Vedat DENİZ

Prof. Dr. Hakan GÜNGÜNEŞ

Prof. Dr. Bülent KABAK

Prof. Dr. Ali KILIÇARSLAN

Prof. Dr. Dursun Ali KÖSE

Prof. Dr. İrfan KURTBAŞ

Prof. Dr. İbrahim SÖNMEZ

Assoc. Prof. Dr. Seyfi ŞEVİK

Prof. Dr. Dilber Esra YILDIZ

University of Malakand, Chakdara, Pakistan

Bangor University, Bangor, United Kingdom

Uoit Ontario University, Ontario, Canada

University of Waterloo, Ontario, Canada

Central Michigan University, Michigan, United States

The University of Nottingham, United Kingdom

Aristotle University of Thessaloniki, Thessaloniki, Greece

The University of Nottingham, United Kingdom

Polish Academy of Sciences, Poland

Suleyman Demirel University, Turkey

Hacettepe University, Turkey

Ankara University, Turkey

Gazi University, Turkey

Kocaeli University, Turkey

TOBB University, Turkey

Middle East Technical University, Turkey

Anadolu University, Turkey

Hacettepe University, Turkey

Hitit University, Turkey

Hitit University, Turkey

Hitit University, Turkey

Hitit University, Turkey

Hitit University, Turkey

Hitit University, Turkey

Hitit University, Turkey

Hitit University, Turkey

Hitit University, Turkey

Hitit University, Turkey

Hitit University, Turkey

Hitit University, Turkey

Journal Name	: HITTITE JOURNAL OF SCIENCE AND ENGINEERING
Year	: 2024
Managing Editor	: Prof. Dr. Ali KILIÇARSLAN
Managing Office	: Hitit University Faculty of Engineering
Managing Office Tel	: +90 364 227 45 33 / 12 36
Publication Language	: English
Publication Type	: Peer Reviewed, Open Access, International Journal
Delivery Format	: 4 times a year (quarterly)
Print ISSN	: 2149-2123
Online ISSN	: 2148-4171
Publisher Address	: Hitit Üniversitesi Kuzey Kampüsü Çevre Yolu Bulvarı 19030 Çorum / TÜRKİYE
Publisher Tel	: +90 364 227 45 33/1236



Hittite Journal of Science and Engineering (HJSE) is published every three months. From January 1, 2024 to March 31, 2024, we have worked very hard and finally published the first issue of year 2024 (2024-Volume 11, Issue 1). As Editor in Chief, I am grateful to all our authors and contributing reviewers of this issue. I also would like to thank to the President of Hitit University, Prof. Dr. Ali Osman Öztürk, for his support and interest in HJSE and to the Associate Editors of HJSE, namely Prof. Dr. Dursun Ali Kose and Assoc. Prof. Dr. Öncü Akyıldız and also the Section Editors of HJSE, namely Prof. Dr. Murat Hoşöz, Prof. Dr. Kazım Savaş Bahçeci, Prof. Dr. Cengiz

Baykasoğlu and Prof. Dr. Akif Akgül as well as our Production Editors, Ömer Faruk Tozlu, Harun Emre Kıran and Hayati Töre for their invaluable efforts in making of the journal.

The good news is that the number of the citations of HJSE from the international journals has been increasing. We have applied for the index of ESCI and database of SCOPUS. We believe that HJSE will be accepted because we don't compromise on quality and work in a very disciplined way.

As Editor in Chief, I would like to thank to the authors submitting their papers to HJSE. In this issue, the articles from the four branches of engineering including "Computer", "Electrical", "Mechanical", and "Metallurgical and Materials" were published. During the first three months of 2024 (January to March), more than the half of the manuscripts submitted to HJSE were rejected based on the reviewers' suggestions. As an Editor in Chief, I always encourage those authors to resubmit their papers after making the required corrections.

I invite the researchers and scientists from all branches of engineering to join us by submitting their original papers for publication in Hittite Journal of Science and Engineering.

Dr. Ali Kiliçarslan

Editor-in-Chief

Effect of Crusher Arm Position and Surface Friction on the Mechanical Behaviour of a Crusher under Static Conditions

Mustafa Murat Yavuz 

 Izmir Democracy University, Mechanical Engineering, Izmir, Türkiye

ABSTRACT

Crushers are utilized to break down or crush various components in industrial applications are subjected to high stresses. The crushing process is carried out by a crusher arm located on the crusher itself. The shape and length of the crusher arm influence the deformation on the arm and the efficiency of crushing process. During the crushing process, stress concentrations occur at the contact regions and especially at the connection location of the crusher arm and the drive shaft. This study examined the connection of the crusher arm at various positions on the shaft and explored variations in stress. Finite element analysis was used in the analyses. The used material is standard steel that behaved elastically. The stresses changed in a way that was not proportional to the movement of the tangential crusher arm towards the center of the shaft. The $d=8$ mm and $d=24$ mm locations are the most suitable places to move the crusher arm rather than the tangential position ($d=40$ mm). The highest stresses occurred at the corners where the shaft and crusher arm connected and formed a stress concentration. The friction effects on the contact surface were also examined and the increased friction coefficient slightly reduced the stress values of the crusher system, but increased the stresses on the crushed object. Only maximum stress levels that are observed at the surface of the beam are mainly considered. The results regarding the crusher arm are discussed in detail.

Keywords:

Crusher; Contact interaction; Deformation; Friction; Sliding distance

INTRODUCTION

Devices that have a motor and a crusher arm mechanism are called a crusher and crusher systems. They use these parts to apply a compressive force and break down objects. Due to surface-to-surface in a limited location or surface-to-point contact, high stresses occur in the crusher arm which can cause fracture. Also these stresses cause deformations in the arm and they must remain within certain limits. The crusher arm is structurally in the beam profile and bending is the most dominant condition that happens during crushing. In the literature, there are different application trials for the solution of bending beam problem. Reinforced recycled concrete beams [1] were analyzed under bending which showed lower compressive strength and modulus of elasticity than normal concrete. A function was expressed between the compressive strength of recycled concrete and Young's modulus. Wang [2] theoretically calculated the appropriate suspended roof length for a

roof. Optimum placement distances of roof hanging slots were determined by considering the weight of the beam. The most suitable cell profile against impact [3] was investigated in different cell structures formed in square tubes. A bending moment occurred due to the inclined plane having different angles used in impact. The energy absorption of a steel plate system [4] was investigated using the finite element method and it was found that most of the absorbed energy was bending energy. In a study transverse ice breaking under crushing and bending conditions, results of force/moment [5] were given. The crush response of two nested rectangular pipes under lateral compression [6-8] was investigated. Crushing load varied according to the area occupied by the plastic zone, tube thickness and yield stress of the material. Zhang et al. [9] investigated rectangular tubing which was fabricated by bending of aluminum sheets under axial crushing. The overlapping plates used in the

Article History:

Received: 2023/02/08

Accepted: 2023/12/19

Online: 2024/03/31

Correspondence to: Mustafa Murat Yavuz,
Izmir Democracy University, Mechanical
Engineering, 35140, Izmir, TÜRKİYE
E-Mail: murat.yavuz@idu.edu.tr;
Phone: +90 232 260 1001;
Fax: +90 232 260 1004.

This article has been checked for similarity.



This is an open access article
under the CC-BY-NC licence

<http://creativecommons.org/licenses/by-nc/4.0/>

Cite as:

Yavuz MM. Effect of Crusher Arm Position and Surface Friction on The Mechanical Behaviour of a Crusher Under Static Conditions. Hittite Journal of Science and Engineering 2024; 11(1):1-6. doi:10.17350/hjse19030000325

tube increased the absorbed energy but caused uneven buckling. The clamped boundary condition solved that problem. Crushing behavior of CF/EP composites [10] were analyzed under quasi-static and dynamic conditions. In the quasi-static analysis, bending, an important factor of the damage mechanism, was found dominant. The average crushing force of multistage nested rectangular tubes [11] was analyzed, and the use of more stages resulted in better crush performance and energy absorption. When the number of stages or cells used [12] was increased, the crash-resistance properties were improved. Energy absorption and crushing performance of capped cylindrical tubes [13] were analyzed under oblique impact which showed better energy absorption performance than standard cylindrical tubes. The samples containing concrete and timber in the steel column tubes were tested for their stability under crushing [14]. The location of loading affected material loading capacity. An axial compression load [15] was applied to corrugated tubes containing carbon fiber reinforced polymer (CFRP) and Kevlar fiber-reinforced polymer (KFRP) composites and having conical angles of 35°, 40°, 45°, 50° and 55°. Similar crushing behavior was observed between KFRP and CFRP composites and 50° conical angle has the best energy absorption behavior. The mechanical behavior of the lattice cylindrical shells under compression [16] was investigated and negative Poisson ratio was observed. Energy absorption capacity was increased 20% between 4 different trials. Transverse bending of thin-walled beams [17] was analyzed without considering various shapes/dimensions and fixed boundary conditions. The used three-point bending analysis results showed that loading angle and position affect the deformation modes. In studies carried out on crushers that have a conical structure rather than a beam structure, heat treatment [18] was applied on a cone crusher surface to increase the resistance to abrasion. Gyrotory crusher torque analysis [19] was analyzed with discrete element method and found that large particles cause to decrease the crushing torque. Another study [20] analyzed the concave curve height, curve radius, and shaft speed of a gyrotory crusher to optimize its geometrical parameters. Frequency [21] for a vibratory crusher, rotor parameters [22] for a crusher-shredder, hammers, and knives [23] on rotor for crushing were investigated. Rotor parameters and hammer shape were found to be the most important design criteria. Discrete element method [24] was used to examine new hammer designs for laboratory-scale jaw crusher and new designs have been found less effective than existing designs. Thus, time/money savings were achieved by not producing industrial sized devices. Investigating single and double rotor impact crushers through the discrete element method [25] revealed that enhancing crushing efficiency is achieved by employing double rotors and ele-

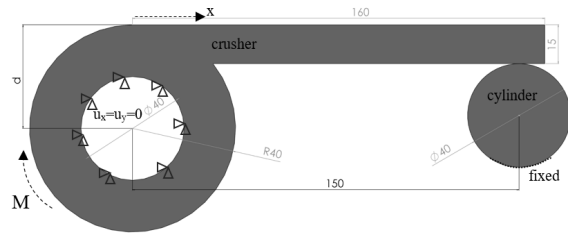


Figure 1. Geometrical model of crusher and cylinder and dimensions (in mm).

minating the rotation speed of the rotor. A general used model for crushing process has not been developed, Mishchuk et al. [26] investigated for five different crushing machines by considering destruction energy of materials. They detected that many tries into the mathematical modeling of material fracture have faced considerable challenges. The review of literature highlighted a deficiency in relevant research concerning a beam constructed on the drive shaft.

In this study, the position of the crusher arm on the shaft body and the surface friction coefficient were examined, stress and deformations were given. The study may contribute to the same or beam-shaft connection studies in the literature.

MATERIAL AND METHODS

The crusher system consists of a crusher arm and the part to be crushed and are shown in Fig. 1. The arm that crushes the material is made of beam is connected to a hollow shaft. The inner part of the shaft is defined as the cylindrical boundary condition that allows only rotational. The boundary condition defined for the rotation of the shaft around a fixed axis is also used in similar studies in the literature [27]. A torque of 1000 Nm is applied to the shaft in a clockwise direction. The piece to be broken has a circular geometry and is mounted in contact with the crusher arm. The bottom surface of the circular piece is fixed. The fixing location is sufficiently far from the contact location. Contact surfaces were defined as friction surfaces and the friction coefficient was determined as 0.3. The position of crusher arm is defined as d is shown in Fig. 1. It is the distance between the outer surface of the crusher arm and the center of the shaft. Different d values have been investigated in the study.

Finite element model of the crusher system was shown in Fig. 2 which was created to include uniform finite element distribution. There are approximately 30,000 finite elements in each model. The aspect ratio of the elements is very close to 1 and high-quality element structure is formed. The model was created with the plane stress condition in 2D with unit thickness. Standard steel ($E=200$ GPa, $\nu=0.3$) was chosen as the material.

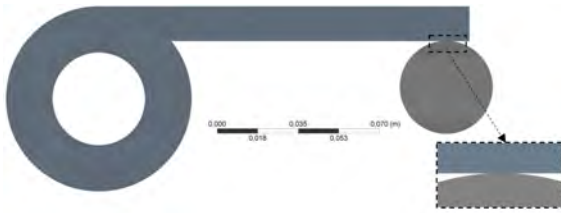


Figure 2. Finite element model of crusher and cylinder.



Figure 3. Finite element model of a cantilever beam.

A validation study was conducted to determine the solution precision and accuracy of the finite element model. Since the bending behaviour is dominant, a cantilever beam problem has been investigated and its model is shown in Fig. 3. One of the short sides of the cantilever beam is fixed and a pure moment of 10 Nm is applied to the other free edge. Cantilever beam has a length of 100 mm and height of 10 mm. The bending stress was [28] given in Eq. 1 for this validation case. The applied moment is represented as M , the distance between the geometric center and the upper/lower surface is represented as c and the moment of inertia is represented as I for the rectangular section.

$$\sigma = \frac{M \times c}{I} \quad (1)$$

The stresses in the crusher are given in the form of Von-Mises stresses [28-29] in Eq. 2. The stresses on the right side of the equation are the principal stresses.

$$\sigma_{VM} = \sqrt{\sigma_1^2 - \sigma_1\sigma_2 + \sigma_2^2} \quad (2)$$

RESULTS AND DISCUSSION

The analytical solution of validation case is given in Eq. 3. and the result obtained for the finite element analysis is shown in Fig. 4. The calculated analytical result and the results obtained from the finite element analysis are consistent with each other. The crusher system was modelled and examined using this element structure.

$$\sigma = \frac{M \cdot c}{I} = \frac{10\text{Nm} \cdot 0.005\text{m}}{\frac{1}{12} \times 1 \times (0.01\text{m})^3} = \pm 0.6\text{MPa} \quad (3)$$

In Fig. 5, the maximum Von-Mises stresses in the crusher system with respect to crusher arm distance (d) are



Figure 4. Bending stress of cantilever beam (in MPa).

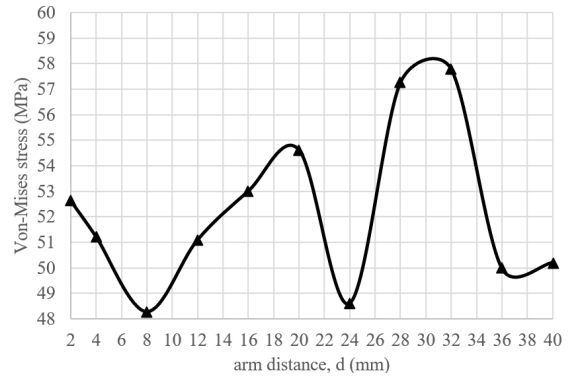


Figure 5. Crusher arm distance (d) and stresses in the system (MPa).

shown. At the farthest distance ($d=40$ mm) where the breaker arm is tangential to the shaft, the stress value is 50,198 MPa. Stress concentration occurs locally at the corner of the breaker arm and shaft connection. When the crusher arm was brought a little closer to the shaft center (from $d=40$ mm to $d=36$ mm), the stress value decreased slightly. As the arm that breaks the material approached the center of the hollow shaft, the connection location where the shaft and the arm meet became less acute. Stress values increased by 15% between $d=36$ mm and $d=32$ mm results. In this layout, the center of the cylindrical part and the center of the shaft are in approximately the same vertical position. The highest stress value is observed in the result with $d=32$ mm. There is a sharp stress reduction observed at $d=24$ mm results. Sharp corners turned into two normal connection corners. The lowest stress value was obtained at $d=8$ mm and then at $d=24$ mm. Geometric nonlinearity is quite dominant in stress values.

Considering the stress contours in Fig. 6, the highest stresses occurred at the corners where the crusher arm and the shaft are connected, and on the upper and lower surfaces of the crusher arm. The stress contour values are labeled as H++, H+, H, L and L- from highest to lowest. The highest stress (H++) locations occur at the connection corners in all cases. When the crusher arm is approaching to the centre of shaft (from $d=40$ mm to $d=32$ mm), H+ stress location vanishes at the upper surface of the crusher arm. H+ location at the below surface of the crusher arm concentrates in a smaller area. Therefore, the stress value at $d=32$ mm is higher than the other cases. H+ contours appear at the upper surface of the crusher arm in $d=24$ mm results that causes to decrease the stresses at the lower surface. At the $d=2$ mm result, two H++ stress locations are observed. This stress distribution is similar the stress distribution of a cantilever beam under bending.

The stresses occurring on the upper surface of the crusher arm are shown in Fig. 7. Stress concentration have occurred at the $x=0$ m location, where the crusher arm connects with the shaft. In the results of $d=40$ mm, stress values

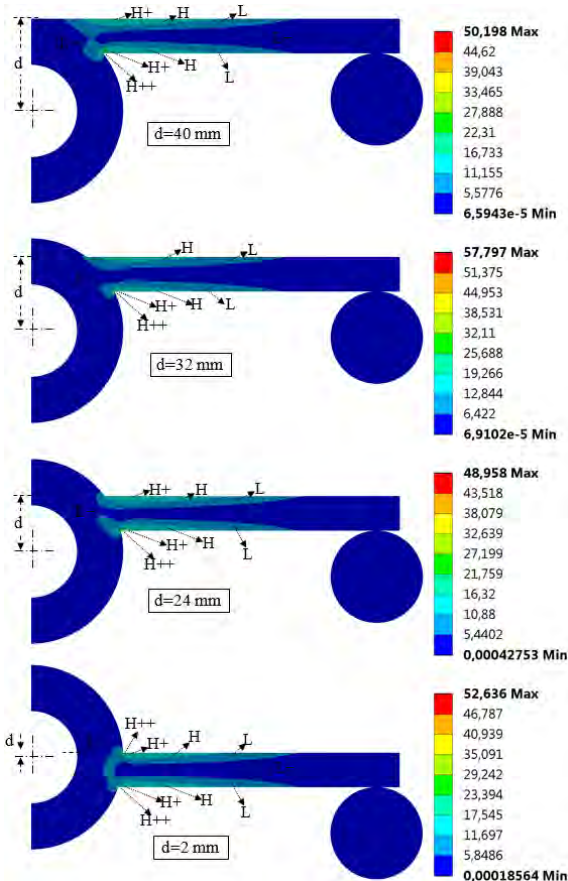


Figure 6. Von-Mises stress (in MPa) contours for $d=40, 32, 24$ and 2 mm.

are not high at $x=0$ m. This is caused by the fact that the crusher arm of the $d=40$ mm model is completely tangential to the shaft outer surface. There is no formation of a protrusion at the $x=0$ m. As a result of the decrease in the d distance of the crusher arm, the crusher arm approach towards the center of the shaft created a protrusion on the connection location between the shaft and the upper surface of the crusher arm. A stress concentration occurs at $x=0$ m with the effect of protrusion. The highest stresses after $x=0$ m range from 18 to 19 MPa. The stress value decreased as the d value decreased.

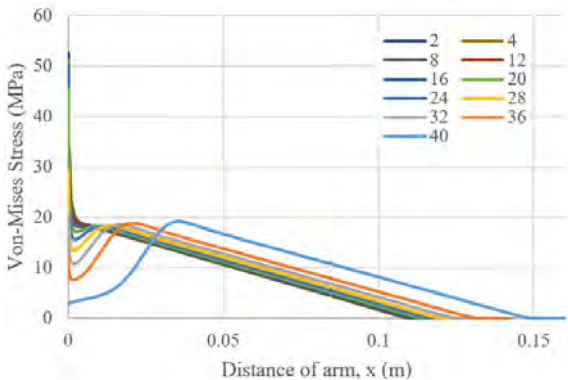


Figure 7. Von-Mises stresses on the upper surface of the crusher arm at different d distance.

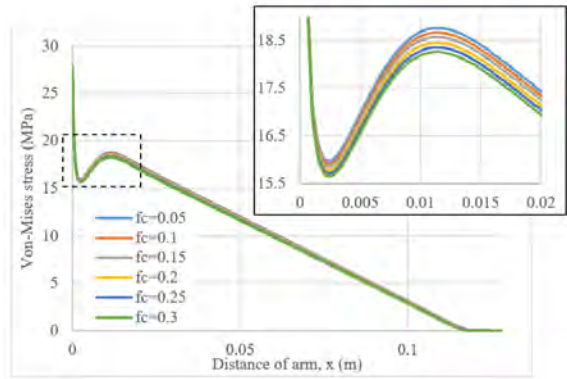


Figure 8. Effect of f_c on Von-Mises stresses of $d=24$ mm model at upper surface.

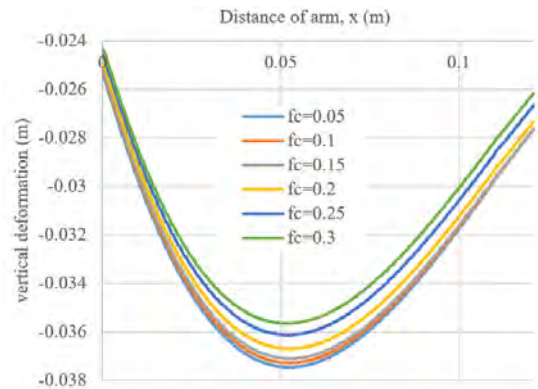


Figure 9. Vertical deflection results on the lower surface of the crusher arm for the $d=24$ mm model.

In Fig. 8, the effect of friction coefficient (f_c) is shown for the $d=24$ mm crusher arm model. The results are taken from upper surface of the crusher arm. It has been observed that increasing friction coefficient reduces stresses. A magnified view is also added at the protrusion location. Increasing the f_c from 0.05 to 0.3 decreased the stresses by 2.6%. The stress distribution does not change much as different f_c values. The effect of f_c on the vertical deflection results are shown in Fig. 9 for the $d=24$ mm model. The highest deflection occurred in the middle of the crusher arm. Deflection results are reduced when the friction coefficient (f_c) increases.

The stress and support reactions are shown in Table 1 at different coefficients of friction for the $d=24$ mm model. The reaction forces (f_x, f_y) that occur where the crushed part is fixed are shown. Same magnitudes of these reaction forces occur at the cylindrical boundary conditions of the shaft, but opposite direction. The reaction moment acts to prevent the rotation of the object that is being crushed. As the friction coefficient increased, the horizontal force and the stress values on the cylinder increased, and this had a positive effect on the crushing situation. The stress in the crusher decreased with increasing friction coefficient.

Table 1. Stress and reaction responses for d=24 mm model.

fc	stress in system (MPa)	stress in cylinder (MPa)	force rea. Fx (N)	force rea. Fy (N)	moment rea. Ma (Nm)
c	50.5	4.69	-312.28	6649.0	11.89
0.1	50.1	4.74	-621.27	6630.4	23.76
0.15	49.8	4.81	-928.47	6612.0	35.55
0.2	49.3	4.95	-1320.6	6588.4	50.60
0.25	49.0	5.13	-1643.6	6569.0	63.00
0.3	48.6	5.33	-1966.3	6549.6	75.38

CONCLUSION

This study examined how the location of the arm and the coefficient of friction on the surface affected a system that crushes materials. Finite element method was used, and stresses, deflection and reaction forces formed under the effect of constant moment were given. In the results obtained;

- Due to the moment applied to the breaker, mainly bending stress has occurred in the breaker arm.
- Sharp corners at the connection locations of the crusher arm and shaft has the highest stress locations.
- The absence of sharp corner on the upper surface of the crusher arm caused the least stress formation at the upper surface (in d=40 mm case)
- Moving the tangentially crusher arm (d=40 mm) towards the d=8 mm and d=24 mm locations reduces the stresses.
- Increasing the friction coefficient increases the horizontal reaction force and the stress in the crushed part while decreases the total stress value of the crusher system and vertical deflection of the crusher arm.

CONFLICT OF INTEREST

The author declares no conflict of interest.

References

1. Sato R, Maruyama I, Sogabe T, Sogo M. Flexural behavior of reinforced recycled concrete beams. *Journal of Advanced Concrete Technology*. 2007;5(1):43-61.
2. Wang K. Study of reasonable hanging roof length on hard roof. *Procedia Engineering*. 2011;26:772-77.
3. Tran T, Hou S, Han X, Nguyen T, Chau M. Theoretical prediction and crashworthiness optimization of multi-cell square tubes under

- oblique impact loading. *International Journal of Mechanical Sciences*. 2014;89:177-193.
4. Dong H, Gao G, Chen X, Guan W, Zou X. Crushing analysis of splitting-bending steel plate energy absorber under axial loading. *International Journal of Mechanical Sciences*. 2016;110:217-228.
5. Zhou L, Riska K, Ji C. Simulating transverse icebreaking process considering both crushing and bending failures. *Marine Structures*. 2017;54:167-87.
6. Tran T. A study on nested two-tube structures subjected to lateral crushing. *Thin-Walled Structures*. 2018;129:418-28.
7. Mohsenizadeh S, Ahmad Z. Auxeticity effect on crushing characteristics of auxetic foam-filled square tubes under axial loading. *Thin-Walled Structures*. 2019;145(106379):1-21.
8. Li J, Gao G, Yu Y, Guan W. Experimental and numerical study on splitting process of circular steel tube with enhanced crashworthiness performance. *Thin-Walled Structures*. 2019;145(106406):1-11.
9. Zhang X, Zhang H, Ren W. Axial crushing of tubes fabricated by metal sheet bending. *Thin-Walled Structures*. 2018;122:252-263.
10. Chen Y, Ye L, Escobedo-Diaz JP, Zhang Y, Fu K. Quasi-static and dynamic progressive crushing of CF/EP composite sandwich panels under in-plane localised compressive loads. *Composite Structures*. 2019;222(110839):1-11.
11. Tran T, Le D, Baroutaji A. Theoretical and numerical crush analysis of multi-stage nested aluminium alloy tubular structures under axial impact loading. *Engineering Structures*. 2019;182:39-50.
12. Wu Y, Fang J, Cheng Z, He Y, Li W. Crashworthiness of tailored-property multi-cell tubular structures under axial crushing and lateral bending. *Thin-Walled Structures*. 2020;149(106640):1-22.
13. Reddy KY, Kumar AP, Nagarjun J. A computational study on the crushing behaviour of aluminium capped cylindrical tubes subjected to oblique load. *Materials Today: Proceedings*. 2020;27:1923-27.
14. Ghanbari-Ghazijahani T, Nabati A, Azandariani MG, Fanaie N. Crushing of steel tubes with different infills under partial axial loading. *Thin-Walled Structures*. 2020;149(106614):1-14.
15. Alkhatib F, Mahdi E, Dean A. Crushing response of CFRP and KFRP composite corrugated tubes to quasistatic slipping axial loading: Experimental investigation and numerical simulation. *Composite Structures*. 2020;246(112370):1-16.
16. Guo Y, Zhang J, Chen L, Du B, Liu H, Chen L, Li W, Liu, Y. Deformation behaviors and energy absorption of auxetic lattice cylindrical structures under axial crushing load. *Aerospace Science and Technology*. 2020;98(105662):1-11.
17. Huang Z, Zhang X, Fu X. On the bending force response of thin-walled beams under transverse loading. *Thin-Walled Structures*. 2020;154(106807):1-10.

18. Allende-Seco R, Artigas A, Bruna H, Carvajal L, Monsalve A, Sklate-Boja MF. Hardening by transformation and cold working in a hadfield steel cone crusher liner. *Metals*. 2021;11(6):961.
19. Moncada M, Toledo P, Betancourt F, Rodríguez CG. Torque analysis of a gyratory crusher with discrete element method. *Minerals*. 2021;11(8):878.
20. Chen Z, Wang G, Xue D, Cui D. Simulation and optimization of crushing chamber of gyratory crusher based on the DEM and GA. *Powder Technology*. 2021;384:36–50.
21. Mishchuk YO, Nazarenko II, Mishchuk DO, Definition of rational operating modes of a vibratory jaw crusher. *Naukovyi Visnyk Natsionalnoho Hirnychoho Universytetu*. 2021;4:56-62.
22. Astanakulov K, Karshiev F, Gapparov S, Khudaynazarov D, Azizov S, Mini crusher-shredder for farms. *E3S Web of Conferences, Conmechhydro*. 2021;264(04038):1-8.
23. Tamborrino A, Perone C, Veneziani G, Berardi A, Romaniello R, Servili M, Leone A. Experimental investigation of a new modular crusher machine developed for olive oil extraction plants. *Foods*. 2022;11:3035.
24. Doroszuk B, Król R. Industry Scale optimization: hammer crusher and dem simulations. *Minerals*. 2022;12:244.
25. Bwalya MM, Chimwani N. Numerical simulation of a single and double-rotor impact crusher using discrete element method. *Minerals*. 2022;12:143.
26. Mishchuk YO, Nazarenko II. Analysis of the energy laws of material destruction. *Strength of Materials and Theory of Structures*. 2023;110:294-315
27. Trahair NS. Non-linear biaxial bending of steel Z-beams. *Thin-Walled Structures*. 2018;129:317–26.
28. Budynas R, Nisbett K. *Shigley's mechanical engineering design* 11th Edition, McGraw Hill; 2020.
29. Young WC, Budynas RG. *Roark's formulas for stress and strain*, Seventh Edition, McGraw-Hill; 2002.

A Fabrication Method for Memristors with Graphene Top Electrodes and their Characterization

Selin Onay^{1,2}  Omer R. Caylan^{2,4}  Goknur Buke³  İtir Köymen^{1,2*} 

¹ TOBB University of Economics and Technology, Department of Electrical and Electronics Engineering, Ankara, Türkiye.

² Bilkent University, UNAM Institute of Materials Science and Nanotechnology, Ankara, Türkiye.

³ TOBB University of Economics and Technology, Micro and Nanotechnology Graduate Program, Ankara, Türkiye.

⁴ TOBB University of Economics and Technology, Department of Materials Science and Nanotechnology Engineering, Ankara, Türkiye.

ABSTRACT

In recent years, there has been extensive research on the memristor, a non-volatile memory device that demonstrates effective emulation of biological synapses. The implementation of graphene as a top electrode in memristive switching systems presents an intriguing alternative to conventional materials such as Platinum. Graphene, as a carbon-derived material, possesses a remarkable area- to-volume ratio, biocompatibility, adsorption capabilities, and high electrical conductivity and thereby offers a promising avenue for the fabrication of biosensors with superior characteristics. This study reports a novel fabrication method of utilizing graphene as a top electrode in memristive devices. Characterization results of micrometric devices as well as larger memristive devices are also discussed. Larger devices show promising results to be used as memristive sensors. Microstructures have been fabricated successfully through developing a process flow and patterning graphene using photolithography and lift-off. E-beam evaporation and sputtering were used for depositing bottom metal electrodes and active layer respectively. Graphene was produced using the chemical vapor deposition (CVD) method and subsequently transferred using the fishing technique. Ultimately Pt/TiO₂/TiO_x/Graphene memristive devices were fabricated.

Keywords:

Memristor; Graphene; Device fabrication; Graphene patterning; Device characterization

INTRODUCTION

The memristor has been introduced as the fourth basic circuit element in 1971, by Leon Chua. It was noted that there are six different mathematical relations that connect pairs of the four fundamental circuit variables: electric current (i), voltage (v), charge (q), and magnetic flux (Q) (1). One of the relationships mentioned (the charge is the time integral of the current) is derived from the definitions of two of the variables mentioned. Another relationship (the flux is the time integral of the electromotive force, or voltage) is determined by Faraday's law of induction (2). The memristor (a contraction for memory resistor) is an electronic component with two terminals that can change its resistance and was invented based on the principle of symmetry. The memristor links electrical charge and magnetic flux.

With the development of big data analytics (BDA) (3), the internet of things (IoT) (4), and artificial intelligence technology (5), a demand for cutting-edge elect-

ronic devices and systems has emerged (6). To function optimally, these systems need to be very power efficient, have a well-designed computer architecture, and be able to process data quickly. There has been significant research interest in memristors and memristive devices over the past decade due to their potential use as non-volatile memory applications (7) and their applications in non-traditional computing (8).

A memristor traditionally consists of a stack of metal, dielectric, and metal layers. The way that a memristor functions relies on the formation and rupture of conductive filament (CF) with defects in the sandwich layer between the two metallic electrodes (9). Once the CF has been formed within a memristor device, the device is able to switch between a high-resistance state (HRS) and a low-resistance state (LRS) in a reversible manner (10). Memristors can be categorized as cation devices, anion devices, and dual ionic devices based on the type of mobile species and migration behavior (11).

Article History:

Received: 2023/09/12

Accepted: 2024/02/22

Online: 2024/03/31

Correspondence to: İtir Köymen,

E-mail: ikoymen@etu.edu.tr;

Phone: +90 312 292 6900.

This article has been checked for similarity.



This is an open access article under the CC-BY-NC licence

<http://creativecommons.org/licenses/by-nc/4.0/>

Cite as:

Onay S, Caylan OR, Buke G, Köymen İ. A Fabrication Method for Memristors with Graphene Top Electrodes and their Characterization. Hittite Journal of Science and Engineering 2024;11(1):7-14. doi:10.17350/hjse19030000326

The conduction path in the fabricated devices is made up of a metal that has undergone chemical reduction, resulting in a lower valence state. This conduction path can be viewed as consisting of oxygen vacancies that act as n-type dopants.

Memristive devices are commonly sandwich like structures with two conductive electrodes separated by an active layer. The first reported memristor prototype employed Platinum (Pt) electrodes and a stoichiometric and doped Titanium oxide ($\text{TiO}_2/\text{TiO}_x$) active layer (2) this structure remains popular (12). Other examples include gold (Au) electrodes with Zinc Oxide (ZnO) active layer (13), Indium Tin Oxide (ITO) bottom electrodes, Zirconium Oxide (ZrO) active layer and Silver (Ag) top electrodes (14), polyvinylpyrrolidone active layer with Ag electrodes (15), hafnium oxide active layer with Pt electrodes (16). The devices fabricated in this work have an active layer that consists of stoichiometric TiO_2 and doped TiO_x , the bottom electrode is Pt and the top electrode is Graphene.

Graphene has garnered considerable attention due to its exceptional electrical and thermal conductivity, impressive mechanical strength, and remarkable single-atom thickness. These distinctive properties position it as a highly promising material for a diverse array of applications, ranging from flexible electronics and high-performance batteries to ultra-fast transistors and potential advancements in medical devices. The widespread recognition of graphene's potential to revolutionize multiple industries has spurred extensive research and exploration into its capabilities (18). Graphene's high surface-to-volume ratio makes it a particularly attractive material for sensing applications. When it is used as an electrode, all carbon atoms contact the analyte, which results in very high sensitivity. Moreover, no impurities are transferred to the analytes from graphene, electrochemistry of the sensing application thus remains intact. Lastly, graphene is biocompatible (17). All of these characteristics combined with the inherent properties of memristance are promising for developing sensitive, selective, area efficient sensors.

Both graphene and its derivatives, including functionalized graphene, have undergone comprehensive study for their viability as electrode and interface materials in memristive devices. These materials offer significant advantages, such as suitability for device fabrication, exceptional mechanical flexibility, and high optical transparency, all of which can greatly contribute to the advancement and enhancement of memristive technologies. Investigation of prior research reveals a wide spectrum of approaches for patterning graphene, encompassing direct mechanical cleavage, electron beam irradiation, scanning probe lithography, helium ion beam lithography, photocatalytic etching, plasma

etching, chemical etching, nanoimprint lithography, and bottom-up growth and synthesis (19). Nevertheless, these methods exhibit certain limitations, such as constraints in scalability, intricate process requirements, high production costs, and potential damage to the graphene's properties and structure during patterning. While each method presents its own set of challenges, the need for a technique that can efficiently pattern graphene without compromising its exceptional characteristics remains a critical goal in advancing its practical applications.

This study aims to explore a convenient, repeatable, and straightforward method for patterning graphene for memristor applications while utilizing the memristor's inherent properties. Larger memristive devices of area 2 cm^2 (hereforth referred to as macro devices) were fabricated to develop fabrication steps and ensure that graphene can be used as a top electrode. The macro devices are fabricated very simply since they do not require any patterning steps. Following successful characterization and sensor measurements, memristors of micrometric dimensions (hereforth referred to as micro devices) were fabricated and electrically characterized. The ultimate objective is to use graphene as a sensitive top electrode for memristive sensors. By acknowledging the constraints of various methodologies, this research focuses on patterning CVD grown and transferred graphene via negative photolithography and lift-off. Furthermore, this paper presents measurement outcomes, encompassing results from current-voltage characterization and the sensing of memristors comprising $\text{Pt}/\text{TiO}_2/\text{TiO}_x/\text{Graphene}$ structures.

MATERIAL AND METHODS

Chemical Vapor Deposition (CVD) for Graphene Growth

Initially, copper foils (Alfa Aesar, 13382, 99.8% purity, 25 μm ; cut to dimensions of 50 mm \times 50 mm) are placed onto a flat quartz boat and positioned within a quartz tube to align with the heating zone. Argon gas (Ar) is flowed through the tube at a rate of 100 sccm for 10 minutes. After purging with Ar, the Ar flow is decreased to 50 sccm and hydrogen gas (H_2) at a flow rate of 50 sccm is introduced into the tube, and heating is commenced. Once the temperature reaches 1000°C , the copper foil is annealed under hydrogen and Ar gas for a duration of 1 hour. Following this 1-hour interval, methane gas (CH_4) at a flow rate of 5 sccm is introduced alongside Ar gas (50 sccm) and hydrogen gas (50 sccm) to facilitate graphene growth over a period of 30 minutes. Post-growth, rapid cooling of the sample is conducted within Ar and hydrogen atmosphere.

Graphene Transfer

A solution of 1 M FeNO_3 (200 ml) is poured into a glass petri dish, and the samples are positioned on the liquid's surface. Approximately 30 minutes later, the copper foil is fully etched by the FeNO_3 solution. The removal of FeNO_3 is executed with care, after which deionized water is introduced into the petri dish, taking precautions to avoid disruption of the graphene layer floating on the liquid. This rinsing process is reiterated until complete removal of FeNO_3 is ensured. In the concluding step, the graphene layer, which remains on the water's surface, is transferred onto the designated substrate. The substrate is immersed in the water, allowing the graphene to settle onto it. Finally, the sample is carefully lifted from the water.

Macro Device Fabrication

Macro devices were fabricated prior to the fabrication of micro devices to develop repeatable and reliable recipes. The first step of the fabrication process is e-beam evaporation. The chamber is pumped down to 6×10^{-3} mTorr before deposition. Chromium was used as an adhesion layer. During Cr deposition, the electric current was gradually raised to 8 mA to achieve a consistent deposition rate of 0.2 \AA/s . Once it was confirmed that this was a stable condition, current was increased 0.5 mA per minute until reaching 12 mA to achieve a deposition rate of 0.5 \AA/s . While developing the recipe, Cr of 50 nm thickness was deposited. Subsequent coatings, including the ones for the microstructures, were executed based on this process.

During Pt deposition, rapid increments in the applied current to the Pt crucible led to the occurrence of sparking, this caused both inefficient use of resources, unstable deposition rates and poor uniformity. As such, the deposition was carried out very slowly. However, the longer process still meant that the chamber heated up significantly since Pt requires high applied current due to its higher melting point. 90mA current was reached in 3 hours by initially increasing the current in steps of 0.5 mA every 30 seconds. After the Pt had melted, the current step was increased to 1 mA every 30 seconds. A 0.1 \AA/s deposition rate was achieved while applying a current of 91mA. For the initial sample used to develop the recipe, a Pt layer of 23 nm was coated. All the following Pt depositions were based on this process. With all the measures to prevent sparking, unstable deposition rates, taking breaks during the deposition to allow the chamber to cool, this recipe ended up being very challenging to carry out. Therefore, it was decided to deposit Pt as a thin capping layer for Cr with a thickness of 7 nm.

TiO_2 was sputtered in RF mode using a TiO_2 target 20 nm thick in 20 minutes with conditions involving 20 sccm Ar, ~ 7 mTorr chamber pressure, 100 W power, 16% CT,

56% CL using Vaksis PVD Handy Twin Sputtering System-3 at Bilkent UNAM. Prior to starting the reaction, chamber pressure is pumped down to below $5\text{E-}6$ Torr. TiO_x layer was sputtered with the Leybold L560 Box Coater in the Advanced Research Laboratory. TiO_x layer was sputtered using a Titanium target with Argon, while giving a minimal amount of oxygen ($<5\%$) to prevent the cessation of the reaction. 20 nm thick TiO_x was coated with 200 sccm of Argon, 4 sccm of O_2 , 150 W power conditions at 3 \AA/s deposition rate. The macro device fabrication is then completed through the transfer of a graphene layer onto the substrate. Fig. 1 shows layers and fabrication process of the macro Pt/ TiO_2 / TiO_x /Graphene device.

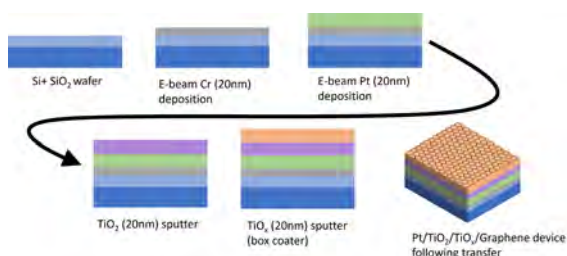


Figure 1. Layers and fabrication process of the macro Pt/ TiO_2 / TiO_x /Graphene device involving sequentially e-beam deposition, sputtering and graphene transfer

Micro Device Fabrication

The fabrication of memristor devices with graphene top electrodes arranged in a crossbar pattern is made possible by a set of 3 masks: Mask 1 for the bottom electrode, Mask 2 for the active layer and graphene, and Mask 3 for the top contact pads. There are 52 1 cm^2 chips on wafer with 3 different structure types and varying dimensions. Table 1 shows the pad dimensions for the memristive device with graphene top electrode.

Table 1. Pad dimensions for the micro memristive structures with graphene top electrodes

	Pad dimensions	Active layer dimensions
Large single device	$100 \mu\text{m} \times 100 \mu\text{m}$	$100 \mu\text{m} \times 226.09 \mu\text{m}$
Small single device	$21.74 \mu\text{m} \times 21.74 \mu\text{m}$	$21.74 \mu\text{m} \times 52.17 \mu\text{m}$
Large 8x8 crossbar	$47.83 \mu\text{m} \times 47.83 \mu\text{m}$	$12.3 \mu\text{m} \times 534.78 \mu\text{m}$
Small 8x8 crossbar	$21.74 \mu\text{m} \times 21.74 \mu\text{m}$	$21.74 \mu\text{m} \times 60.87 \mu\text{m}$
12x12 crossbar	$21.74 \mu\text{m} \times 21.74 \mu\text{m}$	$8.7 \mu\text{m} \times 408.7 \mu\text{m}$

Fig. 2 illustrates the structure of the single device, which consists of a top layer made of Cr and Pt electrode pads, an active layer made up of a stoichiometric TiO_2 / TiO_x topped with graphene, and a bottom layer made of Cr and Pt electrode pads. The horizontal lines in the mask set are created using the bottom electrode mask, while the vertical lines are created using the top electrode mask.

Prior to fabricating the device featuring a graphene top electrode, a more traditional memristor with a platinum top electrode had already been fabricated and characterized (20). As such, the fabrication process had been tested and

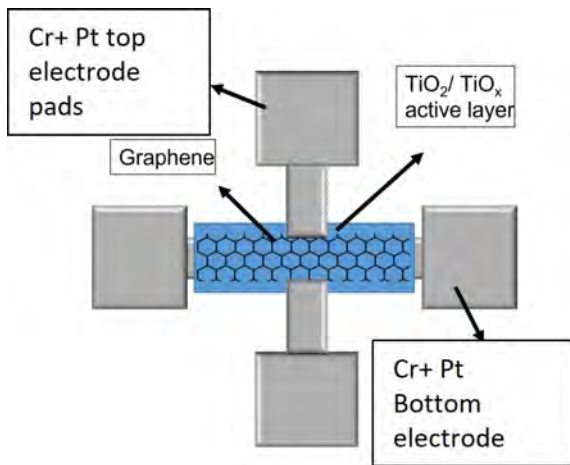


Figure 2. Top view of micro memristor structure with graphene top electrode consisting of Cr+Pt top electrode pads, $\text{TiO}_2/\text{TiO}_x$ active layer, Cr+Pt bottom electrode

verified except for the graphene transfer, patterning and characterization.

Fig. 3 illustrates the fabrication process of memristor with graphene top electrode. A Si wafer with SiO_2 (300nm) passivation layer was used. Then, photolithography technique was initially used to create the bottom electrode, as shown in Fig. 3(a), using a mask aligner. AZ5214E was chosen as the photoresist for the photolithography stage due to its ability to facilitate image reversal (21). In the mask aligner, the contact mode was selected as vacuum+hard and the separation, which means the distance between the mask and the substrate during alignment, was determined as 50 μm . The mask thickness was chosen as 2.3mm, the 4-inch wafer thickness as 0.5mm, and the photoresist thickness as 1.4 μm . The UV exposure dose was determined as 50 mJ/cm². Prior to the flood exposure step, it is essential to undergo an annealing process, also known as hard bake, for 2 minutes on each layer. Afterward, by adjusting the UV exposure dose to 230 and performing the flood exposure step without photomask, the lithography process was completed just as it was for each layer. The top of the wafer, which was obtained after the development stage using AZ400K as a developer, was coated with 20 nm layer of Cr and 7 nm layer of Pt, as depicted in Fig. 3(b), using e-beam process that was developed and described for the macro devices. Following the application of the optimized lift-off technique using acetone, as shown in Fig. 3(c), the photolithography stage for the active layer commenced, as illustrated in Fig. 3(d). Upon the completion of the development phase, the top of the wafer was coated with 20 nm layer of TiO_2 and then 20 nm layer of TiO_x using sputtering, as illustrated in the Fig. 3(e).

The sputtering was carried out using the same recipe that was described for macro devices. This combination of materials allows for resistive switching to occur through the movement of oxygen vacancies within the active layer.

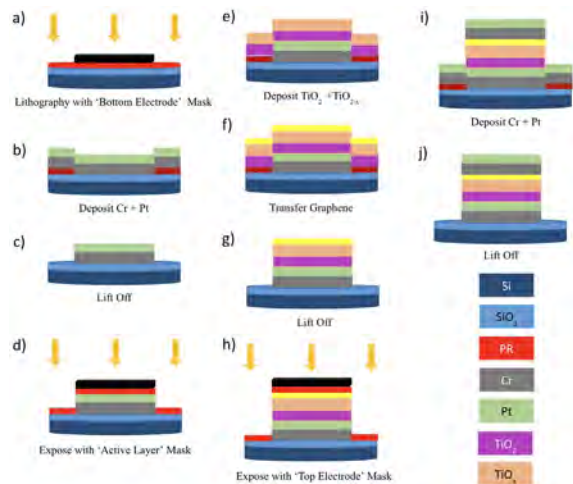


Figure 3. Fabrication process flow of micro Pt/ $\text{TiO}_2/\text{TiO}_x$ /Graphene device with graphene top electrode including (a)lithography with bottom electrode mask, (b)depositing Cr+Pt, (c)lift off, (d)exposing with active layer mask, (e)depositing $\text{TiO}_2/\text{TiO}_x$ (f) transferring graphene, (g)lift off, (h)exposing with top electrode mask, (i) depositing Cr+Pt, (j)lift off.

Graphene was transferred directly after the sputtering of TiO_x , as depicted in Fig. 3(f). Upon transferring the graphene onto the wafer, the lift-off technique was applied, as shown in the Fig. 3(g), and the patterned graphene was examined using a microscope. Fig. 4 shows the orange line border indicating the graphene area on a 4-inch wafer. After completing the photolithography and development stages for the top electrode, as depicted in Fig. 3(h), which will form the final layer of the device, the top of the wafer was coated with 7 nm layer of Pt on 20 nm layer of Cr using the e-beam evaporator, as shown in Fig. 3(i). By utilizing the optimized lift-off stage with acetone, as depicted in the Fig. 3(j), the desired device was obtained. Fig. 5 shows microscope

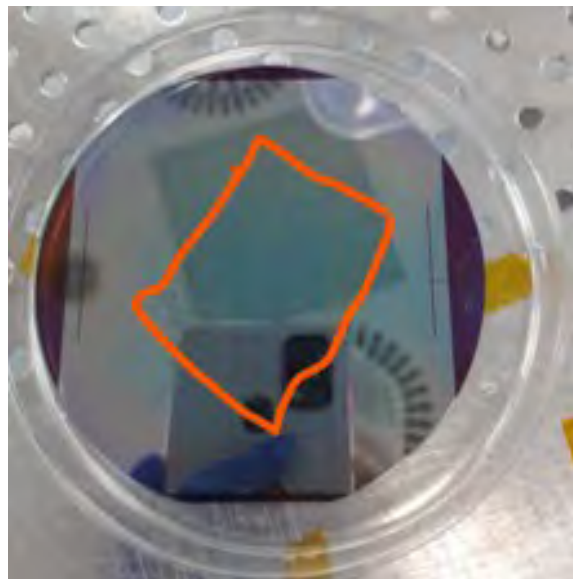


Figure 4. Photograph of micro patterned 4-inch full wafer just after graphene transfer on top of photoresist $\text{TiO}_2/\text{TiO}_x$ before lift-off is completed to pattern active layer and graphene. The area with graphene is bordered by orange line for clarity.

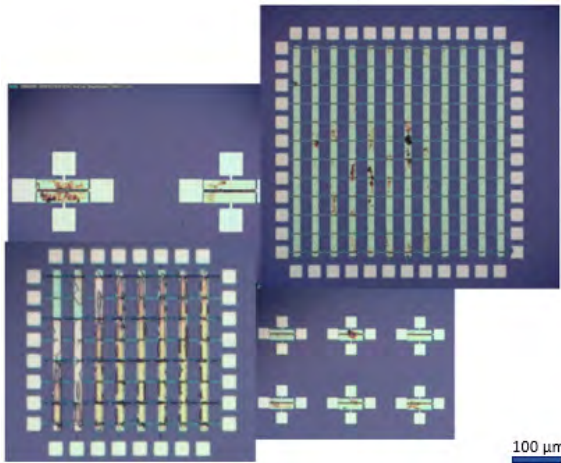


Figure 5. Optical microscope photographs of the fabricated micro memristive structures with graphene top electrodes

photographs of the graphene top electrode microstructures in which the electrode pads were coated and patterned after transferring the graphene.

RESULTS AND DISCUSSION

Pt/TiO₂/TiO_x/Graphene Macro Devices

Upon completing the fabrication of conventional memristors with platinum top electrodes, we initiated the production of graphene top electrodes using macro samples for convenience. Therefore, we obtained novel devices. The fishing method was employed for transferring the graphene. This method can be used to transfer large, macroscopic samples of graphene, which can be convenient for certain applications.

A Sigma Aldrich micro pipette was utilized to control the amount of liquid that was dripped into the macro memristor. The ratio of glucose syrup to water was 1:10 in both experiments.

The graphene macro device, which has the sample dripped and connected to the NI PXIe4139, appears as illustrated in Fig. 6. By connecting the device to the NI PXIe4139, it is possible to perform detailed electrical measurements and gain insight into the device's behavior and performance.

The measurements were conducted by exciting the devices with an input current signal and measuring the resulting voltage across it. Hence, strictly speaking Fig.7 shows a V-I curve where input signal is current, this figure clearly depicts the memristive behavior exhibited by the graphene top electrode macro device where the R_{OFF}/R_{ON} ratio is 80.

Fig. 8(a) presents the memristance measurement results for three different conditions: without a sample (represented by blue), with a water drop (represented by black),

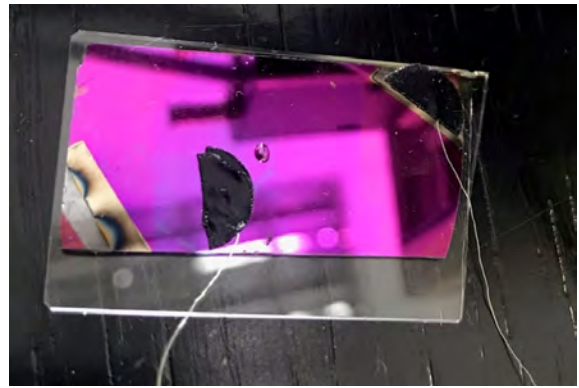


Figure 6. Fabricated macro Pt/TiO₂/TiO_x/Graphene device's measurement setup with sample

and with a 1 μl glucose syrup water drop (represented by green). As shown in the figure, the addition of a 1μl glucose syrup water drop led to lower memristance values.

In the absence of liquid on the graphene surface, the memristor exhibits high ROFF values (450 kΩ in the first cycle, 320 kΩ-350 kΩ in the second cycle). The addition of a 4 μl water drop resulted in a ROFF value that was similar to the value obtained in the absence of a sample, but lower (400 kΩ in the first cycle, 250 kΩ-280 kΩ in the second cycle). The addition of a 1 μl drop of a glucose syrup water mixture resulted in a significant decrease in the ROFF value, which became stable at 173 kΩ. The RON values were measured as follows: 104 kΩ with the addition of glucose syrup, 122 kΩ with water, and 125-129 kΩ in the control condition with no sample present. These results provide sufficient evidence to establish a trend.

Fig. 8(b) shows the results of observations of water drops with varying amounts of glucose syrup. The figure illustrates the memristance measurement results for three distinct conditions: the absence of a sample, represented by blue; the presence of a 1 μl glucose syrup water drop, represented by green; and the presence of a 4 μl glucose syrup water drop, represented by red. The results obtained from mixing 4 μl of glucose syrup with water were similar to those obtained when using only water. When the droplet with 4 μl glucose syrup was deposited, ROFF was 315 kΩ and 280

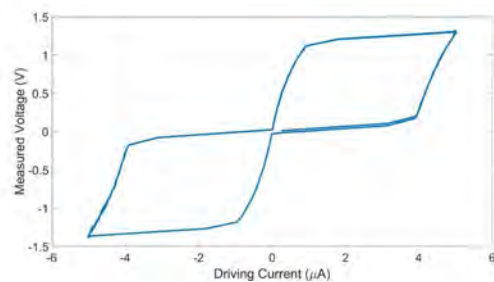


Figure 7. Driving current vs. measured voltage curve of graphene top electrode macro memristive device driven by a square wave current of 83 Hz 5μA amplitude with pinched hysteresis

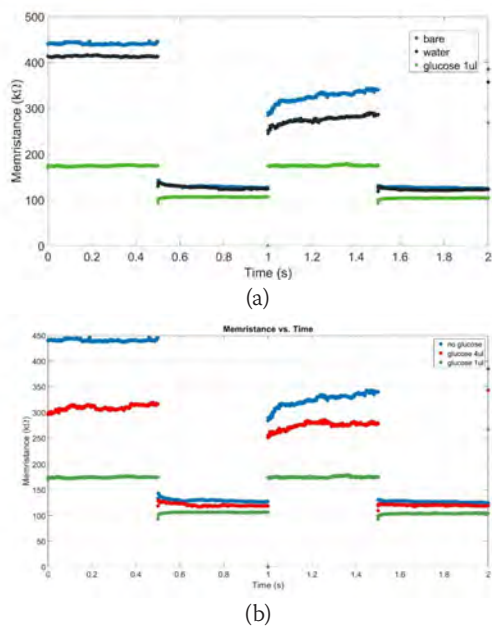


Figure 8. (a) Memristance measurement results of macro Pt/TiO₂/TiO_x/Graphene device without sample, with water drop, with 1 μl glucose syrup water drop (b) Memristance measurement results of macro t/TiO₂/TiO_x/Graphene device without sample, with 1 μl glucose syrup water drop, with 4 μl glucose syrup water drop

kΩ and RON was 120 kΩ. Depositing a liquid sample on top of the graphene electrode clearly changes the conductivity mechanism of the electrode and possibly influences the active layer underneath.

Pt/TiO₂/TiO_x/Graphene Micro Devices: Graphene Characterization

Fig. 9 shows patterned graphene with optimized lift-off. Achieving a successful result with graphene after lift-off typically depends on the ability to maintain the continuity of the graphene layer during the transfer process (22). In order to maintain the continuity of graphene, it is important to use a high-resolution photolithography system, choose carefully the photoresist material and determine the lift-off time (23). If the lift-off time is not carefully controlled, it can lead to damage to the graphene layer. This may involve conducting experiments to determine the optimal lift-off time for a particular application or using advanced techniques such as atomic force microscopy to monitor the lift-off process in real-time.

In the context of lift-off processes, Raman spectroscopy plays a pivotal role in confirming the existence and quality of graphene (24). The top of the active layer is covered with graphene, Fig. 10 (a) shows the device and area that was analyzed, and Fig. 10(b) showcases discernible G and 2D peaks, signature of graphene. Raman analysis substantiates the existence of few-layer graphene with structural integrity and continuity.



Figure 9. Top view optical microscope photograph of micro memristive device after graphene patterning with optimized lift-off

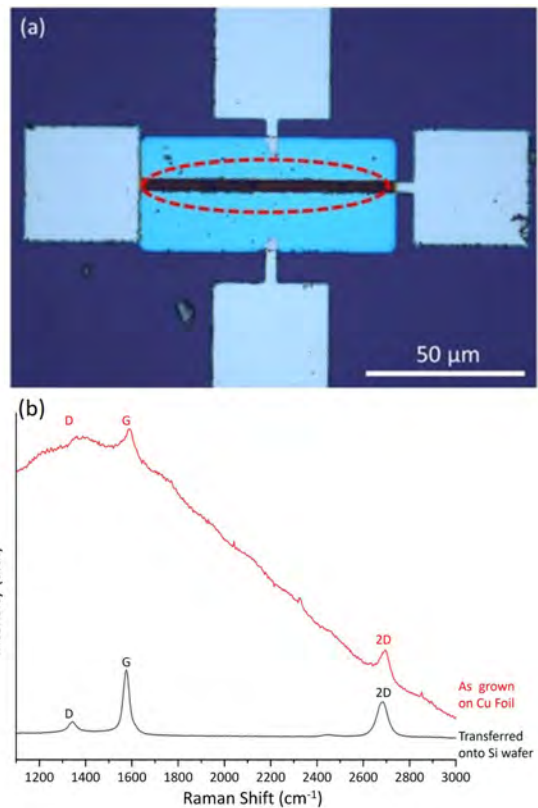


Figure 10. Verification of few-layer graphene (a) Top view optical microscope photograph of the micro Pt/TiO₂/TiO_x/Graphene device the red dashed circle marks the area where Raman Spectroscopy is performed (b) Raman spectrum of graphene prior to transfer to the wafer (shown in red) and after having been transferred and patterned (shown in black) on the micro Pt/TiO₂/TiO_x/Graphene device

Pt/TiO₂/TiO_x/Graphene Micro Devices: I-V Characterization

I-V measurements can be used to assess the device's performance and determine input dependent variations in its resistance. Electrical characterization results in Fig. 11 show that the graphene top electrode micro memristive

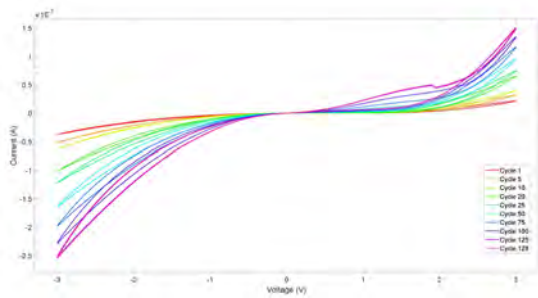
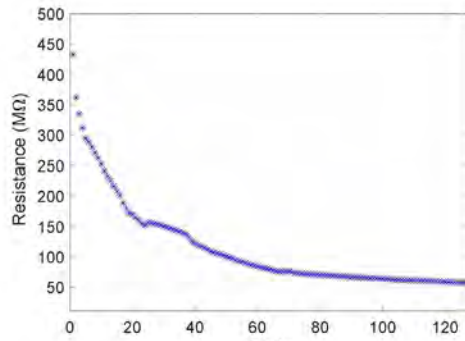
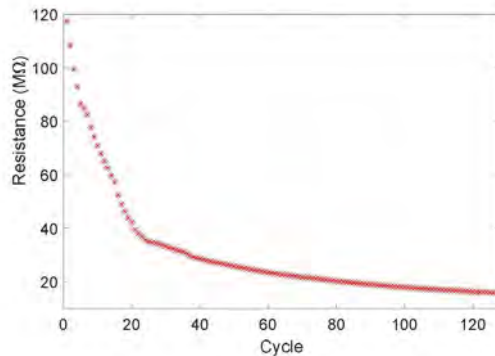


Figure 11. I-V Measurements of micro Pt/TiO₂/TiO_x/Graphene device



(a)



(b)

Figure 12. Resistance values of the device were measured at $V_{read}=2.1V$ to show the cycle-to-cycle variation in each quadrant (a) Resistance of micro Pt/TiO₂/TiO_x/Graphene device for positive quadrant during 128 cycles (b) Resistance of micro Pt/TiO₂/TiO_x/Graphene device for negative quadrant during 128 cycles

device clearly exhibits diodic behavior in both the positive and negative quadrants. Unlike the macro devices, distinct resistance states are not demonstrated by this device. However, the resistance is input dependent. Moreover, there is a cycle-to-cycle variation in resistance. This can be deduced when one compares the I-V plot from earlier cycles to later cycles: the red plot (Cycle 1) shows a high resistance and magenta plot (Cycle 128) shows a much lower resistance. This is better demonstrated in Fig. 12 which depicts the drop in device resistance from one cycle to the next. This drop in resistance is more rapid at first in both quadrants e.g. as shown in Fig. 12 (a) a

drop from 450 MΩ to 150 MΩ is observed in the HRS value in the positive quadrant during the first 20 cycles, after which the resistance settles more gradually to around 50 MΩ during the next 108 cycles. This trend applies to both quadrants. These micro devices exhibit much higher resistances and are susceptible to charging. This would explain the cycle-to-cycle variation. The device resistance in both quadrants exhibit some hysteresis and consecutive cycles show that resistance decreases gradually due to excitation.

CONCLUSION

A fabrication method to utilize graphene as a top electrode in memristive devices is presented. Electrical and structural characterization results demonstrate that: (i) graphene is a promising material to utilize memristive devices as sensors and (ii) the developed fabrication method and lift-off method yields continuous, patterned graphene top electrodes. Both sets of devices, macro and micro, were fabricated using the same deposition and transfer methods. The microstructures were patterned using photolithography and lift-off. Electrical characterization was carried out in all cases by applying the input signal to the top electrode and grounding the device from the Pt bottom electrode. The first and most fundamental aim of electrical characterization was to demonstrate that the graphene in fact functions as an electrode i.e. an applied current results in a potential difference across the grounded bottom electrode and the graphene electrode, or if the input is a voltage signal, that this input results in a current that flows from the bottom electrode to the graphene electrode. Secondly, as the aim was to utilize memristive dynamics, it was important to verify that these devices exhibited memristance. Both were demonstrated through I-V measurements as shown in Fig. 7 and Fig. 12. Both macro and micro devices exhibit input dependent memristance. In the case of the macro device distinct resistance states were observed which enabled sensor measurements to show that these Pt/TiO₂/TiO_x/Graphene devices could discern between a state of having no deposited sample, a water drop, and a glucose drop.

These experiments yielded convincing results. Lastly, since the fabrication method is novel to our knowledge graphene had to be tested with surface measurement techniques such as Raman to corroborate that it remained continuous after the lift-off process. These measurements also produced positive results.

This work has attained encouraging results. Memristive devices with graphene top electrodes have the potential to have a significant impact in the future, given the many advantages of graphene as a material. They may be used in a variety of applications, including in memory and computing

devices, as well as in sensors and energy storage systems. Graphene is a promising material for use in memristive devices, due to their excellent electrical and mechanical properties, as well as their high strength and flexibility.

ACKNOWLEDGEMENT

This work was supported by TUBITAK [grant number: 119E367].

CONFLICT OF INTEREST

Authors approve that to the best of their knowledge, there is not any conflict of interest or common interest with an institution/organization or a person that may affect the review process of the paper.

AUTHOR CONTRIBUTION

Selin Onay: Fabrication, Writing- original draft

Omer R. Caylan: Graphene synthesis, transfer, Raman measurements



Goknur Buke: Graphene characterization analysis, writing- review and editing

Itr Koymen: Conceptualization, Electrical characterization, Methodology, Analysis, Supervision, Writing- review and editing

REFERENCES

- Chua L. Memristor-The missing circuit element. *IEEE Trans Circuit Theory*. 1971;18(5):507-19.
- Strukov DB, Snider GS, Stewart DR, Williams RS. The missing memristor found. *Nature*. 2008 May 1;453(7191):80-3.
- Hamdioui S, Taouil M, Du Nguyen HA, Haron A, Xie L, Bertels K. Memristor: the enabler of computation-in-memory architecture for big-data. In: 2015 International Conference on Memristive Systems (MEMRISYS) [Internet]. Paphos, Cyprus: IEEE; 2015 [cited 2023 Aug 14]. p. 1-3. Available from: <http://ieeexplore.ieee.org/document/7378391/>
- Rady H, Hossam H, Saied MS, Mostafa H. Memristor-Based AES Key Generation for Low Power IoT Hardware Security Modules. In: 2019 IEEE 62nd International Midwest Symposium on Circuits and Systems (MWSCAS) [Internet]. Dallas, TX, USA: IEEE; 2019 [cited 2023 Aug 14]. p. 231-4. Available from: <https://ieeexplore.ieee.org/document/8885031/>
- Zhao C, Shen ZJ, Zhou GY, Zhao CZ, Yang L, Man KL, et al. Neuromorphic Properties of Memristor towards Artificial Intelligence. In: 2018 International SoC Design Conference (ISOC) [Internet]. Daegu, Korea (South): IEEE; 2018 [cited 2023 Aug 14]. p. 172-3. Available from: <https://ieeexplore.ieee.org/document/8649926/>
- Zhou Z, Yang F, Wang S, Wang L, Wang X, Wang C, et al. Emerging of two-dimensional materials in novel memristor. *Front Phys*. 2022 Apr;17(2):23204.
- Rozenberg MJ, Inoue IH, Sánchez MJ. Nonvolatile Memory with Multilevel Switching: A Basic Model. *Phys Rev Lett*. 2004 Apr 30;92(17):178302.
- Gebregiorgis A, Singh A, Diware S, Bishnoi R, Hamdioui S. Dealing with Non-Idealities in Memristor Based Computation-In-Memory Designs. In: 2022 IFIP/IEEE 30th International Conference on Very Large Scale Integration (VLSI- SoC) [Internet]. Patras, Greece: IEEE; 2022 [cited 2023 Aug 14]. p. 1-6. Available from: <https://ieeexplore.ieee.org/document/9939618/>
- Kim GS, Song H, Lee YK, Kim JH, Kim W, Park TH, et al. Defect-Engineered Electroforming-Free Analog HfO_x Memristor and Its Application to the Neural Network. *ACS Appl Mater Interfaces*. 2019 Dec 18;11(50):47063-72.
- Hu SG, Liu Y, Chen TP, Liu Z, Yu Q, Deng LJ, et al. Emulating the paired-pulse facilitation of a biological synapse with a NiO_x-based memristor. *Appl Phys Lett*. 2013 May 6;102(18):183510.
- Sun W, Gao B, Chi M, Xia Q, Yang JJ, Qian H, et al. Understanding memristive switching via in situ characterization and device modeling. *Nat Commun*. 2019 Aug 1;10(1):3453.
- Abbas H, Abbas Y, Truong SN, Min KS, Park MR, Cho J, et al. A memristor crossbar array of titanium oxide for non-volatile memory and neuromorphic applications. *Semicond Sci Technol*. 2017 Jun 1;32(6):065014.
- Paul S, Harris PG, Pal C, Sharma AK, Ray AK. Low cost zinc oxide for memristors with high On-Off ratios. *Mater Lett*. 2014 Sep;130:40-2.
- Awais MN, Muhammad NM, Navaneethan D, Kim HC, Jo J, Choi KH. Fabrication of ZrO₂ layer through electrohydrodynamic atomization for the printed resistive switch (memristor). *Microelectron Eng*. 2013 Mar;103:167-72.
- Ali S, Khan S, Khan A, Bermak A. Memristor Fabrication Through Printing Technologies: A Review. *IEEE Access*. 2021;9:95970-85.
- Kumar S, Wang Z, Huang X, Kumari N, Davila N, Strachan JP, et al. Conduction Channel Formation and Dissolution Due to Oxygen Thermophoresis/Diffusion in Hafnium Oxide Memristors. *ACS Nano*. 2016 Dec 27;10(12):11205-10.
- Justino CIL, Gomes AR, Freitas AC, Duarte AC, Rocha-Santos TAP. Graphene based sensors and biosensors. *TrAC Trends Anal Chem*. 2017 Jun 1;91:53-66.
- Colak M, Onay S, Orhan B, Milano G, Koymen I. Simulation of Half-Center Oscillator Circuits Employing Newly Developed Models of Fabricated Memristors. In: 2022 International Symposium on Multidisciplinary Studies and Innovative Technologies (ISMSIT) [Internet]. Ankara, Turkey: IEEE; 2022 [cited 2023 Aug 18]. p. 504-8. Available from: <https://ieeexplore.ieee.org/document/9932824/>
- Long ML, Newman J. Image Reversal Techniques With Standard Positive Photoresist. In: Willson CG, editor. Santa Clara; 1984 [cited 2023 Aug 18]. p. 189. Available from: <http://proceedings.spiedigitallibrary.org/proceeding.aspx?doi=10.1117/12.941793>
- Rasool HI, Song EB, Allen MJ, Wassei JK, Kaner RB, Wang KL, et al. Continuity of Graphene on Polycrystalline Copper. *Nano Lett*. 2011 Jan 2;11(1):251-6.
- Zheng Y, Wang H, Hou S, Xia D. Lithographically Defined Graphene Patterns. *Adv Mater Technol*. 2017 May;2(5):1600237.

COVID-19 Diagnosis from Blood Gas Using Multivariate Linear Regression

Faruk Ayata¹  Ebubekir Seyyarer² 

¹Van Yuzuncu Yil University, Computer Technologies, Van, Türkiye

²Van Yuzuncu Yil University, Computer Engineering, Van, Türkiye

ABSTRACT

With the impact of the COVID-19 outbreak, almost all scientists and nations began to show great interest in the subject for a long time. Studies in the field of outbreak, diagnosis and prevention are still ongoing. Issues such as methods developed to understand the spread mechanisms of the disease, prevention measures, vaccine and drug research are among the top priorities of the world agenda. The accuracy of the tests applied in the outbreak management has become extremely critical. In this study, it is aimed to obtain a function that finds the positive or negative COVID-19 test from the blood gas values of individuals by using Machine Learning methods to contribute to the outbreak management. Using the Multivariate Linear Regression (MLR) model, a linear function is obtained to represent the COVID-19 dataset taken from the Van province of Turkey. The data set obtained from Van Yüzüncü Yıl University Dursun Odabaş Medical Center consists of blood gas analysis samples (109 positive, 1146 negative) taken from individuals. It is thought that the linear function to be obtained by using these data will be an important method in determining the test results of individuals. Gradient Descent optimization methods are used to find the optimum values of the coefficients in the function to be obtained. In the study, the RMSProp optimization algorithm has a success rate of 58-91.23% in all measurement methods, and it is seen that it is much more successful than other optimization algorithms.

Keywords:

Multivariate linear regression; COVID-19; Blood gases.

INTRODUCTION

The COVID-19 pandemic is an infectious disease that emerged in the city of Wuhan, China, in 2019 and quickly spread worldwide. Diagnosis of COVID-19 is typically performed using various methods such as symptoms, imaging techniques, and laboratory tests [1, 2]. Common symptoms include fever, cough, shortness of breath, muscle aches, fatigue, headache, and loss of taste or smell [3]. Imaging techniques are another auxiliary method in the diagnosis of COVID-19. The most commonly used methods include computerized tomography (CT) and chest X-rays. These imaging methods can help detect damage, inflammation, and other abnormalities in the lungs [4, 5]. The most common laboratory tests include polymerase chain reaction (PCR) tests, antigen tests, and antibody tests. The PCR test helps diagnose COVID-19 by detecting the genetic material of the virus in the patient's respiratory samples. In addition to these, blood gas values are important parameters

that needs to be monitored during the disease management process [6]. Hemoglobin, composed of heme and globin, which transport gases in the blood, is present in all living organisms. Hemoglobin's primary function is to transport oxygen (O_2) from the lungs to peripheral tissues and carry carbon dioxide (CO_2) from tissues to the lungs. An increase in carboxyhemoglobin levels has been observed in COVID-19 patients receiving treatment in intensive care units [6]. Diagnosing whether or not someone is infected with COVID-19 remains a current challenge. Machine learning methods, which have provided solutions to many contemporary problems, can also play a significant role in the fight against COVID-19.

Machine learning techniques can be applied in various fields such as tracking the spread of the virus, making diagnoses, optimizing treatment, and discovering potential vaccines. COVID-19 diagnosis is categorized

Article History:

Received: 2023/09/20

Accepted: 2024/02/73

Online: 2024/03/31

Correspondence to: Faruk Ayata,
Van Yüzüncü Yıl University, Computer
Technologies, Van, TÜRKİYE
E-Mail: farukayata@yyu.edu.tr;
Phone: +90 531 500 33 66.

This article has been checked for similarity.



This is an open access article
under the CC-BY-NC licence

<http://creativecommons.org/licenses/by-nc/4.0/>

Cite as:

Ayata F, Seyyarer E. COVID-19 Diagnosis From Blood Gas Using Multivariate Linear Regression. Hittite Journal of Science and Engineering 2024;11 (1):15-23. doi:10.17350/hjse19030000327

as a Non-deterministic Polynomial problem, and analytical methods of Machine Learning that provide exact results are not preferred for solving such problems [7]. This is because as the dimensions of the problem increase, analytical methods become cost-prohibitive. Instead of analytical methods, heuristic or metaheuristic approach algorithms inspired by nature are recommended, which provide approximate results and are optimization-based, such as Artificial Neural Networks [7, 8], Genetic Algorithms [7, 9], Particle Swarm Optimization [7, 10], and others. The reason for this is that these methods can provide approximate results at a reasonable cost even as the size of the problem increases. Such methods do not guarantee exact results [11, 12].

Intuitive methods are techniques aimed at finding a satisfactory solution through trial and error without guaranteeing that the solution is optimal or even close to optimal. These methods are typically used for complex problems that cannot be solved with analytical methods or in situations where an approximate solution is acceptable [7]. Metaheuristic methods, on the other hand, are optimization techniques that combine multiple intuitive methods to obtain a better solution [13]. These methods aim to explore the search space more efficiently than simple heuristic methods by using various strategies such as randomization, neighborhood search, and adaptive memory. Metaheuristic methods are often used in complex optimization problems where the search space is vast and navigation is challenging [8, 13].

Multivariate linear regression is based on the assumption that the dependent variable can be expressed as a linear combination of independent variables. Therefore, it is one of the most suitable metaheuristic methods to use when data exhibits a linear relationship [14, 15]. Multivariate linear regression can be employed in crises such as the COVID-19 pandemic for tasks such as predicting the course of the outbreak, determining the disease burden, assessing healthcare resource requirements, planning pandemic control strategies, and evaluating their effectiveness.

Özen et al. (2021) use machine learning methods to make predictions for the detection of COVID-19 cases. They employed Python and R programming languages and utilized Prophet, Polynomial Regression, ARIMA, Linear Regression, and Random Forest models for their predictions. They reported that the Polynomial regression method provided the best prediction results [15]. Saadatmand et al. (2021) developed a model for the detection of oxygen therapy needs of COVID-19 patients. This model includes five different methods: Logistic Regression, Random Forest, XGBoost, C5.0, and Artificial Neural Networks. They used data obtained from two local hospitals in Iran to create their dataset. Test results showed that the Logistic Regression

and Artificial Neural Networks used in the model achieved the highest accuracy rate [16]. Mohan et al. (2021) used their Ensemble Learning, Autoregressive, and Moving Regressive (EAMA) hybrid model to detect COVID-19. The EAMA model, also known as a community learning, autoregressive model, and moving average model, used data from the Ministry of Health and Family Welfare in India and Worldometers. Their analysis allowed for detailed predictions of active cases and deaths at the state level in India [17]. Pinter et al. (2020) proposed a hybridization model consisting of a network-based fuzzy inference system and a multi-layer perceptron-empirical competitive algorithm for the prediction of COVID-19. The performance evaluation of the proposed model used metrics such as Mean Absolute Percentage Error, Root Mean Square Error (RMSE), and coefficient of determination (R-squared). The analysis indicated promising results for the proposed method in disease prediction [18]. Elaziz et al. (2020) used CXR images to distinguish COVID-19 cases. They proposed a new feature selection method and utilized a modified mantis-ray search optimization algorithm based on Modified Reflective and Fitness-Oriented Differential Evolution (MRFODE) to determine relevant subset features. Test results indicated promising accuracy values in classifying COVID-19 patient samples [19].

In this study, a method is aimed to be developed for the detection of the COVID-19 virus from blood gas data frequently used in laboratory tests and for monitoring the disease following transmission. The method includes a multivariate linear regression model, six gradient descent-based optimization algorithms to minimize error, and a dataset obtained from the Van province of Turkey for COVID-19.

MATERIAL AND METHODS

Optimization Algorithms

The primary objective of optimization algorithms is to minimize the error quantity. Methods based on Gradient Descent, such as Stochastic Gradient Descent (SGD), Momentum Stochastic Gradient Descent (MMT), Adadelta Gradient Descent (AGD), RMSProp (RMP), Adagrad (ADD), and Adam (ADM), are among the most commonly used optimization algorithms. These algorithms are employed to reduce the error quantity and improve the model's performance. Table 1 displays these algorithms [20- 24].

Objective Functions

The choice of the objective function is dependent on the goal of the optimization algorithm. This goal is typically determined as enhancing the model's accuracy or minimizing the error quantity. Integral of Absolute Er-

Table 1. Most popular gradient descent methods [20- 24].

Algorithm Name	Formula	Description
SGD	$W_{t+1} = W_t - a \frac{\partial L}{\partial W_t}$	The current derivative ($\partial L/\partial w_t$) updates the current weight (w_t) by multiplying it with the learning rate (a).
MMT	$w_{t+1} = w_t - aV_t$ $V_t = \beta V_{t-1} + (1-\beta) \frac{\partial L}{\partial W_t}$	The initial value of V_t is 0. β is between 0 and 1, and it is commonly taken as 0.9.
ADG	$w_{t+1} = w_t - \frac{a}{\sqrt{S_t + \epsilon}} \cdot \frac{\partial L}{\partial w_t}$ $S_t = S_{t-1} + \left[\frac{\partial L}{\partial w_t} \right]^2$	S starts as 0 initially. ϵ is typically set to a very small value (10^{-7}).
RMP	$w_{t+1} = w_t - \frac{a}{\sqrt{S_t + \epsilon}} \cdot \frac{\partial L}{\partial w_t}$ $S_t = \beta S_{t-1} + (1-\beta) \left[\frac{\partial L}{\partial w_t} \right]^2$	S starts as 0 initially, $a = 0.001$, $\beta = 0.9$, and ϵ is chosen as 10^{-6} .
ADD	$w_{t+1} = w_t - \frac{\sqrt{D_{t-1}}}{\sqrt{S_t + \epsilon}} \cdot \frac{\partial L}{\partial w_t}$ $D_t = \beta D_{t-1} + (1-\beta) [\Delta w_t]^2$ $S_t = \beta S_{t-1} + (1-\beta) \left[\frac{\partial L}{\partial w_t} \right]^2$ $\Delta w_t = w_t - w_{t-1}$	S and D are initialized to 0, β is set to 0.95, and ϵ is chosen as 10^{-6} .
ADM	$W_{t+1} = W_t - \frac{a}{\sqrt{\hat{S}_t + \epsilon}} \cdot \hat{V}_t$ $\hat{V}_t = \frac{V_t}{1-\beta_1}$ $\hat{S}_t = \frac{S_t}{1-\beta_2}$ $V_t = \beta_1 V_{t-1} + (1-\beta_1) \frac{\partial L}{\partial W_t}$ $S_t = \beta_2 S_{t-1} + (1-\beta_2) \left[\frac{\partial L}{\partial W_t} \right]^2$	S and V are initially set to 0, $a = 0.001$, $\beta_1 = 0.9$, $\beta_2 = 0.999$, and ϵ is chosen as 10^{-8} .

ror (IAE), Integral of Time multiplied by Absolute Error (ITAE), and Mean Squared Error (MSE) are commonly used objective functions in control systems and optimization problems. IAE measures the system's error, i.e., the deviation between actual and desired values, and is used for minimization. ITAE evaluates the performance of a control system by considering both the error and response time. MSE measures the error quantity and is

Table 2. Objective Functions [25, 26].

Method Name	Formula
IAE	$\int_0^t e(t) dt$
ITAE	$\int_0^t t e(t) dt$
MSE	$\frac{1}{n} \int_0^t (e(t))^2 dt$

used for minimization as well. MSE is also often used as a performance metric in regression problems [25, 26]. Table 2 displays the mathematical formulas of the objective functions.

Feature Selection

In the field of machine learning, datasets are growing exponentially day by day and their quantitative numbers as well as qualitative features are increasing. The increase in the number of features in datasets can lead to different behaviors of machine learning methods. Even when behaviors do not change, it excessively increases the costs of methods. Dimension reduction techniques are used to reduce these costs. Feature Selection (FS) and Feature Extraction (FE) are the most common dimension reduction techniques. FE creates new and more effective features by using existing ones. FS, on the other hand, selects

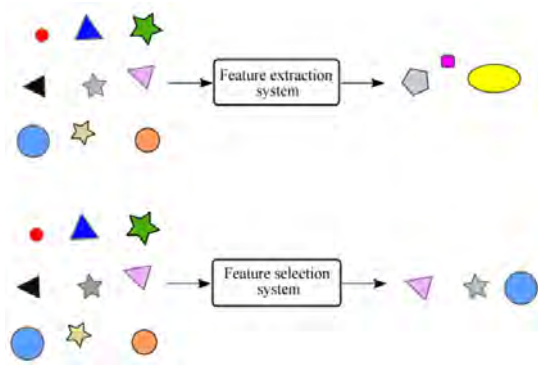


Figure 1. The Difference Between FE and FS [29].

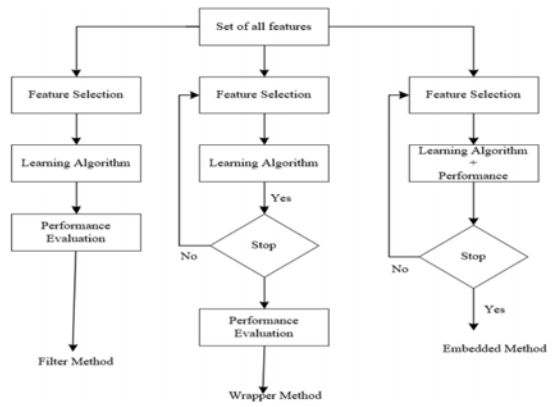


Figure 2. An Overview of FS Main Headings [27].

Table 3. Attributes of blood gas examination records for COVID-19 testing.

	1.	2.	3.	4.	686.	1255.					
Age	84	64	82	70	51	32	70	18					
Gender	E	K	K	E	E	E	E	K					
Base(B,ox)	-0.15	-1.50	7.90	0.00	5.10	0.70	-17.60	-0.70					
Base(Ecf)	1.25	-2.50	6.89	-3.90	6.90	2.70	-11.00	1.60					
Base(Ecf,ox)	1.15	-2.60	8.57	0.00	6.40	2.40	-11.80	1.00					
Ca ⁺⁺	1.04	0.94	1.08	1.05	1.45	1.20	1.30	1.23					
CHCO ₃	24.65	23.20	30.09	21.40	29.10	25.00	12.30	23.90					
Cl	104.75	108.00	106.00	106.00	95.00	106.00	110.00	103.00					
ctHb	13.95	14.50	13.43	12.20	12.90	16.30	18.30	14.30					
ctO ₂ e	16.85	18.40	18.14	14.40	8.60	13.20	1.80	7.00					
FHHb	9.93	7.80	2.66	13.30	50.30	36.30	92.20	63.20					
FMetHb	0.03	-0.60	0.55	0.70	0.70	0.40	0.50	0.70					
FO ₂ Hb	88.48	91.00	95.60	84.40	47.50	57.70	6.70	35.10					
Glukoz	139.75	100.00	129.83	105.00	124.00	129.00	154.00	110.00					
K ⁺	3.27	3.90	3.70	5.80	4.00	4.10	6.30	3.00					
Na ⁺	134.50	136.00	144.14	140.00	134.00	141.00	148.00	141.00					
p50e	28.53	25.42	24.00	27.22	27.77	25.60	39.92	28.81					
pCO ₂	54.10	28.80	40.31	34.70	40.10	47.60	103.00	45.40					
pCO ₂ (T)	54.10	28.80	40.31	34.70	40.10	47.60	103.00	45.40					
pH	7.35	7.47	7.49	7.39	7.49	7.38	6.93	7.38					
pH(T)	7.35	7.47	7.49	7.39	7.49	7.38	6.93	7.38					
pO ₂	76.15	61.80	95.12	53.00	27.20	30.70	13.10	22.90					
pO ₂ (T)	76.15	61.80	95.12	53.00	27.20	30.70	13.10	22.90					
sO ₂	89.90	92.10	97.30	86.40	48.60	61.40	6.80	35.70					
Result						Positive					Negative				

the features among the existing ones that have the most influence on the outcome. Therefore, instead of raw data, a dataset that is more effective on the results is provided as input data to machine learning methods. Using these methods, performance improvement and cost reduction can be achieved. The difference between FE and FS is shown in Fig. 1 [27-29].

FE is applied to data sets such as images and audio, while FS is applied to more sensitive data. Since the dataset used in the study does not involve image data and is related to the field of medicine, FS methods are employed. As seen in Fig. 2, FS is examined under three main headings (Filter, Wrapper, Embedded) [27, 29, 30].

Table 4. Features to be used in the MLR model.

Age	Base(B,ox)	Ca++	Result
84	-0.15	1.04	Positive
64	-1.50	0.94	Positive
82	7.90	1.08	Positive
70	0.00	1.05	Positive
...
...
61	2.00	1.06	Negative
60	7.41	1.05	Negative
51	5.10	1.45	Negative
32	0.70	1.20	Negative
...
...

Spiral methods are preferred because they take into account the dependence between features and have high accuracy performance from filter methods. There are three types of spiral methods used in regression or classification methods [27, 30].

Spiral methods have different methods such as Forward Selection, Backward Selection, and Stepwise (Exhaustive) Selection. In the Forward Selection method, the feature that most affects the performance of the machine learning method is selected from the feature pool, then the second most influential feature is selected, and so on until the feature selection reaches the stopping criterion. A stopping criterion is considered to be selecting all features with a P-value below 0.05. In the Backward Selection method, the opposite path of Forward Selection is followed. Feature selection begins by removing the feature that has the least impact on the performance of the machine learning method from all features. Then, the second least influential feature is removed. This process continues until all features with a P-value above 0.05 are removed to create the best feature subset. Stepwise Selection is a combination of both methods. Each feature is compared to all other features and selected for the best feature subset [27, 30, 31].

Problem Formulation

Table 3 displays the features of the dataset obtained from the hospital. The Blood Gas data set, where the MLR model is applied, is obtained upon an official request. This dataset consists of examination records conducted by Van Yüzüncü Yıl University Dursun Odabaş Medical Center between 01.11.2020 and 31.12.2020. The Blood Gas records contain 22 attributes (Base(B,ox), Base(Ecf), Base(Ecf,ox), Ca++, cHCO_3^- , C_i , ctHb, ctO_2e ,

FHHb, FMetHb, FO_2Hb , Glucose, K^+ , Na^+ , p50e, pCO_2 , $\text{pCO}_2(\text{T})$, pH, $\text{pH}(\text{T})$, pO_2 , $\text{pO}_2(\text{T})$, sO_2). Together with age and gender information as shown in Table 3, a dataset with 24 features is obtained. In the result section, there are labels indicating whether the COVID-19 virus is positive or negative. In other words, the obtained dataset has two classes (positive, negative). The positive class has a total of 109 samples (87 training, 22 testing), and the negative class has a total of 1146 samples (916 training, 229 testing), making a total of 1255 samples. In MLR models, a single point is initially selected for coefficients. These points are generally zero, one, or a randomly selected value. In the conducted study, a population is used for the initialization of coefficients.

Feature selection methods (Filter, Wrapper, and Embedded) are applied to the dataset in Table 3. The features that are common among the most effective ones obtained in all three methods (Age, Base(B,ox), Ca++) are shown in Table 4. The training and testing processes of MLR are conducted using these selected features.

The resulting function is formulated with the most effective features as shown in Eq. 1.

$$Y = \theta_1 X_{\text{Age}} + \theta_2 X_{\text{Base(B,ox)}} + \theta_3 X_{\text{Ca++}} \quad (1)$$

Y , X_{Age} , $X_{\text{Base(B,ox)}}$, $X_{\text{Ca++}}$ values are read from the dataset to obtain the coefficients θ_1 , θ_2 , θ_3 . These coefficients are generally initially set to 0 or 1 or randomly generated between two values. Using the obtained coefficients after the operations, the X input values are substituted in Equation 1 to obtain Y' (Y to the power of Y). The difference between the real value Y and the predicted value Y' constitutes our error amount.

Experimental Study

All modules of the conducted study are shown in Figure 3. After applying feature selection methods to the entire dataset, outputs are generated with six different optimization algorithms and three different objective functions. In other words, 6*3 outputs are compared, and the results are analyzed. Solving MLR problems requires finding a function using many inputs and their corresponding output values. Therefore, after the regression process, the most suitable values found represent a function that includes all input and output values, replacing the θ coefficients in Equation 1. To find appropriate values for these coefficients, an initial value is assigned, and the process is initiated. With this initial value, the Dik Inis optimization algorithms are used to gradually obtain the optimal θ coefficient.

In this study, it starts with stochastic initial coefficients because the aim is to reach a solution as quickly as possible.

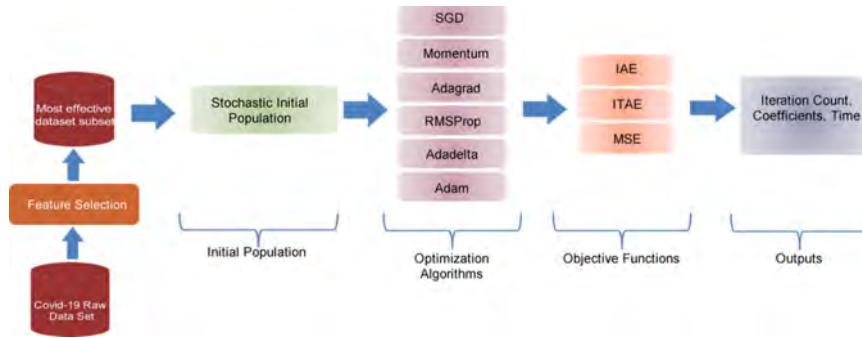


Figure 3. All modules of the study.

From the initial population, one candidate solution that is closest to the result must be selected to initiate the application. After individually processing all candidate solutions through optimization and objective functions once, the candidate solution with the lowest result is chosen to proceed. The obtained ideal candidate solution continues with regression steps for up to 1000 iterations. At the end of the regression process, the coefficients of the function that represents the entire dataset will have been determined.

RESULTS AND DISCUSSION

The outputs obtained from the application with a starting population size of 10 are listed in Table 5. In Table 5, the averages of the outputs obtained from 10 runs are compared. Here, the outputs of the applications using

different optimization algorithms and objective functions (θ_1 , θ_2 , θ_3 , and the number of iterations) are listed. Additionally, the "time" column of the table provides the processing times for each objective function for all optimization methods. Adadelta and Adagrad optimization algorithms achieve results with the lowest number of iterations for all objective functions. SGD, Momentum, and Adam optimization algorithms have high numbers of iterations for the IAE objective function. Among the objective functions, MSE reaches results with the lowest number of iterations for all optimization algorithms.

In Fig. 4, the errors and the number of iterations for the application using the IAE objective function with all optimization algorithms are shown graphically. Here, applications for all optimization algorithms are run 10 times, and the

Table 5. Results table for a population size of 10.

Obj. Func.	Opt. Alg.	Iterations Number	θ_1	θ_2	θ_3	Time
IAE	SGD	1000	0.3533127117	0.7155792544	0.9136478838	00:27:52
	MMT	1000	0.3539140773	0.7161656774	0.9141953364	
	ADG	1000	0.0000619687	0.0000620018	0.0000621926	
	RMP	1000	0.9425588422	0.9871959691	0.9895221032	
	ADD	1000	0.0000525305	0.0000527744	0.0000528254	
	ADM	1000	0.5689422754	0.4302199096	0.3704841926	
ITAE	SGD	1000	0.3532622052	0.7154840038	0.9135009433	00:32:59
	MMT	1000	0.3538630228	0.7160694295	0.9140472966	
	ADG	1000	0.0000614089	0.0000618772	0.0000618805	
	RMP	1000	0.9427011017	0.9867973079	0.9885063650	
	ADD	1000	0.0000525305	0.0000527744	0.0000528254	
	ADM	1000	0.5675193230	0.4295664937	0.3697876234	
MSE	SGD	1000	0.3532656701	0.7154717486	0.9135007489	00:28:45
	MMT	1000	0.3538664716	0.7160571368	0.9140470657	
	ADG	1000	0.0000614950	0.0000614423	0.0000614426	
	RMP	1000	0.9447178907	0.9855191028	0.9872083973	
	ADD	1000	0.0000525305	0.0000527744	0.0000528254	
	ADM	1000	0.5678662791	0.4290865789	0.3693919793	

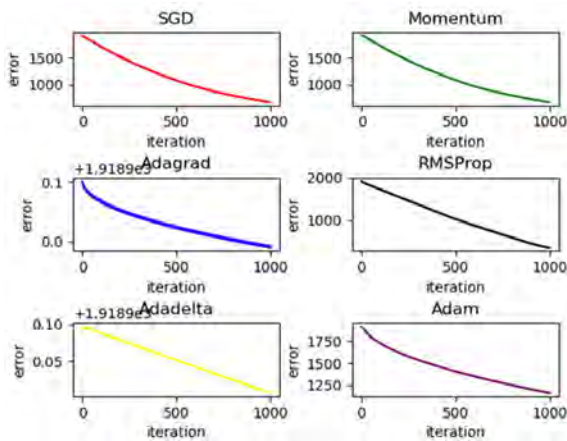


Figure 4. Outputs with the IAE objective function.

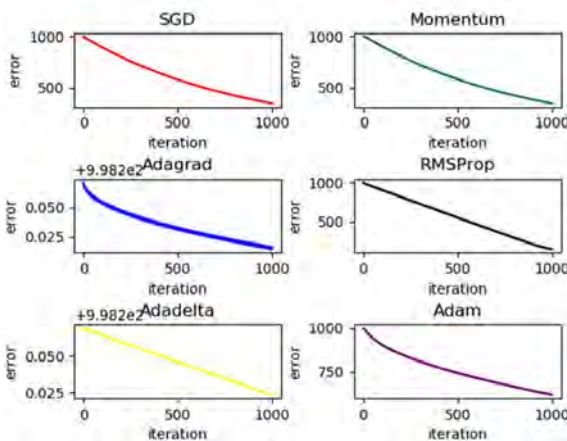


Figure 5. Outputs with the ITAE objective function.

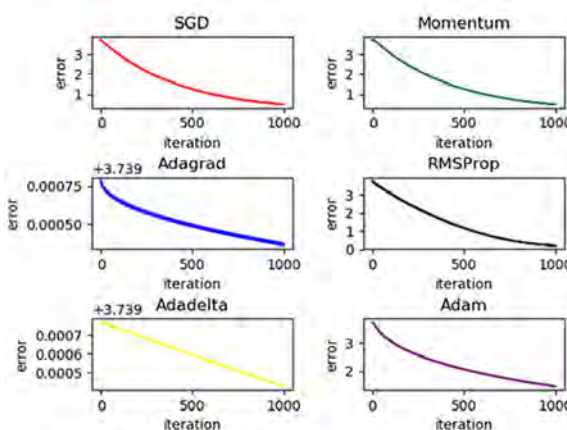


Figure 6. Outputs with the MSE objective function.

results are presented graphically. Fig. 5 displays the results of applications using the ITAE objective function and different optimization methods graphically.

Fig. 6 shows the results of the applications using the MSE objective function and different optimization methods graphically.

Results obtained for different optimization algorithms based on stochastic initialization and different objective functions are shown in Figs 4, 5, and 6. As seen in the figures, very similar results are obtained. Table 5 provides a comparative view of the coefficients, iteration counts, and processing times obtained from experiments with different parameters. The obtained coefficients are used for testing, i.e., a validation step is performed. The aim of the validation section is to confirm the accuracy of the obtained coefficients. Here, the success rates of the coefficients obtained with 251 test data (229 negative and 22 positive) are analyzed. Using various optimization algorithms and objective functions, many coefficient vectors $(\theta_1, \theta_2, \theta_3)$ are obtained. With six optimization algorithms (SGD, MMT, ADG, RMP, ADD, ADM) and three objective functions (IAE, ITAE, MSE), 6x3 coefficient vectors are obtained. When the values are put together, a matrix of size 18x3 is formed. By substituting each row of the 18-row matrix into Eq. 1 separately, processing is performed with the 251-test data set. As a result of the processing, 18x251 Y' (predicted results) are obtained. The total error rates of the obtained estimated data are calculated using the MAPE method. In addition, correct prediction counts are analyzed at certain threshold values (20%, 30%, 40%). If the error is below these threshold values, it is considered a correct prediction; if it is above, it is considered an incorrect prediction. Table 6 shows the success rates of all the studies obtained through thresholding and the MAPE method.

When examining the success rates, it is observed that the performance of the SGD, MMT, and RMP algorithms used with the IAE objective function is successful. In particular, RMP exhibits a success rate ranging from 58% to 91.23% across all measurement methods.

CONCLUSION

The aim of this study is to obtain a testing method for the COVID-19 pandemic. Individuals' COVID-19 test results, whether positive or negative, are determined using blood gas values. Multivariate linear regression modeling is carried out with a stochastic initial population method, six different optimization algorithms, and three different objective functions.

The method for generating the initial population is a crucial step in multivariate linear regression and all other machine learning algorithms, yet it remains an area with limited research. The most commonly used method to date is the traditional stochastic initialization method. In studies initiated with the traditional stochastic initialization method, the initial populations and obtained outputs always differ. Therefore, studies initiated with stochastic methods need to be run multiple times (e.g., 10, 50, or 100 times), and

Table 6. Success Rates of the Studies.

Initial Pop	Objective Func.	Opt. Alg.	Threshold			MAPE
			20% Success Rate	30% Success Rate	40% Success Rate	Success Rate (%)
Stokastik	IAE	SGD	3.187	21.513	73.705	64.71
		MMT	3.585	21.912	74.103	64.75
		ADG	0	0	0	0.01
		RMP	58.565	79.282	91.235	77.90
		ADD	0	0	0	0.01
		ADM	5.577	6.772	7.968	42.67
	ITAE	SGD	3.187	21.513	73.705	64.71
		MMT	3.585	21.912	73.705	64.74
		ADG	0	0	0	0.01
		RMP	58.565	79.282	90.836	77.88
		ADD	0	0	0	0.01
		ADM	5.577	6.772	7.9681	42.60
MSE	SGD	3.187	21.513	73.705	64.71	
	MMT	3.585	21.912	73.705	64.74	
	ADG	0	0	0	0.01	
	RMP	58.565	78.884	90.836	77.85	
	ADD	0	0	0	0.01	
	ADM	5.577	6.772	7.968	42.57	

the average values of the obtained outputs are presented in the literature, which is more acceptable. In terms of processing time, it is observed that the IAE objective has a slight advantage in the study. Additionally, the RMP optimization algorithm is found to have a success rate ranging from 58% to 91.23% across all measurement methods. Thus, a success rate of 91.23% is achieved in the modeling aimed at the COVID-19 pandemic. The desired outcome of this study is to contribute to the field of healthcare.

In future studies, changing the modeling method is aimed at achieving more successful results. Contributions to the field of healthcare are crucial in today's world. Therefore, one of the fundamental duties of every individual should be to serve society and humanity.

ACKNOWLEDGEMENT

The author received financial support from Van Yüzüncü Yıl University Scientific Research Projects Coordination Unit for the research, authorship and/or publication of this article.

CONFLICT OF INTEREST

Authors approve that to the best of their knowledge, there is not any conflict of interest or common interest with an institution/organization or a person that may affect the

review process of the paper.

The authors of this study declare that they have received an ethical permission from the Van Yüzüncü Yıl University Dursun Odabaşı Medical Center dated 20.05.2021 and numbered 52545.

AUTHOR CONTRIBUTION

Faruk Ayata: Conceptualization, Methodology, Software, Validation, Writing- original draft. Ebubekir Seyyarer: Data curation, Visualization, Investigation, Supervision.

References

1. Raji P, Lakshmi G. R. D. Covid-19 pandemic analysis using regression. medRxiv. 2020. doi: 10.1101/2020.10.08.20208991.
2. Bandil S, Rathore S. Study of Haematological Parameters in Malaria. Asian J. Med. Res. 2019; volume(8): PT08-PT12. doi: 10.21276/ajmr.2019.8.3.pt3.
3. Demircan S. Öksürük Sesi Kayıtlarından Spektral Özellikler ile Otomatik COVID-19 Tespiti. Avrupa Bilim ve Teknoloji Dergisi. 2022. Ejosat Special Issue 2022 (ICAENS-1): 492-495. DOI: 10.31590/ejosat.1083052
4. Demir F. B. And Yılmaz, E. X-Ray Görüntülerinden COVID-19 Tespiti için Derin Öğrenme Temelli Bir Yaklaşım. Avrupa Bilim ve Teknoloji Dergisi. 2021. Ejosat Special Issue 2021 (RDCONF): 627-632. DOI: 10.31590/ejosat.1039522
5. Taş F, Özudođru O, & Bolatlı G. Bilgisayarlı Tomografi Bulguları

- Negatif Olan Covid-19 Hastalarının; Epidemiyolojik, Klinik ve Laboratuvar Sonuçları Açısından Değerlendirilmesi. *Selçuk Sağlık Dergisi*. 2021. Covid-19 Özel:18-32. Retrieved from <https://dergipark.org.tr/en/pub/ssd/issue/57170/757740>
6. Şahin Gökçe H, Özensoy Güler Ö, Şimşek E, Karagülleoğlu Z, and Çarhan A. COVID-19 Hastalarında Yeni Bir Yaklaşım Olarak Oksihemogloblin Karboksihemogloblin, Kan Gazı Değerlerinin İncelenmesi. *Longitudinal Bir Çalışma. Türk Yoğun Bakım Hemşireleri Derneği Yayın Organı*. 2022; 26 (3): 92-99.
 7. Dokeroglu T, Sevinc E, Kucukyilmaz T, and Cosar A. A survey on new generation metaheuristic algorithms. *Comput. Ind. Eng.*, 2019. doi: 10.1016/j.cie.2019.106040.
 8. Villarrubia G, De Paz J. F, Chamoso P, and De la Prieta F. Artificial neural networks used in optimization problems. *Neurocomputing*. 2018. doi: 10.1016/j.neucom.2017.04.075.
 9. Pandey M, Zakwan M, Sharma P. K, and Ahmad Z. Multiple linear regression and genetic algorithm approaches to predict temporal scour depth near circular pier in non-cohesive sediment. *ISH J. Hydraul. Eng*. 2020. doi: 10.1080/09715010.2018.1457455.
 10. Shihabudheen K. V, Mahesh M, and Pillai G. N. Particle swarm optimization based extreme learning neuro-fuzzy system for regression and classification. *Expert Syst. Appl*. 2018. doi: 10.1016/j.eswa.2017.09.037.
 11. Zhijian L, Guangyao F, Dekang S, Di W, Jiacheng G, Shicong Z, Xinyan Y, Xianping L, Lei A. A novel distributed energy system combining hybrid energy storage and a multi-objective optimization method for nearly zero-energy communities and buildings. *Energy*. 2022; Volume (239). ISSN 0360-5442.
 12. On O, AE-S. E, Mohamed T, ve Abualigah L. Ebola Optimizasyon Arama Algoritması: Doğadan Esinlenen Yeni Bir Metasezgisel Optimizasyon Algoritması. *IEEE Access*. 2022; Volume (10): 16150-16177. doi: 10.1109/ACCESS.2022.3147821.
 13. Ponce-Ortega J.M, Hernández-Pérez L.G. Optimization of Process Flowsheets through Metaheuristic Techniques. Springer, UK. 2019.
 14. Güler E, & Yerel Kandemir S. Lineer ve Kübik Regresyon Analizleri Kullanılarak OECD Ülkelerinin CO2 Emisyonlarının Tahminlemesi. *Avrupa Bilim ve Teknoloji Dergisi. Ejosat Special Issue 2022 (ICAENS-1)*. 2022; 175-180. DOI: 10.31590/ejosat.1079187
 15. Özen N. S, Saraç S, & Koyuncu M. COVID-19 Vakalarının Makine Öğrenmesi Algoritmaları ile Tahmini: Amerika Birleşik Devletleri Örneği. *Avrupa Bilim ve Teknoloji Dergisi. Ejosat*. 2021; 134-139. DOI: 10.31590/ejosat.855113
 16. Saadatmand S, Salimifar K, Mohammadi R. Predicting the necessity of oxygen therapy in the early stage of COVID-19 using machine learning. *Med Biol Eng Comput*. 2022; 60, 957-968. <https://doi.org/10.1007/s11517-022-02519-x>
 17. Mohan S, A J, Abugabah A, M A, Kumar Singh S, Kashif Bashir A, Sanzogni L. An approach to forecast impact of Covid-19 using supervised machine learning model. *Softw Pract Exp*. 2021 Apr 1:10.1002/spe.2969. doi: 10.1002/spe.2969.
 18. Pinter G, Felde I, Mosavi A, Ghamisi P, & Gloaguen R. COVID-19 pandemic prediction for hungary; a hybrid machine learning approach. *Mathematics*. 2020; Volume 8(6): 890. <https://doi.org/10.3390/math8060890>
 19. Elaziz M. A, Hosny K. M, Salah A, Darwish M. M, Lu S, & Sahlol A. T. New machine learning method for image-based diagnosis of COVID-19. *PLoS One*. 2020; Volume 15(6). <https://doi.org/10.1371/journal.pone.0235187>
 20. Haji S. H, & Abdulazeez A. M. Comparison of optimization techniques based on gradient descent algorithm: A review. *PalArch's Journal of Archaeology of Egypt/Egyptology*. 2021; Volume 18(4): 2715-2743.
 21. Iqbal I, Odesanmi G. A, Wang J, & Liu L. Comparative Investigation of Learning Algorithms for Image Classification with Small Dataset. *Applied Artificial Intelligence*. 2021; Volume 35(10): 697-716. <https://doi.org/10.1080/08839514.2021.1922841>
 22. Song C. Y, Pons A, & Yen K. AG-SGD: Angle-Based Stochastic Gradient Descent. *Ieee Access*. 2021; Volume (9): 23007-23024. <https://doi.org/10.1109/Access.2021.3055993>.
 23. Truong T. T, & Nguyen H. T. Backtracking Gradient Descent Method and Some Applications in Large Scale Optimisation. Part 2: Algorithms and Experiments. *Applied Mathematics and Optimization*. 2021; Volume 84(3): 2557-2586. <https://doi.org/10.1007/s00245-020-09718-8>
 24. Zaman S. M, Hasan D. M, Sakline R. I, Das D, & Alam M. A. A Comparative Analysis of Optimizers in Recurrent Neural Networks for Text Classification. 2021 *Ieee Asia-Pacific Conference on Computer Science and Data Engineering (Csde)*. 2021. <https://doi.org/10.1109/Csde53843.2021.9718394>
 25. Abdul-Adheem W. R, Ibraheem I. K, Humaidi A. J, Alkhayyat A, Maher R. A, Abdulkareem A. I, & Azar A. T. Design and analysis of a novel generalized continuous tracking differentiator. *Ain Shams Engineering Journal*. 2021.
 26. Seyyarer E, Karci A, & Ates A. Effects of the stochastic and deterministic movements in the optimization processes. *Journal of the Faculty of Engineering and Architecture of Gazi University*. 2022; Volume37(2):949-965. <https://doi.org/10.17341/gazimmd.887976>
 27. Venkatesh B, & Anuradha J. A review of feature selection and its methods. *Cybernetic and information Technologies*. 2019; Volume 19(1): 3-26.
 28. Khair U. M, & Dhanalakshmi R. Stability of feature selection algorithm: A review. *Journal of King Saud University-Computer and Information Sciences*. 2022; Volume 34(4): 1060-1073.
 29. Remeseiro B, & Bolon-Canedo V. A review of feature selection methods in medical applications. *Computers in biology and medicine*. 2019; Volume (112).
 30. Zebari R, Abdulazeez A, Zeebaree D, Zebari D, & Saeed J. A comprehensive review of dimensionality reduction techniques for feature selection and feature extraction. *Journal of Applied Science and Technology Trends*. 2020; Volume 1(2): 56-70.
 31. Şener Y. Makine Öğrenmesinde Değişken Seçimi (Feature Selection) Yazı Serisi: Sarmal (Wrapper) Yöntemler ve Python Kodları. 2020. Erişim Adresi: <https://iyigitsener.medium.com>

Microstructural Evolution and Mechanical Properties of Y Added CoCrFeNi High-entropy Alloys Produced by Arc-melting

Gokhan Polat^{1*}  Hasan Kotan² 

¹Izmir Katip Celebi University, Metallurgical and Materials Engineering, Izmir, Türkiye

²Bursa Technical University, Metallurgical and Materials Engineering, Bursa, Türkiye

ABSTRACT

The CoCrFeNi high entropy alloy (HEA) with face-centered cubic (FCC) crystal structure exhibits excellent ductility values even at cryogenic temperatures. However, since this HEA is relatively weak in strength, it may not meet the requirements of industrial applications in terms of strength-ductility trade-off. Therefore, the systematic addition of yttrium (Y) into CoCrFeNi HEA was investigated in the present study to increase the strength by solid solution and second phase strengthening. The HEAs were produced by vacuum arc melting, suction casting, and subsequent homogenization at 1150 °C for 24 h. The structural development of the HEAs was investigated by using the X-ray diffraction (XRD) technique which revealed the formation of a solid solution phase and CaCu5-type hexagonal structure (HS) second phase. The corresponding microstructure of the HEAs was examined under a scanning electron microscope (SEM) revealing the transformation of the microstructure from elongated grains to nearly equiaxed grains with the increase of Y content from 2 at. % to 4 at. %. The mechanical properties of the HEAs were investigated by using hardness and compression tests. The results exhibited a dramatic increase in the hardness from 143 (±2) HV to 335 (±7) HV and in the yield strength from 130 MPa to 1025 MPa with 4 at. % Y addition. Our study has revealed that the addition of rare earth Y element results in further development in the strength of the CoCrFeNi for potential engineering applications.

Keywords:

High entropy alloys; Strength; Rare earth addition; Second phase

INTRODUCTION

High entropy alloys (HEAs) are a novel class of emerging materials with great potential to be applied in a wide range of engineering applications due to their unique comprehensive properties and structures (1, 2). Differing from conventional alloys, HEAs usually contain five or more principal elements in equiatomic or near-equiatomic ratios which causes an increase in the mixing entropy (ΔS_{mix}) of the alloys (3). Accordingly, HEAs are more likely to form simple solid solution structures such as face-centered cubic (FCC), body-centered cubic (BCC), and hexagonal close-packed (HCP) because of the reduced Gibbs free energy (4–6).

FCC-type HEAs have received much attention as compared to conventional alloys due to their exceptional properties such as fracture toughness at cryogenic

temperatures (7), and remarkable ductility (8). The well-known equiatomic CoCrFeNi HEA with a single FCC crystal structure is the starting point of numerous studies in the field of alloy development. The reported yield strength and ultimate tensile strength of the as-cast CoCrFeNi HEA are 160 MPa and 718 MPa, respectively (9). In addition, this HEA shows an excellent elongation to failure of over 50 % suggesting outstanding uniform deformation along with high strain hardening ability (9). This feature provides a great base for further strengthening the ductile HEAs. However, recent research indicates that a HEA matrix alone, particularly the single-phase FCC structure, is insufficiently robust for engineering applications at ambient and increased temperatures (10). Thus, the development of the mechanical properties of single-phase FCC CoCrFeNi HEAs has received great attention over the past decade (11). The main strategies

Article History:

Received: 2023/09/19

Accepted: 2024/01/23

Online: 2024/03/31

Correspondence to: Gökhan Polat,
Izmir Katip Çelebi University, Metallurgical
and Materials Engineering, 35620, Izmir,
TÜRKİYE

E-Mail: gokhan.polat@ikc.edu.tr;

Phone: +90 232 329 3535/3830.

This article has been checked for similarity.



This is an open access article
under the CC-BY-NC licence

<http://creativecommons.org/licenses/by-nc/4.0/>

Cite as:

Polat G, Kotan H. Microstructural Evolution and Mechanical Properties of Y Added CoCrFeNi High-entropy Alloys produced by Arc-melting. Hittite Journal of Science and Engineering 2024;11(1):25-31. doi:10.17350/hjse19030000328

to enhance the mechanical properties of the HEAs include severe plastic deformation (12), tuning the composition of the main alloy (13–15), solid solution hardening by the addition of solute atoms (16), and second-phase hardening (17–19). It is widely known that adding additional alloying elements, such as Al, Mn, and Cu at low concentrations to the base CoCrFeNi alloy destabilizes the single FCC phase and promotes phase (20, 21). For instance, Wang et al. (22) reported that the presence of Al in Al_{0.3}CoCrFeNi HEA produced by the magnetic levitation induction technique and subsequent annealing at 800 °C resulted in the formation of a B2 phase. The formation of the B2 phase in the FCC matrix caused outstanding mechanical properties of ~870 MPa yield strength and ~1060 MPa tensile strength as well as the ductility of ~26 %. In addition, Chen et al. (23) produced (CoCrFeNi)_{100-x}(ZrC)_x (x = 0-8, at. %) HEAs by arc-melting and investigated the strengthening mechanisms. They showed that the amounts of Laves and ZrC phases were increased with the increasing amounts of Zr and C additions, resulting in an improvement of the yield strength from 154 MPa to 374 MPa owing to the second phase strengthening mechanism.

The rare earth (RE) elements, often known as "industrial vitamins" due to their exceptional physical and chemical qualities, play a significant role in enhancing the quality of products and raising manufacturing performance. Because of their beneficial effects on molten steel purification and inclusion modification, additions of RE elements into steels have been a popular strategy for tailoring microstructure and improving mechanical performance (24–26). In addition, Y addition caused a substantial increase in the hardness of Fe-Al and Ni-Al-based superalloys (27, 28).

Similarly, it is shown in the literature that the mechanical properties of the HEAs could be enhanced by the addition of RE elements such as Y and Zr. For instance, Polat et al. (18) produced 1 and 4 at. % Y added CoCrFeNi HEAs by mechanical alloying followed by annealing and investigated the mechanical properties. They showed that an increase in the Y content caused a dramatic rise in the hardness from 215 to 435 HV after annealing at 1100 °C. Similarly, Tekin et al. (17) studied the effect of 1 and 4 at. % Zr addition into CoCrFeNi HEAs by mechanical alloying and subsequent annealing at 1100 °C. They reported a systematic increase in the hardness from 315 to 347 HV with the addition of 1 and 4 at. % Zr, respectively. These results demonstrate that the mechanical properties of HEAs could be further enhanced by the addition of RE elements synthesized by mechanical alloying. However, an inspection of the literature shows a lack of studies that utilized RE elements to increase the mechanical properties of the CoCrFeNi HEAs by melting techniques.

Table 1. The nominal compositions of the base, 2Y, and 4Y HEAs.

HEA	Compositions (at. %)				
	Co	Cr	Fe	Ni	Y
Base	25	25	25	25	-
2Y	24.5	24.5	24.5	24.5	2
4Y	24	24	24	24	4

In the present study, CoCrFeNi, (CoCrFeNi)₉₈Y₂, (CoCrFeNi)₉₆Y₄ HEAs were produced by vacuum arc melting to investigate the development of the mechanical properties due to the solid solution strengthening of solute Y atoms in the FCC crystal structure and formation of second phases. The formations of the phases were investigated experimentally by XRD, SEM, and EDS analyses along with the mechanical properties and interpreted thermodynamically.

MATERIAL AND METHODS

The CoCrFeNi, (CoCrFeNi)₉₈Y₂, (CoCrFeNi)₉₆Y₄ HEAs with the nominal compositions provided in Table 1 were produced by vacuum arc melting technique under argon atmosphere. For convenience, they are referred to as base, 2Y, and 4Y, respectively. The elemental Co, Cr, Fe, Ni, and Y chunks, each with purities higher than 99.9 wt. % were used to obtain the metal mixtures based on the nominal compositions. A total of 3 grams of metal chunk mixtures for each composition were charged into Edmund Buhler MAM-1 copper hearth arc-melter to produce ingots. The HEA ingots were flipped and re-melted at least 3 times to achieve the chemical homogeneity in the microstructure. Finally, the alloys were suction cast into a water-cooled cylindrical copper mold with a diameter of 4 mm. The suction-casted HEAs were homogenized at 1150 °C for 24 h in a tube furnace with a controlled atmosphere.

The structural characterizations of the HEAs were conducted by using a Panalytical Empyrean X-ray diffractometer with Cu-K α radiation source ($\lambda=1.5406$ Å). The X-ray diffraction (XRD) characterization was conducted with a scanning rate of 1°/min between 35-100° values.

The relative intensity ratio (RIR) method is used to determine the percentages of the hexagonal structure (HS) phases based on the XRD analyses as shown in the following equation (29, 30):

$$\frac{V_{FCC}}{V_{HS}} = \frac{I_{(hkl)FCC}}{I_{(hkl)HS}} \cdot \frac{R_{HS}}{R_{FCC}} \quad (1)$$

where v and I are the volume fraction and intensity of the most intense (hkl) peak, respectively. R-value of any phase a is given by (29–31):

$$R_{\alpha} = \frac{M_{(hkl)\alpha} \cdot LP_{(hkl)\alpha} \cdot |F_{(hkl)\alpha}|^2}{V_{\alpha}^2} \quad (2)$$

where M, LP, F, and V are the multiplicity factor, Lorentz-polarization factor, structure factor, and volume of the unit cell, respectively.

The HEAs were etched by using a fresh aqua regia solution (a mixture of nitric acid and hydrochloric acid with a molar ratio of 1:3) for 1-2 min. The microstructural characterization and energy dispersive spectroscopy (EDS) were performed by using Hitachi SU1510 scanning electron microscope (SEM) with the Oxford Instruments x-act detector.

Hardness tests were conducted to determine the relationship between microstructure and mechanical properties of the HEAs as a function of Y content. The micro Vickers tests were carried out on the cylindrical 4 mm HEAs by using a load of 4.903 N (0.5 kgf) and a dwell duration of 10 sec at room temperature. At least 5 measurements were taken from each sample and their average was used for the corresponding hardness values. The compression tests were performed at room temperature using an INSTRON 5582 universal testing machine with a 10-ton capacity at a strain rate of 10^{-4} s^{-1} according to ASTM E9-09 standard. The samples were prepared by adjusting their height to be 1.5-2 times the diameter. To ensure the reliability of the test results, three samples were tested for each sample set.

RESULTS AND DISCUSSION

Structural and Microstructural Evolution of the HEAs

Fig. 1 shows the XRD patterns of the HEAs after homogenization at 1150 °C for 24 h. It should be noted that the homogenization duration and temperature were determined based on previous studies and $\sim 0.7T_m$, respectively, where T_m represents the theoretical melting points of the HEAs calculated through thermo-physical calculations (32, 33). The FCC phase is present in all the alloys, as seen by the (111), (200), (220), and (311) reflections of the FCC crystal structure. The base HEA consists of only these reflections in the XRD pattern, while additional reflections corresponding to a simple hexagonal structure (HS) were detected with Y additions. The formation of the HS could be attributed to the reaction between Y and Ni to form a CaCu_5 type Ni-Y rich phase with the P6/mmm space group, which agrees well with the previous reports indicated by Zhang et al. (26) and Zhou et al. (34). Due to the limited solubility of Y in Ni with a value of 0.4 at. % cause the formation of intermetallic compounds instead of the solid solution formation (35). In addition, the large negative enthalpy of mixing (ΔH_{mix}) value of -31

Table 2. Enthalpy of mixing (ΔH_{mix} , kJ/mol) values for the atom pairs in the HEAs (38).

	Co	Cr	Fe	Ni	Y
Co	0	-4	-1	0	-22
Cr		0	-1	-7	11
Fe			0	-2	-1
Ni				0	-31.0
Y					

kJ/mol for the Ni-Y pair (Table 2) triggers the reaction between these elements as compared to the remaining elements in the HEAs (18). Xu et al. (36) showed that ΔH_{mix} plays a critical role in the formation of the solid solution or intermetallic phases. The large negative values of ΔH_{mix} cause the increase in the bonding strength between the element pairs owing to their proper chemical reaction (37).

The increasing Y content from 2 at. % to 4 at. % raised the peak intensities of the HS phase suggesting the increase in the HS phase. In addition, the increasing Y content caused a shift towards a lower angle, as can be seen clearly in (311) reflection (Fig. 1) of the FCC phase. The decrease in the angles of the peak positions could be attributed to the increase in the lattice parameter of the HEAs due to the increase in the atomic radius of Y. That is, the increasing dissolution of the Y element in the HEAs causes a lattice distortion in the HEAs as pointed out by Zhang et al. (26).

The SEM images of the 2Y and 4Y HEAs are provided in Fig. 2. As can be deduced from the figure, the increasing Y content changes the shape of the etched region from elongated grains to nearly equiaxed grains. That is, the further addition of the Y element from 2 at. % to 4 at. % into the HEA results in the dendritic microstructure due to the increasing segregation into interdendritic regions. The frontal segrega-

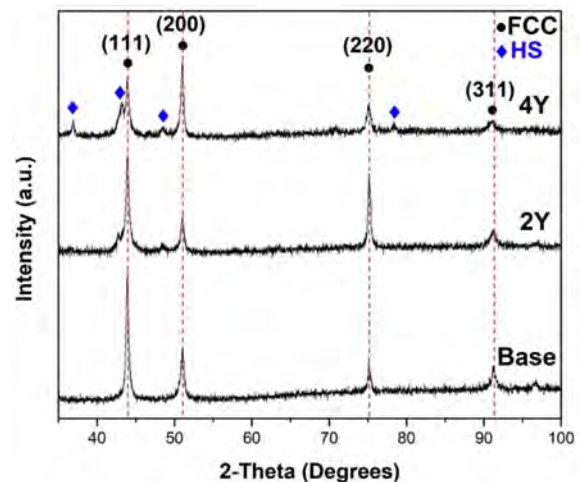


Figure 1. XRD patterns of the base, 2Y, and 4Y HEAs.

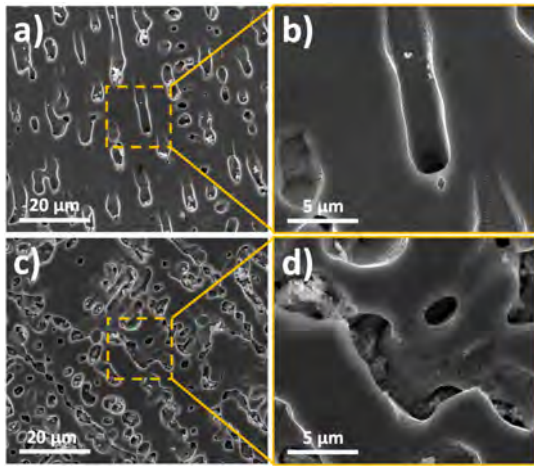


Figure 2. SEM images of 2Y HEA a) low magnification, b) high magnification. SEM images of 4Y HEA a) low magnification, b) high magnification.

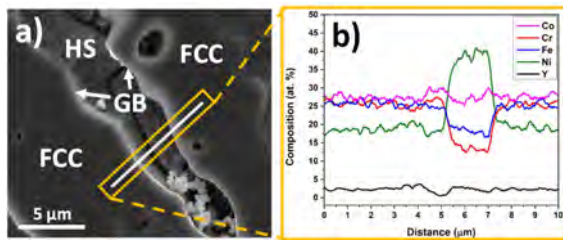


Figure 3. a) SEM image b) Corresponding EDS line scanning of etched 4Y HEA.

tion of the solute atoms in the solid-liquid interface causes a compositional change at the interface resulting in the formation of primary dendrites upon the solidification (39).

The SEM image and EDS line scanning provided in Fig. 3 show the compositional distribution between the matrix and second phase in the microstructure of the etched 4Y HEA. It should be noted that since the microstructure consists of dual phases of FCC and HS as shown with the XRD analyses (Fig. 1), the second phase could be indexed as HS. The EDS data provided in Fig. 3b shows that the FCC pha-

se is responsible for the almost homogeneously distributed areas of Co, Cr, and Fe with average values of around 27 at. %. In addition, the FCC matrix includes the homogeneously distributed Ni content with a value of ~ 17.5 at. %. This value is well below the nominal composition of the 4Y HEA having 24 at. % Ni in it. On the other hand, as can be seen in Fig. 3b, the Ni content reaches to a value of 40 at. % in the interdendritic regions, while the Co, Cr, and Fe elements deplete in this region. This suggests the segregation of the Ni element into the interdendritic region along with Y. In addition, the depletion of both Ni and Y elements could be seen in the grain boundary (GB) (Fig. 3a) of the FCC and HS phases.

It should be noted that although an increasing amount of Y could be expected in the interdendritic regions, the etching process decreases their amount. Therefore, detailed EDS analyses were conducted on the unetched 4Y HEA to reveal the exact elemental distribution of the FCC (matrix) and HS (segregated phase) as shown in Fig. 4. These results suggest the similar elemental distribution of Co, Cr, and Fe within the FCC matrix consistent with the EDS line scanning results. However, the compositions of Ni and Y elements in the HS phase reach values of 41.3 and 17.5 at. %, respectively, which is in line with the XRD results indicating the formation of the HS phase.

The Evolution of Mechanical Properties

The influence of the Y addition on the mechanical properties was investigated with the correlation of the HS phase formed in the microstructure. The hardness values and compression properties of the HEAs including yield stress ($\sigma_{0.2}$), fracture/peak stress (σ_p), and compressive strain to fracture (ϵ), are provided in Fig. 5 and summarized in Table 3. As seen in Fig. 5a, the amount of HS phase in the FCC matrix of the HEAs increased from 0 to 34 vol. % with the addition of 4 at. % Y, and the corresponding

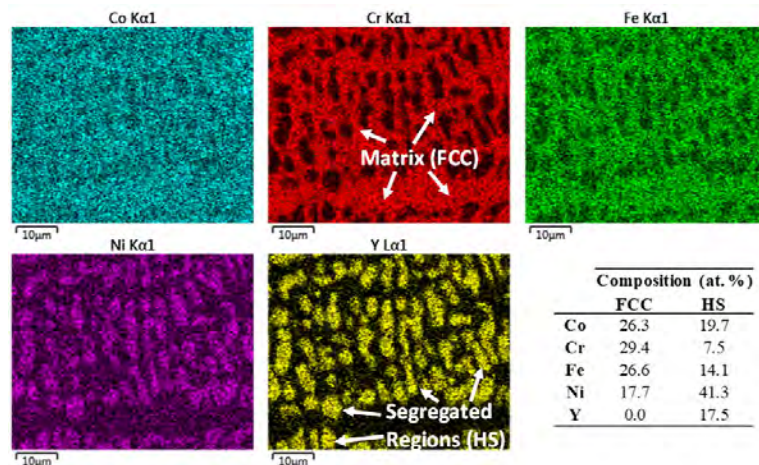


Figure 4. Mapping and point EDS analyses of unetched 4Y HEA.

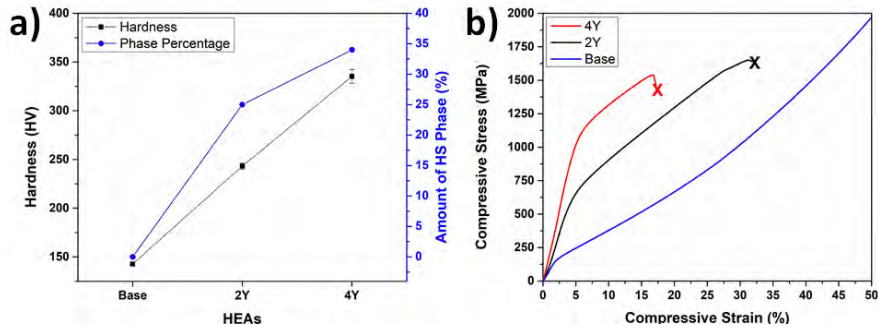


Figure 5. a) Hardness and amount of the HS phase in the HEAs as a function of composition, b) Compressive stress-strain curves of the HEAs.

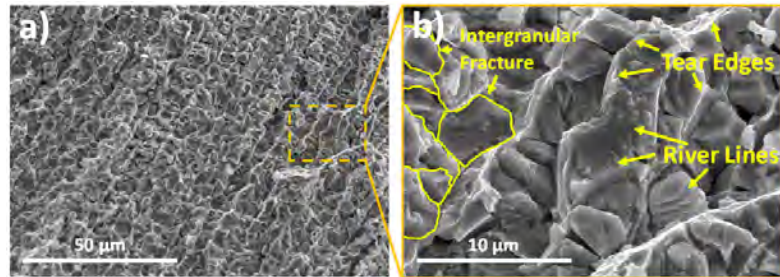


Figure 6. SEM images showing the fracture surface of the 4Y HEA after compression tests a) 1000x, b) 5000x.

hardness values were raised from 143 (± 2) HV to 335 (± 7) HV. In addition, the increasing Y content from 0 at. % to 4 at. % caused a dramatic increase in the yield strength from 130 MPa to 1025 MPa. On the other hand, the increase in the Y content from 2 at. % to 4 at. % decreased the compressive strain from 32 % to a value of around 16.5 %. It should be noted that the base HEA demonstrated high ductility and high strain hardening; its strength increased over 1960 MPa and it showed no signs of cracking up to compressive deformation of 50 %. Nevertheless, as can be deduced from the results, the formation of the HS phases plays a critical role in the improvement of the mechanical properties of the HEAs. These findings are in agreement with previous studies (26, 40, 41). The increased mechanical properties with the addition of alloying elements are generally divided into two categories; solid-solution strengthening and second-phase strengthening (14, 42, 43). Firstly, as explained in XRD analysis results (Fig. 1), the addition of Y causes a shift in the positions of the FCC reflections towards the lower angles due to the dissolution of Y in the matrix. This suggests a lattice distortion in the FCC crystal structure, and hence, an inc-

crease in the mechanical properties (44) due to the much larger atomic radius of Y as compared to the elements in the matrix (45). Secondly, the formation of the second phase causes a dramatic increase in the mechanical properties of the HEAs as reported in the previous studies (14, 32, 42). In the present study, the addition of excess Y into base HEA resulted in the formation of the HS phase in the microstructure. This causes an additional contribution to the increase of the mechanical properties due to the hard nature of the HS phase. The decrease in the available slip systems in the HS phases compared to the FCC results in the production of more brittle but stronger alloys (26). Therefore, the increasing amount of the HS phases up to 34 vol. % along with the solid solution strengthening has a vital contribution to the mechanical properties of the investigated HEAs.

The compression test results showed that Y addition caused the change in the failure mechanism of the HEAs. Therefore, the fracture morphology of the 4Y HEA was investigated under SEM to reveal the effect of Y on the fracture mode as shown in Fig. 6. As can be seen, although there are some river lines and smooth facets indicating the appearance of transgranular fractures, the intergranular dominated fracture was observed in the HEA due to the formation of hard and brittle HS phase in the intergrain regions resulting in the weakness of the intergrain regions (27, 46). In addition, the formation of tear edges in the fracture surface of the HEA shows relatively ductile behavior of the corresponding regions, which is consistent with what has been found in previous studies (32, 47). That is, combined with the above-mentioned results, it can be inferred that a

Table 3. Hardness and compressive properties of the base, 2Y and 4Y HEAs, and the amount of HS phase in the HEAs. *The base HEA demonstrated no fracture over the compressive strain value of 50 % and the compressive stress was continuously raised.

HEA	Amount of HS (%)	Hardness (HV)	$\sigma_{0.2}$ (MPa)	σ_p (MPa)	ϵ (%)
Base	0	143 (± 2)	130	>1960*	>50*
2Y	25	243 (± 3)	562	1650	31.5
4Y	34	335 (± 7)	1025	1538	16.5

mixed mode of fracture indicating quasi-cleavage fracture was observed in 4Y HEA.

CONCLUSION

In the present study, The CoCrFeNi, (CoCrFeNi)₉₈Y₂, (CoCrFeNi)₉₆Y₄ HEAs were produced by vacuum arc melting and subsequent homogenization at 1150 °C for 24 h. The effect of Y addition on the structural, microstructural, and mechanical properties was investigated. The following conclusions could be drawn:

- The systematic addition of 2 at. and 4 at. % Y into CoCrFeNi HEA caused the dissolution of Y in the FCC crystal structure and the formation of CaCu5-type HS second phase.

- The increasing Y content from 2 at. % to 4 at. % resulted in the transformation of the microstructure from an elongated shape to nearly equiaxed grains.

- The EDS analyses revealed the segregation of the Ni and Y atoms into intergrain regions.

- The hardness of CoCrFeNi HEA was increased from 143 (±2) HV to 335 (±7) HV with the addition of 4 at. % Y.

- The compressive yield strength, fracture stress, and strain of 1025 MPa, 1538 MPa, and 16.5 %, respectively, were achieved with the addition of 4 at. % Y.

- The strength-ductility trade-off of CoCrFeNi HEA could be enhanced by the addition of Y for the potential engineering application.

ACKNOWLEDGEMENT

The authors would like to thank the Department of Metallurgical and Materials Engineering, Middle East Technical University for their support in the production of alloys.

CONFLICT OF INTEREST

The authors state that there is no conflict of interest.

AUTHOR CONTRIBUTION

Gokhan Polat: Methodology, Investigation, Data curation, Writing-review & editing.

Hasan Kotan: Data curation, Writing-review & editing.


References


1. Senkov ON, Miracle DB, Chaput KJ, Couzinie JP. Development and exploration of refractory high entropy alloys—A review. *Journal of Materials Research* 2018 33:19. 2018; 33: 3092–3128.
2. Zhang Y, Zuo TT, Tang Z, Gao MC, Dahmen KA, Liaw PK, Lu ZP. Microstructures and properties of high-entropy alloys. *Progress in Materials Science*. 2014; 61: 1–93.
3. Yeh JW, Chen SK, Lin SJ, Gan JY, Chin TS, Shun TT, Tsau CH, Chang SY. Nanostructured high-entropy alloys with multiple principal elements: Novel alloy design concepts and outcomes. *Advanced Engineering Materials*. 2004; 6: 299–303.
4. Guo S, Ng C, Lu J, Liu CT. Effect of valence electron concentration on stability of fcc or bcc phase in high entropy alloys. *Journal of Applied Physics*. 2011; 109: 103505.
5. Ye YF, Wang Q, Lu J, Liu CT, Yang Y. High-entropy alloy: challenges and prospects. *Materials Today*. 2016; 19: 349–362.
6. Gao MC, Zhang B, Guo SM, Qiao JW, Hawk JA. High-Entropy Alloys in Hexagonal Close-Packed Structure. *Metallurgical and Materials Transactions A: Physical Metallurgy and Materials Science*. 2016; 47: 3322–3332.
7. Gludovatz B, Hohenwarter A, Catoor D, Chang EH, George EP, Ritchie RO. A fracture-resistant high-entropy alloy for cryogenic applications. *Science*. 2014; 345: 1153–1158.
8. Liu J, Guo X, Lin Q, He Z, An X, Li L, Liaw PK, Liao X, Yu L, Lin J, Xie L, Ren J, Zhang Y. Excellent ductility and serration feature of metastable CoCrFeNi high-entropy alloy at extremely low temperatures. *Science China Materials*. 2019; 62: 853–863.
9. Liu WH, Lu ZP, He JY, Luan JH, Wang ZJ, Liu B, Liu Y, Chen MW, Liu CT. Ductile CoCrFeNiMox high entropy alloys strengthened by hard intermetallic phases. *Acta Materialia*. 2016; 116: 332–342.
10. Yang T, Zhao Y, Liu W, Kai J, Liu C. L12-strengthened high-entropy alloys for advanced structural applications. *Journal of Materials Research*. 2018; 33: 2983–2997.
11. Liu WH, Yang T, Liu CT. Precipitation hardening in CoCrFeNi-based high entropy alloys. *Materials Chemistry and Physics*. 2018; 210: 2–11.
12. Gao X, Chen R, Liu T, Fang H, Wang L, Su Y. High deformation ability induced by phase transformation through adjusting Cr content in Co-Fe-Ni-Cr high entropy alloys. *J Alloy Compd*. 2022; 895: 162564.
13. Garcia Filho FDC, Ritchie RO, Meyers MA, Monteiro SN. Cantor-derived medium-entropy alloys: bridging the gap between traditional metallic and high-entropy alloys. *Journal of Materials Research and Technology*. 2022; 17: 1868–1895.
14. He MY, Shen YF, Jia N, Liaw PK. C and N doping in high-entropy alloys: A pathway to achieve desired strength-ductility synergy. *Applied Materials Today*. 2021; 25: 101162.
15. Zeng Z, Xiang M, Zhang D, Shi J, Wang W, Tang X, Tang W, Wang Y, Ma X, Chen Z, Ma W, Morita K. Mechanical properties of Cantor alloys driven by additional elements: a review. *Journal of Materials Research and Technology*. 2021; 15: 1920–1934.
16. Tong C-J, Chen Y-L, Yeh J-W, Lin S-J, Chen S-K, Shun T-T, Tsau C-H, Chang S-Y. Mechanical Performance of the AlxCoCrCuFeNi High-Entropy Alloy System with Multiprincipal Elements. *Metallurgical and Materials Transactions A*. 2005; 36: 881–893.
17. Tekin M, Polat G, Kotan H. An investigation of abnormal grain growth in Zr doped CoCrFeNi HEAs through in-situ formed oxide phases. *Intermetallics*. 2022; 146: 107588.

18. Polat G, Tekin M, Kotan H. Role of yttrium addition and annealing temperature on thermal stability and hardness of nanocrystalline CoCrFeNi high entropy alloy. *Intermetallics*. 2022; 146: 107589.
19. Tekin M, Polat G, Kalay YE, Kotan H. Grain size stabilization of oxide dispersion strengthened CoCrFeNi-Y2O3 high entropy alloys synthesized by mechanical alloying. *Journal of Alloys and Compounds*. 2021; 887: 161363.
20. Zhu ZG, Ma KH, Wang Q, Shek CH. Compositional dependence of phase formation and mechanical properties in three CoCrFeNi-(Mn/Al/Cu) high entropy alloys. *Intermetallics*. 2016; 79: 1–11.
21. Polat G, Atalay Kalsen TS. Al içeriğinin (CoCrFe)60AlXNi(40-X) yüksek entropili alaşımının yapısal ve mekanik özellikleri üzerindeki etkisi. *Kahramanmaraş Sütçü İmam Üniversitesi Mühendislik Bilimleri Dergisi*. 2023; 26: 812–822.
22. Wang X, Zhang Z, Wang Z, Ren X. Microstructural Evolution and Tensile Properties of Al0.3CoCrFeNi High-Entropy Alloy Associated with B2 Precipitates. *Materials*. 2022; 15: 1215.
23. Chen X, Qin G, Gao X, Chen R, Song Q, Cui H. Strengthening CoCrFeNi High Entropy Alloy by In-Situ Phases of Laves and ZrC. *Metals and Materials International*. 2023; 29: 1390–1398.
24. Wang LM, Lin Q, Yue LJ, Liu L, Guo F, Wang FM. Study of application of rare earth elements in advanced low alloy steels. *Journal of Alloys and Compounds*. 2008; 451: 534–537.
25. Zhao Y, Wang J, Zhou S, Wang X. Effects of rare earth addition on microstructure and mechanical properties of a Fe–15Mn–1.5Al–0.6C TWIP steel. *Materials Science and Engineering: A*. 2014; 608: 106–113.
26. Zhang LJ, Zhang MD, Zhou Z, Fan JT, Cui P, Yu PF, Jing Q, Ma MZ, Liaw PK, Li G, Liu RP. Effects of rare-earth element, Y, additions on the microstructure and mechanical properties of CoCrFeNi high entropy alloy. *Materials Science and Engineering: A*. 2018; 725: 437–446.
27. Atas MS, Yildirim M. Structural properties and cyclic oxidation behavior of Ni-Al-Y superalloys. *Kovove Materialy*. 2022; 60: 281–292.
28. Yildirim M, Atas MS, Akdeniz MV, Mekhrabov AO. Effect of Y Addition on the Structural Properties and Oxidation Behavior of Fe60Al40-nYn Alloys (n= 1, 3, and 5 at.%). *Materials at High Temperatures*. 2022; 39: 220–230.
29. Cullty B., Stock SR. *Elements of X-Ray Diffraction: Third Edition*. New York: Prentice-Hall, 2014.
30. John R, Karati A, Garlapati MM, Vaidya M, Bhattacharya R, Fabijanic D, Murty BS. Influence of mechanically activated annealing on phase evolution in Al0.3CoCrFeNi high-entropy alloy. *Journal of Materials Science*. 2019; 54: 14588–14598.
31. Keleş A, Cengiz R, Yildirim M. Effect of Alloying Elements and Technological Parameters of Austempering on the Structure and Mechanical Properties of Ductile Cast Iron (ADI). *Metal Science and Heat Treatment*. 2023; 65: 191–199.
32. Polat G, Erdal ZA, Kalay YE. Design of Novel Non-equiatomic Cu-Ni-Al-Ti Composite Medium-Entropy Alloys. *Journal of Materials Engineering and Performance*. 2020; 29: 2898–2908.
33. Moghanni H, Dehghani K, Shafiei A. Effects of process parameters on microstructure and mechanical properties of Al0.5CoCrFeNi high entropy alloy thin sheets using pinless friction stir welding. *Journal of Materials Research and Technology*. 2022; 16: 1069–1089.
34. Zhou YX, Hu MY, Yan P, Shi X, Chong XY, Feng J. A first-principles calculation of structural, mechanical, thermodynamic and electronic properties of binary Ni-Y compounds. *RSC Advances*. 2018; 8: 41575–41586.
35. Beaudry B, Daane A. Yttrium-nickel system. *Trans Met Soc AIME*. 1960.
36. Xu XD, Guo S, Nieh TG, Liu CT, Hirata A, Chen MW. Effects of mixing enthalpy and cooling rate on phase formation of AlxCoCrCuFeNi high-entropy alloys. *Materialia*. 2019; 6: 100292.
37. Kukshal V, Patnaik A, Bhat IK. Effect of cobalt on microstructure and properties of AlCr1.5CuFeNi2Cox high-entropy alloys. *Materials Research Express*. 2018; 5: 046514.
38. Takeuchi A, Inoue A. Classification of Bulk Metallic Glasses by Atomic Size Difference, Heat of Mixing and Period of Constituent Elements and Its Application to Characterization of the Main Alloying Element. *Materials Transactions*. 2005; 46: 2817–2829.
39. Oliveira PHF, Mancilha PHS, Reyes RAV, de Gouveia GL, Bolfarini C, Spinelli JE, Coury FG. Influence of the cooling rate on the solidification path and microstructure of a AlCoCrFeNi2.1 alloy. *Materials Characterization*. 2023; 203: 113121.
40. Hong X, Hsueh CH. Effects of yttrium addition on microstructures and mechanical properties of CoCrNi medium entropy alloy. *Intermetallics*. 2022; 140: 107405.
41. Silveira RMS Da, Guimarães AV, De Melo CH, Ribeiro RM, Farina AB, Malet L, De Almeida LH, Araujo LS. Effect of yttrium addition on phase transformations in alloy 718. *Journal of Materials Research and Technology*. 2022; 18: 3283–3290.
42. Stepanov ND, Yurchenko NY, Tikhonovsky MA, Salishchev GA. Effect of carbon content and annealing on structure and hardness of the CoCrFeNiMn-based high entropy alloys. *Journal of Alloys and Compounds*. 2016; 687: 59–71.
43. Fleischer RL. Substitutional solution hardening. *Acta Metallurgica*. 1963; 11: 203–209.
44. Lin CM, Tsai HL. Evolution of microstructure, hardness, and corrosion properties of high-entropy Al0.5CoCrFeNi alloy. *Intermetallics*. 2011; 19: 288–294.
45. Lokman M, Ab A. Enhanced lattice distortion, yield strength, critical resolved shear stress, and improving mechanical properties of transition-metals doped CrCoNi medium entropy alloy. *RSC Advances*. 2021; 11: 23719–23724.
46. Zhang J, Chen S, Liu J, Qing Z, Wu Y. Microstructure and Mechanical Properties of Novel High-Strength, Low-Activation Wx(TaVZr)100-x (x = 5, 10, 15, 20, 25) Refractory High Entropy Alloys. *Entropy* 2022, Vol 24, Page 1342. 2022; 24: 1342.
47. Seifi M, Li D, Yong Z, Liaw PK, Lewandowski JJ. Fracture Toughness and Fatigue Crack Growth Behavior of As-Cast High-Entropy Alloys. *Jom*. 2015; 67: 2288–2295.

A Research: Investigation of Financial Applications with Blockchain Technology

Mohammed Ali Mohammed¹  Fuat Turk^{2*} 

¹  Cankiri Karatekin University, Faculty of Engineering, Department of Computer Engineering, Cankiri, Türkiye.

²  Kirikkale University, Faculty of Engineering and Architecture, Kirikkale, Türkiye.

ABSTRACT

Cryptocurrencies have revolutionized the financial landscape by providing decentralized and anonymous payment systems, making them an intriguing subject for investors and researchers. This article delves into applying machine learning techniques for predicting cryptocurrency prices, mainly focusing on Bitcoin, Ethereum, and Binance Coin. Employing a range of machine learning models, including XGBoost, Linear Regression, and Gaussian Processes, the study aims to evaluate their predictive performance comprehensively. The results are promising; our models outperform existing studies, achieving impressively low RMSE values of 0.0040 for Bitcoin, 0.028 for Ethereum, and 0.027 for Binance Coin. These findings contribute valuable insights into the volatility and dynamics of cryptocurrency prices and underscore the potential of machine learning in shaping financial decision-making. Future directions include integrating advanced deep learning models, additional data sources, and ensemble methods to enhance prediction accuracy and robustness.

Keywords:

Cryptocurrencies; Machine learning; Price prediction; Bitcoin; Ethereum; Binance coin

Article History:

Received: 2023/09/25

Accepted: 2024/03/23

Online: 2024/03/31

Correspondence to: Fuat TÜRK

E-mail: fturk@kku.edu.tr;

Phone: +905057061373

This article has been checked for similarity.



This is an open access article under the CC-BY-NC licence

<http://creativecommons.org/licenses/by-nc/4.0/>

INTRODUCTION

Over the last ten years, the swift rise of cryptocurrencies has triggered sweeping shifts in the worldwide economy, reshaping financial landscapes and remoulding transactional systems [1]. These seismic shifts owe much to rapid advancements in Information Technology (IT), enabling the emergence of blockchain and the birth of Bitcoin in 2009 by the enigmatic entity known as Satoshi Nakamoto [2]. The soaring popularity of digital currencies like Bitcoin and Ethereum is fuelled by an expanding community of users and the allure of substantial financial returns. These currencies use a decentralized architecture anchored by blockchain technology for the secure verification and logging of transactions. However, this decentralization poses complex challenges for regulatory bodies and traditional financial institutions [3].

As fascination with cryptocurrencies grows, so does academic interest in blockchain and its foundational technology. Digital currencies come into the blockchain each time a new block is formed, and they can be traded for various goods and services [4]. Mainstream cryptocurrencies like Bitcoin and Ethereum have attained widespread acknowledgement, notably for their hefty trading volumes and market capitalizations. For

instance, in April 2021, Bitcoin displayed a market value of USDT 1,304 billion alongside a trading volume of USDT 64 billion. Ethereum posted a USDT 38 billion trading volume and a USDT 265 billion market cap [5]. This burgeoning value and interest have led researchers to dig deeper into the predictive analysis of cryptocurrencies to understand market trends and minimize investor risks.

While there are intrinsic challenges, recent years have seen remarkable progress in machine learning (ML) and blockchain technologies [6]. These technological leaps have culminated in new or enhanced products now used by billions worldwide. Numerous studies have honed in on applying these innovative technologies to financial markets, exploring areas like stock market prediction and fraud detection since ML research took off [7]. The insights from such research are especially crucial for cryptocurrencies, which are increasingly considered financial assets by a growing audience.

Blockchain and ML are relatively nascent, marked by a limited research corpus. Most existing studies in this domain have mainly concentrated on the non-technical facets of blockchain. Nonetheless, there lies

Cite as:

Mohammed MA, Turk F. A Research: Investigation of Financial Applications with Blockchain Technology. Hittite Journal of Science and Engineering 2024;11(1):33-40. doi:10.17350/hjse19030000329

a vast, untapped reservoir of research potential due to the frontier nature of blockchain and the rapid advancements in ML. In this thesis, we aim to delve into the complex interplay between cryptocurrencies, blockchain, and ML, examining their interconnected challenges and untangling the prospects for future innovations. The primary objective of this article is to enhance the understanding of cryptocurrency price movements by employing various ML techniques. Through a detailed analysis focusing on the daily closing prices of three significant cryptocurrencies, we aim to develop predictive models that can accurately forecast the next day's closing price. The research seeks to identify the most influential computational methods for predicting cryptocurrency prices by comparing a range of ML algorithms and their performance metrics. Ultimately, this study aims to contribute to both academic literature and practical applications by highlighting the potential of ML and blockchain technologies in influencing and transforming financial decision-making processes.

In recent years, many studies have been undertaken to scrutinize different facets of cryptocurrency, most notably Bitcoin, by applying ML and deep learning (DL) methodologies. [8] employed a Stochastic Fluid Queueing Process to mathematically model Bitcoin transaction times, particularly in high-traffic scenarios, thereby shedding light on the probability distribution of confirmation times. Their work added crucial insights into understanding transaction times in congested network conditions. [9], on the other hand, it utilized Support Vector Machines (SVM) on time-series cryptocurrency data to compare the performance of ML systems in Bitcoin price forecasting. Their research concluded that there is significant scope for enhancing model accuracy, as evidenced by an accuracy rate of 95.50%.

Building upon similar themes, [10] proposed using generic machine learning algorithms to compare performance systems for Bitcoin forecasting, focusing on time series data but not quantifying the results regarding Root Mean Squared Error (RMSE). [11] devised an innovative approach using Random Forest (RF) Regressor, Multilayer Perceptron (MLP), and statistical regression models to predict the time needed for a mining node to validate and confirm a transaction. Their comparison indicated that the RF Regressor had an RMSE of 0.36, outperforming MLP and a previously introduced statistical model.

[12] tackled Bitcoin's notorious price volatility by employing DL models like Long Short-Term Memory (LSTM) and Gated Recurrent Units (GRU). They achieved a notable level of precision in predicting Bitcoin's price movements, with RMSE values of 0.045 and 0.051 for LSTM and GRU, respectively. Similarly, [13] engaged multiple machine learning techniques like SVM, Artificial Neural Networks

(ANN), Naive Bayes (NB), RF, and Logistic Regression (LR) to forecast Bitcoin prices. Their results underscored that ANN, with an RMSE of 0.341, performed relatively better under certain conditions.

Researchers in [14] used ML to study the distribution of Bitcoin transaction times based on memory pool size, discovering an inverse Gaussian distribution. Tanwar et al. presented a hybrid deep learning model that combines LSTM and GRU to forecast Litecoin and Zcash prices, achieving an MAE of 0.02038 and 0.02103, respectively. In a parallel line of inquiry, [5] used ANN and SVM to study the relationship between Ethereum prices and blockchain data, finding ANN to be the superior model with an RMSE of 0.068. In [15], Ho et al. used LSTM and Linear Regression (LR) models to predict Bitcoin values, impressively achieving an accuracy rate of 99.87%.

Furthermore, [16] introduced novel on-chain metrics and developed a deep learning model for Bitcoin, reporting an RMSE of 0.045 for LSTM and 0.293 for Random Forest. Finally, in the most recent study [17] by Aziz et al. (2022), a Light Gradient Boosting Machine (LGBM) was used to identify fraudulent Ethereum transactions. Although they didn't provide RMSE values, they claimed that the LGBM model outperformed other machine learning and soft computing models like RF, MLP, and XGBoost.

These studies highlight the burgeoning potential of machine learning and deep learning techniques in various aspects of cryptocurrency, such as transaction time analysis, security vulnerability identification, and price prediction, thereby laying the groundwork for developing automated trading systems.

MATERIAL AND METHODS

Proposed model

Our proposed framework is a multi-faceted machine-learning model tailored for cryptocurrency price prediction. Utilizing three curated datasets, the model undergoes an initial data preprocessing phase where normalization ensures compatibility across various ML algorithms. This step streamlines the data and optimizes computational efficiency. Subsequently, a diverse suite of algorithms, including LSTM, CNN, KNN, XGBoost, Astro ML, and several regression techniques, are applied to construct the predictive model, as shown in Fig. 1. Aimed at providing reliable and precise price forecasts, our model equips traders, investors, and other market participants with actionable insights, offering a scalable and flexible tool responsive to the ever-changing cryptocurrency landscape.

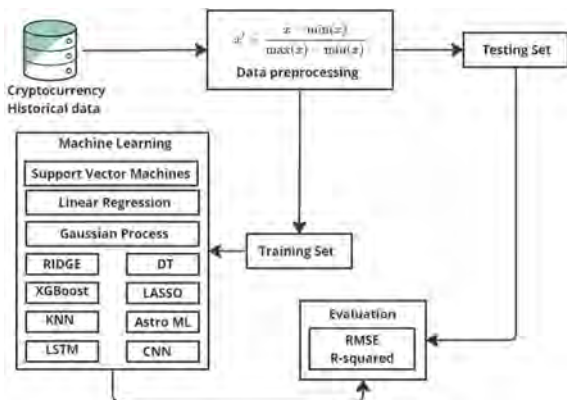


Figure 1. Cryptocurrency proposed model.

Our research utilizes a dataset comprising the historical prices and trading volumes of four cryptocurrencies: Bitcoin (BTC), Ethereum (ETH), Binance Coin (BNB), and Tether (USDT). This dataset spans from November 9, 2017, to August 27, 2022, and includes data points collected for each cryptocurrency in terms of their adjusted closing prices and trading volumes. The datasets were sourced from Kaggle and processed using Python's Pandas library. Conversion to a data frame structure allows for robust data handling and efficient computational operations. We extracted this dataset for our analysis, focusing particularly on BTC, ETH, and BNB, due to their significant impact on the cryptocurrency market dynamics. This valuable dataset, uploaded to Kaggle two years ago, encompasses detailed records of each cryptocurrency's adjusted closing prices and trading volumes, enabling an in-depth analysis of market trends. Notably, this dataset has also been utilized in a study by Baviskar, V. S., Radha, D., & Sankari, S. U. in their 2023 publication on cryptocurrency price prediction and analysis, presented at the 14th International Conference on Computing Communication and Networking Technologies (ICCCNT) [29].

Our dataset includes seven critical features to facilitate a comprehensive market analysis:

1. **Date:** This column records the specific date for each data entry, formatted to capture the day, month, and year. It serves as the temporal reference for all other data points, providing the context in which the price and volume observations were made.
2. **Close (BTC):** This column contains the adjusted closing price of Bitcoin (BTC) on each respective date, expressed in USD. The adjusted close price reflects the final trading price of Bitcoin for the day and is adjusted for any corporate actions that might affect the price, such as stock splits.
3. **Volume (BTC):** This column reports the total trading volume of Bitcoin transactions on the corresponding date. It measures the number of Bitcoins that were traded during the day, offering insights into the trading activity and

liquidity of Bitcoin in the market.

4. **Close (ETH):** Similar to the BTC close column, this column provides the adjusted closing price of Ethereum (ETH) for each date, in USD. It represents the final price at which Ethereum was traded at the end of the trading day, after adjustments for any applicable market events.

5. **Volume (ETH):** This column indicates the daily trading volume of Ethereum, capturing the total quantity of Ethereum traded on each day. The volume data helps assess Ethereum's market activity and investor interest over time.

6. **Close (BNB):** This column records the adjusted closing price of Binance Coin (BNB) on each date, expressed in USD. The price reflects the final market valuation of Binance Coin at the end of each trading day, adjusted for any significant events affecting stock prices.

7. **Volume (BNB):** Finally, this column measures the daily trading volume of Binance Coin, indicating the total amount of BNB traded on each date. It provides a gauge of Binance Coin's market activity and liquidity.

Data Preprocessing

Data preprocessing forms the backbone of our study, focusing on cleaning and transforming raw data to ensure its compatibility with machine learning algorithms. We deal with missing values and outliers during the data cleaning and employ Pandas' Dropna function to refine the dataset.

After cleaning, we retain only essential features like 'date' and 'close' to maintain data integrity. On the transformation front, we tackle feature scaling issues through Min/Max normalization. This approach harmonizes variable scales, enhancing the predictive accuracy of our machine-learning models in cryptocurrency price forecasting. Both data cleaning and transformation steps are instrumental in fortifying our dataset's quality and our predictive model's robustness.

Predictive Methods

In our study, we allocated 70% of the dataset for training and 30% for testing, adhering to a widely accepted practice in machine learning to balance robust training and unbiased evaluation. We employed eleven distinct predictive models, each tailor-made for a specific cryptocurrency. We used identical model parameters across the various cryptocurrencies to maintain consistency in our comparisons. Detailed analyses of each model will follow in subsequent sections of the article.

Long Short-Term Memory (LSTM) Model

In cryptocurrency price prediction, LSTM networks [18] have garnered attention for their capability to model time series data effectively. These networks can capture long-term dependencies in historical price data and other

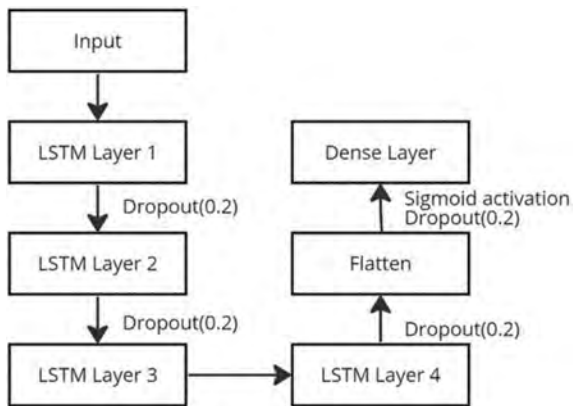


Figure 2. Our LSTM architecture.

market variables like trading volume and trends. After training on this historical data, LSTMs can generate future price predictions with considerable accuracy. Their performance is competitive compared to other predictive models, making them a popular choice for this application. Specific architecture and training steps for LSTM models in cryptocurrency prediction are detailed in Fig. 2.

Convolutional Neural Network Model

CNNs [19] are increasingly used for cryptocurrency price prediction, offering valuable insights into market trends and trading opportunities. Designed to excel at handling image and time-series data, CNNs are particularly apt for analyzing complex cryptocurrency data structures. A typical CNN architecture for this use case consists of multiple layers: An input layer that accepts preprocessed historical price data, convolutional layers that identify patterns and features, pooling layers that simplify the model's complexity, and fully connected layers that finally make price predictions. The output layer then delivers these predicted future cryptocurrency prices. This structured approach makes CNNs a reliable tool for making informed cryptocurrency trading decisions.

Support Vector Regression (SVR) Model

The SVR model [20] uses historical price data to forecast future cryptocurrency prices. Through mathematical optimization, SVR identifies an optimal function that minimizes error between actual and predicted values. The data is transformed into a high-dimensional feature space, where a hyperplane represents the prediction function. The goal is to find a hyperplane that minimizes errors and maximizes the margin between itself and the nearest data points, enhancing the model's robustness and preventing overfitting. Once established, this prediction function can forecast future cryptocurrency prices by projecting new data points into this high-dimensional space.

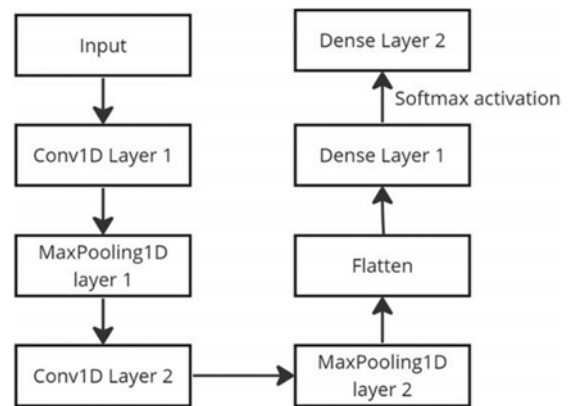


Figure 3. Our CNN architecture

K-Nearest Neighbors (KNN) Model

The KNN model [21] predicts future cryptocurrency prices by storing historical data points and their target values. When a new data point emerges, the model identifies its K nearest neighbours from the stored data based on a selected distance metric. The forecast is then calculated as the average of these neighbours' target values. While KNN is a quick and straightforward algorithm, its accuracy depends on the careful choice of distance metric and the number of neighbours. Additionally, KNN may struggle with high-dimensional data, as the distance metrics might not effectively capture relationships between data points.

XGBoost Model

XGBoost [22] operates by combining the forecasts of multiple weak decision tree (DT) optimized using gradient descent. The process starts by initializing residuals representing the differences between actual target values and current predictions. Trees are built by iteratively finding the split that minimizes loss, subject to stopping criteria like maximum tree depth or minimum samples per node. Tree pruning further refines the model by eliminating less essential branches. Through a boosting technique, the model iteratively adds trees and updates the forecast based on these residuals. Each tree's accuracy contributes to its weighting, and the final prediction is an aggregated, weighted sum of all trees. This boosting approach allows XGBoost to correct individual tree biases and produce more accurate predictions.

AstroML Model

AstroML [23], initially designed for machine learning applications in astrophysics, offers valuable tools for cryptocurrency analysis. AstroML's regression capabilities within the crypto landscape can model the correlation between multiple variables and coin price. The optimal regression model depends on factors like data complexity and the desired level of accuracy. Methods such as line-

ar regression, polynomial regression, DT, and RF can be deployed to forecast cryptocurrency prices based on historical data and other influencing factors.

Lasso Model

Lasso [24] is a machine learning approach often employed in cryptocurrency price prediction to enhance model interpretability and accuracy. It distinguishes itself by incorporating a penalty term into the loss function minimized during optimization. This term pushes the model towards sparsity in its coefficients, effectively downplaying less essential features. Consequently, Lasso often yields simpler, more interpretable models by focusing on a subset of relevant features for its predictions.

Ridge Model

Ridge Regression [25] is a regularization method commonly employed for predicting cryptocurrency prices to bolster the model's stability and interpretability. During optimization, ridge Regression nudges the model towards smaller coefficients across all features by introducing a penalty term to the loss function. This diminishes the model's sensitivity to minor data fluctuations, resulting in a more stable and robust predictive framework.

Linear Regression Model

Linear regression [26] is a foundational statistical method to model the relationship between a dependent variable and one or more independent variables. In the context of cryptocurrency, LR uses historical data to map the connection between various features and the cryptocurrency's price. It operates on the principle that these relationships can be linearly represented. The model aims to optimize coefficients for each feature to minimize the difference between predicted and actual values. Optimization techniques like gradient descent and ordinary least squares are commonly employed. Once the coefficients are optimized, the LR model can forecast future cryptocurrency prices through a weighted sum of the independent variables.

DT Model

DT [27] refers to machine learning algorithms that provide a structured, tree-like approach to decision-making by considering various possible outcomes and the factors influencing them. The tree starts from a root node, branching into different scenarios, each leading to subsequent child nodes and relevant probabilities. This allows for hierarchical mapping.

RESULTS AND DISCUSSION

Evaluation Models

We employ key performance metrics, RMSE and R-squared (R^2), to evaluate our model's effectiveness for

forecasting cryptocurrency prices. A lower RMSE score and a higher R^2 value indicate superior predictive performance, providing a comparative measure to gauge the accuracy of the various predictors.

Evaluation metrics with Bitcoin dataset

In our study, we evaluated the performance of various machine learning methods for predicting Bitcoin prices using two key metrics: RMSE and R^2 . As presented in Table 1, different models yield distinct results. The LR and GP models outperformed other techniques, achieving the lowest RMSE values of 0.022368 and 0.022381, respectively, and high R^2 values exceeding 0.98. These results suggest exceptional predictive accuracy. The Ridge model also exhibited strong performance, with an R^2 value of 0.980667.

On the other hand, the CNN model had the highest RMSE of 0.166565 and the lowest R^2 value of 0.308789, indicating suboptimal performance for this dataset. The XGB Regressor model demonstrated an impressively low RMSE of 0.004042, but its R^2 value was slightly lower than that of the Ridge and LR models. The ASTRO ML model, adapted from astrophysics, also performed well with an RMSE of 0.063575 and an R^2 value of 0.899303. These evaluations provide valuable insights into the most suitable ML methods for accurate and reliable Bitcoin price prediction, with LR and GP emerging as the leading candidates.

Table 1. Performance metrics of various models for Bitcoin dataset

Model Name	RMSE	R^2
LSTM	0.088911	0.803051
CNN	0.166565	0.308789
SVR	0.066702	0.889154
KNN	0.085906	0.816138
XGBRegressor	0.004042	0.899303
ASTRO ML	0.063575	0.899303
Ridge	0.027857	0.980667
LR	0.022368	0.987535
DT	0.074230	0.862722
GP	0.022381	0.987520

Evaluation metrics with Ethereum dataset

Our study includes an in-depth performance evaluation of multiple machine learning algorithms for predicting Ethereum prices, focusing on RMSE and R^2 . As depicted in Table 2, the results vary significantly among different models. The LR and GP models showcase the lowest RMSE values of 0.028457 and 0.028346, respectively, while achieving exceptionally high R^2 values, just above 0.98. This suggests that these models provide remarkably accurate and reliable predictions for Ethereum prices. The Ridge model also performed notably well, with an R^2 value of 0.956592.

Table 2. Performance metrics of various models for the Ethereum dataset

Model Name	RMSE	R ²
LSTM	0.144385	0.525188
CNN	0.208044	0.014207
SVR	0.191266	0.166793
KNN	0.100407	0.770383
XGBRegressor	0.124654	0.646093
ASTRO ML	0.161861	0.403296
Ridge	0.043656	0.956592
LR	0.028457	0.981556
DT	0.129323	0.619086
GP	0.028346	0.981700

On the contrary, the CNN model yielded the highest RMSE of 0.208044 and a deficient R² value of 0.014207, indicating its poor suitability for this particular task. Among ensemble models, the XGBRegressor exhibited a relatively low RMSE of 0.124654, although its R² was somewhat less impressive than the Ridge and LR models. Interestingly, the ASTRO ML model, adapted from astrophysics, had an RMSE of 0.161861 and an R² of 0.403296, placing it in the middle range of performance. The analysis reveals that LR and GP models are the most effective for predicting Ethereum prices regarding RMSE and R².

Evaluation metrics with Binance Coin dataset

Our analysis rigorously evaluates the performance of different ML algorithms for forecasting Binance Coin prices, emphasizing RMSE and R². As shown in Table 3, the metrics exhibit considerable variation across models. The LSTM and CNN models yielded unusually high R² values above R² and the highest RMSE of 0.265808, suggesting potential overfitting or other anomalies in their predictive performance. In stark contrast, the LR and GP models outperformed others with the lowest RMSE values, 0.027286 and 0.027298, respectively, and R² values around 0.968. This indicates exceptional accuracy and reliability for these methods in predicting Binance Coin prices. The Ridge model also showed high reliability with an R² of 0.924290, albeit with a slightly higher RMSE of 0.041881.

Interestingly, SVR and DT models presented moderate R² values of 0.636128 and 0.350212, respectively, but could

Table 3. Performance metrics of various models for the Binance Coin dataset

Model Name	RMSE	R ²
LSTM	0.265808	2.049658
CNN	0.265808	2.049658
SVR	0.091816	0.636128
KNN	0.136745	0.192878
XGBRegressor	0.142542	0.122999
ASTRO ML	0.128486	0.287434
Ridge	0.041881	0.924290
LR	0.027286	0.967863
DT	0.176865	0.350212
GP	0.027298	0.967835

not match the top-performing models in terms of RMSE. The ensemble model XGBRegressor exhibited minor effectiveness with an R² of 0.122999, raising questions about its suitability for this task. The data suggests that for Binance Coin price prediction, LR and GP models are the most reliable in terms of both RMSE and R².

Comparison Results

In an endeavour to place our contributions within the broader scope of research in cryptocurrency price prediction, we present a comparative evaluation in Table 4. Our model significantly outperforms existing models across multiple cryptocurrencies in terms of RMSE. For Bitcoin, the XGBoost model generated an impressively low RMSE of 0.0040, which is considerably smaller than the values reported by Pabuc et al. (2020) for ANN, SVR, Naive Bayes, and RF, which ranged from 0.293 to 0.461. Similarly, our XGBoost model outshines the LSTM model by Jagannath et al. (2021), which recorded an RMSE as high as 1.9. In the Ethereum context, our LR and GP models delivered an RMSE of 0.028, again establishing superior performance when compared to the ANN and SVR models by Kim et al. (2021) that reported RMSEs of 0.068 and 0.048, respectively. Lastly, for Binance Coin, our LR and GP models achieved an RMSE of 0.027, though a direct comparison with previous works is not available for this specific cryptocurrency. These results corroborate our models' robustness and superior predictive accuracy, offering significant improvements over existing methods in the literature.

Table 4. Comparison of RMSE values for various models and cryptocurrencies

AUTHORS	CRYPTOCURRENCY	TECHNIQUES	RMSE
Pabuc et al. (2023)	Bitcoin	ANN	0.341
Pabuc et al. (2023)	Bitcoin	SVR	0.438
Pabuc et al. (2023)	Bitcoin	Naive Bayes	0.461
Pabuc et al. (2023)	Bitcoin	RF	0.293
Jagannath et al. (2021)	Bitcoin	LSTM	1.9
Kim et al. (2021)	Ethereum	ANN	0.068
Kim et al. (2021)	Ethereum	SVR	0.048
Our model	Bitcoin	XGBoost	0.0040
Our model	Ethereum	LR, GP	0.028
Our model	Binance coin	LR, GP	0.027

CONCLUSION

This study ventured into the burgeoning field of ML and blockchain to predict cryptocurrency prices. These models were selected for their ability to handle the complex and nonlinear nature of cryptocurrency price movements, leading to our achieving remarkably low RMSE values of 0.0040 for Bitcoin, 0.028 for Ethereum, and 0.027 for Binance Coin. This performance significantly surpasses that of previous studies, such as those by Pabuc et al. (2023) and Kim et al. (2021), where the best RMSE

values reported for Bitcoin and Ethereum were 0.293 and 0.048, respectively. Our models' superior accuracy can be attributed to the sophisticated data handling and learning capabilities of XGBoost, along with the robustness of LR and GP in capturing the underlying trends and volatility of cryptocurrency markets. These compelling results substantiate the potential of ML techniques in innovating and informing decision-making in the financial sector. In future work, we suggest exploring advanced deep-learning models for sentiment analysis and integrating additional data sources to refine prediction accuracy. Ensemble learning and model interpretability also offer promising avenues for further research.

CONFLICT OF INTEREST

Authors approve that to the best of their knowledge, there is not any conflict of interest or common interest with an institution/organization or a person that may affect the review process of the paper.

AUTHOR CONTRIBUTION

Mohammed Ali Mohammed: Conceptualization, Methodology, Software, Validation, Writing- original draft
Fuat Turk: Data curation, Visualization, Investigation, Writing- review and editing

REFERENCES

- Marc Pilkington. 11 Blockchain technology: principles and applications. Research handbook on digital transformations, 225(2016), 2016.
- Pinyaphat Tasatanattakool and Chian Techapanupreeda. Blockchain: Challenges and applications. In 2018 International Conference on Information Networking (ICOIN), pages 473–475. IEEE, 2018.
- Thippa Reddy Gadekallu, Thien Huynh-The, Weizheng Wang, Gokul Yenduri, Pasika Ranaweera, Quoc-Viet Pham, Daniel Benevides da Costa, and Madhusanka Liyanage. Blockchain for the metaverse: A review. arXiv preprint arXiv:2203.09738, 2022.
- Saveen A Abeyratne and Radmehr P Monfared. Blockchain-ready manufacturing supply chain using distributed ledger. International journal of research in engineering and technology, 5(9):1–10, 2016.
- Han-Min Kim, Gee-Woo Bock, and Gunwoong Lee. Predicting ethereum prices with machine learning based on blockchain information. Expert Systems with Applications, 184:115480, 2021.
- Evangeline Ducas and Alex Wilner. The security and financial implications of blockchain technologies: Regulating emerging technologies in canada. International Journal, 72(4):538–562, 2017.
- Peter Gomber, Robert J Kauffman, Chris Parker, and Bruce W Weber. On the fintech revolution: Interpreting the forces of innovation, disruption, and transformation in financial services. Journal of management information systems, 35(1):220–265, 2018.
- David Koops. Predicting the confirmation time of bitcoin transactions. arXiv preprint arXiv:1809.10596, 2018.
- Azizah Hitam and Amelia Ritahani Ismail. Comparative performance of machine learning algorithms for cryptocurrency forecasting. Ind. J. Electr. Eng. Comput. Sci, 11(3):1121–1128, 2018.
- S Yogeshwaran, Maninder Jeet Kaur, and Piyush Maheshwari. Project based learning: predicting bitcoin prices using deep learning. In 2019 IEEE global engineering education conference (EDUCON), pages 1449–1454. IEEE, 2019.
- Harsh Jot Singh and Abdelhakim Senhaji Hafid. Transaction confirmation time prediction in ethereum blockchain using machine learning. arXiv preprint arXiv:1911.11592, 2019.
- Temesgen Awoke, Minakhi Rout, Lipika Mohanty, and Suresh Chandra Satapathy. Bitcoin price prediction and analysis using deep learning models. In Communication Software and Networks: Proceedings of INDIA 2019, pages 631–640. Springer, 2020.
- Hakan Pabuc, Serdar Ongan, and Ayse Ongan. Forecasting the movements of bitcoin prices: an application of machine learning algorithms. arXiv preprint arXiv:2303.04642, 2023.
- Rowel Gundlach, Martijn Gijsbers, David Koops, and Jacques Resing. Predicting confirmation times of bitcoin transactions. ACM SIGMETRICS Performance Evaluation Review, 48(4):16–19, 2021.
- Alvin Ho, Ramesh Vatambeti, and Sathish Kumar Ravichandran. Bitcoin price prediction using machine learning and artificial neural network model. Indian Journal of Science and Technology, 14(27):2300–2308, 2021.
- Nishant Jagannath, Tudor Barbulescu, Karam M Sallam, Ibrahim Elgendi, Asuquo A Okon, Braden McGrath, Abbas Jamalipour, and Kumudu Munasinghe. A self-adaptive deep learning-based algorithm for predictive analysis of bitcoin price. IEEE Access, 9:34054–34066, 2021.
- Rabia Musheer Aziz, Mohammed Farhan Baluch, Sarthak Patel, and Abdul Hamid Ganie. Lgbm: a machine learning approach for ethereum fraud detection. International Journal of Information Technology, 14(7):3321–3331, 2022.
- Alex Graves and Alex Graves. Long short-term memory. Supervised sequence labelling with recurrent neural networks, pages 37–45, 2012.
- Jiuxiang Gu, Zhenhua Wang, Jason Kuen, Lianyang Ma, Amir Shahroudy, Bing Shuai, Ting Liu, Xingxing Wang, Gang Wang, Jianfei Cai, et al. Recent advances in convolutional neural networks. Pattern recognition, 77:354–377, 2018.
- Alex J Smola and Bernhard Schölkopf. A tutorial on support vector regression. Statistics and computing, 14:199–222, 2004.
- Padraig Cunningham and Sarah Jane Delany. k-nearest neighbour classifiers—a tutorial. ACM computing surveys (CSUR), 54(6):1–25, 2021.
- Syeda Sarah Azmi and Shwetha Baliga. An overview of boosting decision tree algorithms utilizing adaboost and xgboost boosting strategies. Int. Res. J. Eng. Technol, 7(5), 2020.
- Snigdha Sen, Sonali Agarwal, Pavan Chakraborty, and Krishna Pratap Singh. Astronomical big data processing using machine learning: A comprehensive review. Experimental Astronomy, 53(1):1–43, 2022.
- Lukas Meier, Sara Van De Geer, and Peter Bühlmann. The group lasso for logistic regression. Journal of the Royal Statistical Society Series B: Statistical Methodology, 70(1):53–71, 2008.
- Arthur E Hoerl and Robert W Kennard. Ridge regression: applications to nonorthogonal problems. Technometrics, 12(1):69–82, 1970.
- Sanford Weisberg. Applied linear regression, volume 528. John

Wiley & Sons, 2005.

27. Sotiris B Kotsiantis. Decision trees: a recent overview. *Artificial Intelligence Review*, 39:261–283, 2013.
28. Christopher Williams and Carl Rasmussen. Gaussian processes for regression. *Advances in neural information processing systems*, 8, 1995.
29. Baviskar, V. S., Radha, D., & Sankari, S. U.. Cryptocurrency Price Prediction and Analysis. In *2023 14th International Conference on Computing Communication and Networking Technologies (ICCCNT)* (pp. 1-7). July,2023.

Size Dependent Compressive Strength of FIB Machined Single Crystal Manganese Pillars

Halil Yılmaz^{1*}  Bulent Alkan²  Hasan Feyzi Budak³ 

¹ Mus Alparslan University, Department of Mechanical and Metal Technologies, Mus, Türkiye.

² Hittit University, Department of Metallurgy and Materials Engineering, Corum, Türkiye.

³ Ataturk University, East Anatolia High Technology Application and Research Center, Erzurum, Türkiye.

ABSTRACT

The deformation behavior of single crystals of manganese pillars generated by focused ion beam (FIB), with diameters ranging from $-1 \mu\text{m}$ to $-4.5 \mu\text{m}$, has been studied as a function of specimen size using micropillar compression at ambient temperature. The manganese pillars were machined from randomly chosen larger grains of polycrystalline metal. At ambient temperature, single crystals of manganese display chaotic slip planes emerging on the sample surface and brittle plastic deformation when the sample size is decreased to the micrometer scale. The manganese pillars reached very high flow stresses in the range of 4-5.6 GPa. The stress-strain curves of all tested manganese pillars demonstrated significant work hardening and smooth flow behavior, with strains up to 8-10%. After 10% strain, however, the flow stresses remained constant with no work hardening. As previously reported, the manganese pillars with undetermined crystal orientation demonstrated a less pronounced size effect (-0.14) by the size effect exponent of BCC pillars.

Keywords:

Focused ion beam; Manganese; Micropillar compression; Mechanical properties; Size effect

INTRODUCTION

Pure manganese is simply known as 'hard, brittle and silverly colored' metal, however why manganese is hard and is not entirely clear. The microcracks appearing during the phase transformation upon solidification are sometimes reported as one of the main causes of brittleness, since the varying displacements are accumulating during the multiphase transformation (1, 2).

Manganese resembles iron and is reasonably reactive that dissolves non-oxidizing acids. Additionally, it tends to rust when subjected to exposure to water. It has been widely used as the main additive in the production of steel and other alloys, thereby significantly enhancing their physical and mechanical properties. Manganese is important as an alloying element in ferrous and non-ferrous metal alloys to enhance corrosion resistance and strength. Furthermore, manganese dioxide is commonly employed as a cathode material in commercial batteries. (3, 4).

It is known that manganese undergoes isotropic phase transformation on cooling, beginning from δ to γ (at 1407 K), then to β (at 1368 K) and finally to α (at 1015

K). While δ to γ phases have body centered cubic (BCC) and face centered cubic (FCC) respectively. The β and α phases of manganese are known to have a complicated crystal structure with 20 and 58 atoms in the cubic cell, respectively. α -manganese has a complex crystal lattice of the A12-type based on the BCC structure with a lattice constant $\alpha \sim 8.9 \text{ \AA}$ (2, 5).

The use of advanced characterization techniques is one component in knowing the quality of such alloys or steels. However, evaluating small-volume materials differs from testing bulk materials. This is due to the occurrence of artifacts, such as in nanomechanical testing techniques. Mechanical properties and deformation behavior of small volume materials are critical in the effective design of small devices that must sustain stresses in service. (6, 7). Thus, mechanical testing of nanostructured materials fabricated by FIB machining allows the investigation of various sample geometries such as micropillar for compression (8, 9), dog-bone shape for tensile tests (10, 11), and cantilevers for bending (12, 13). Free-standing micropillar compression experiments are a promising method to examine the mechanical properties of single crystals of various materials with small

Article History:

Received: 2023/09/25

Accepted: 2024/01/22

Online: 2024/03/31

Correspondence to: Halil Yılmaz,
E-mail: halil.yilmaz@alparslan.edu.tr;
Phone: +90(436) 249 49 49 (2532)

This article has been checked for similarity.



This is an open access article
under the CC-BY-NC licence

<http://creativecommons.org/licenses/by-nc/4.0/>

Cite as:

Yılmaz H, Alkan B, Budak HF. Size Dependent Compressive Strength of FIB Machined Single Crystal Manganese Pillars. Hittite Journal of Science and Engineering 2024;11(1):41-47. doi:10.17350/hjse19030000330

dimensions.

There are numerous reports published on compression experiments of metal nanopillars with diameters less than 5 μm . In all cases, the smaller the sample diameter, the higher the pillar/wire strength. This phenomenon is called size effect dependency. This dependence of strength on specimen size was first reported by Uchic et al. (8), whereby they used a FIB machining and nanomechanical testing device equipped with a flat-ended tip to investigate the in-situ mechanical properties of micron/submicron-sized nickel (Ni) pillars at room temperature (8, 14). They reported some shifts in the stress-strain plots as the pillar diameters varied and found an inverse relationship between yield stress and power of sample size. Consequently, this method has become more attractive and very popular for investigating the size effect dependence of various materials. Moreover, fundamental approaches were tried to understand the size effect dependence and deformation behaviors of small-sized materials and specially focused on different lattice types of materials such as FCC (8, 14-18), BCC (19-23), hexagonal close-packed (HCP) (24, 25), metallic glasses (26-28) and nanocrystalline materials (29). The FCC metal pillars under compression exhibited a universal power-law relation between pillar diameter and strength. The yield stress (σ_y) has an inverse relationship with the variable power of the sample size (d), with a universal empirical correlation:

$$\sigma_y = \sigma_0 + Ad^n \quad (1)$$

where, σ_0 represents a bulk strength, A represents a material constant, and n represents a size effect exponent. For several FCC lattices, the power-law exponents have been typically found to be in the range of -0.6 to -1.0. Dou and Derby compiled the size-dependent strength for several FCC nanowires/pillars (tested in compression) against sample diameter. This was proposed that a universal empirical relation of approximately $n = -0.67$, for equation 1, where $\sigma_0 = 0$ (30).

Equation 1 expresses a similar connection between compressive engineering stress and pillar/wire diameter for BCC metal pillars. However, samples of BCC metal tested under compression exhibit considerable variances in behavior with power-law exponents ranging from -0.15 to -0.8 (19, 21-23, 31-34). It is generally believed that the difference in the behavior between FCC and BCC metals is attributed to the different responses of dislocations in the different lattice structures. In FCC metal pillars, the dislocations are highly mobile, thereby showing similar mobility for edge and screw dislocations and need quite low thermal activation. However, in BCC structures, the coplanar core structure of a screw dislocation causes a higher lattice friction stress (Peierls) and lower mobility when than their edge counter-

parts, thus necessitating a higher level of thermal activation (19, 35, 36). Kishida et. al (37) examined the compression behavior of single crystal α -Mn micropillars with squared cross-sections ranging from 1 to 10.5 μm , against crystal orientation at the room temperature for the first time, and determined the deformation mechanism and critical resolved shear stress (CRSS). They discovered that single crystal manganese pillars deformed plastically due to dislocation motion and reached extremely high flow stresses in the 4.5-6 GPa range. Dislocations glide along [111] and [001] are pointed out to operate in Z-axis orientations near [001] and [111] respectively. Because of the wavy shape of slip planes induced by cross-slip, they were unable to identify the low-indexed planes.

Furthermore, the literature has extensive experimental research on the size-dependent mechanical characteristics of different single-crystal FCC and BCC metals. This suggests the evolution of the size effect, which could be instrumental in this regard. As a result, there is sufficient opportunity to improve understanding of the micromechanical properties of manganese pillars for the whole range of BCC metals size effects mentioned in the literature.

Thus, the purpose of this study is to investigate the size-dependent compressive strength and deformation behavior of single crystals manganese pillars against sample size at ambient temperature using micropillar samples with diameters ranging from ~ 1 to ~ 4.5 μm to deduce the size-dependent strength through evaluating flow stress values.

MATERIALS AND METHODS

Materials Used and Pillar Preparation

A cast polycrystalline pure Mn metal sheet (99.95%) having 2 mm thickness, denoted "as-received" material was provided from Goodfellow Cambridge Ltd. The samples were cut into small squares (10 mm \times 10 mm) and mounted in resin. The sample surface was gradually ground with SiC abrasive grinding papers (from P1200-grit to final grinding with P2000-grit; EU grade). This process was followed by polishing down to $\frac{1}{4}$ μm using diamond pastes in sequence. After that, further finishing was carried out using an active polishing suspension (OP-S) to remove the strain, induced by grinding and polishing operations. The specimen was extracted from the mount and placed onto scanning electron microscopy (SEM) stub for further characterization. Larger grains were selected to generate random orientation samples, which were subsequently processed using a FIB to fabricate micropillars of the desired dimensions.

All single crystal pillars with diameters ranging from ~ 1 μm to ~ 4.5 μm were prepared using FIB from randomly

selected grains of manganese. A free-standing Mn pillar was prepared using a Zeiss Gemini 2 Crossbeam 540 SEM-FIB (Carl Zeiss, Jena, Germany). This instrument was located at the East Anatolia High Technology Application and Research Center (DAYTAM)/Ataturk University. Accelerating voltages of 5 kV and 30 kV were utilized for imaging and machining (preparations), respectively. According to Volkert and Lilleodden's procedure, (38) the nano/micropillar machining process was performed in two stages. The methods and experimental conditions used to fabricate the micropillars have also been explained in detail in our earlier work (23). Briefly, the pillars were prepared using an inner and outer diameter ring pattern design. The radius of the inner and outer rings was set to approximately around 9 μm and 16 μm , respectively. The pillars of different heights were produced by utilizing a variety of dwell times. Depending on the required pillar height, a high flow of gallium (Ga^+) ions applied at the start of the FIB milled a hole around the pillar with a depth ranging from 18-32 μm . An individual Mn pillar was machined (at most $\frac{1}{4}$ of the grain size) from each selected grain in the Mn microstructure. The highest pillar fabricated was around 12.3 μm . Therefore, we chose a grain with around 50 μm to be sure that pillar does not contain any sub-grain or grain boundaries. The aspect ratio was set between 2.8 and 3.8, to avoid buckling deformation at higher pillar heights. This was accomplished by progressively decreasing the FIB current at various machining stages. From a milling point of view, the compression pillars with taper angles ranging from 3° to 5° were obtained. Based on the as-received conditions, the manganese metal only allows to machine/prepare a single pillar from an individual grain. Before the uniaxial compression experiments, the size of each pillar (all diameters and heights) was obtained using images collected with FIB (Zeiss Gemini Crossbeam 540, at 5kV).

Uniaxial Compression Experiments

Uniaxial compression tests on Mn pillars were carried out with the help of an Agilent Technologies Nano Indenter G200 micromechanical testing system (Agilent Technologies, Santa Clara, CA, USA) outfitted with a 15 μm flat punch tip. This instrument was located at Koç University Surface Science and Technology Center (KUYTAM). The compression tests were performed in displacement-rate control mode at a constant nominal displacement rate of 3 nm/s. Stress-strain graphs were created using the load-displacement data. As mentioned in our previous work, the size-dependent strength vs pillar diameter was displayed following standard compressive flow stress at 4% strain (23). This is because there is no uniform engineering strain value in the literature where micropillar compression experiments are reported, and the data are variably given in a 2.5-8% compressive strain range (22, 31, 39, 40).

RESULTS AND DISCUSSION

Microstructure

Several attempts have been made to examine the information about the microstructure of manganese metal sheet using electron backscatter diffraction (EBSD) analysis. It has been discovered that the surface of manganese metal cannot produce a single diffraction pattern. The crystal orientation of the grains could not be identified. Thus, larger grains were chosen at random to produce the manganese pillars. The Mn pillars of varying diameters were machined from randomly selected grains without regard for orientation. Therefore, due to the microstructure of manganese metal, it was impossible to fabricate multiple pillars in one grain. The SEM micrographs of the microstructure and FIB machined micropillars are depicted in Fig. 1 (a-c).

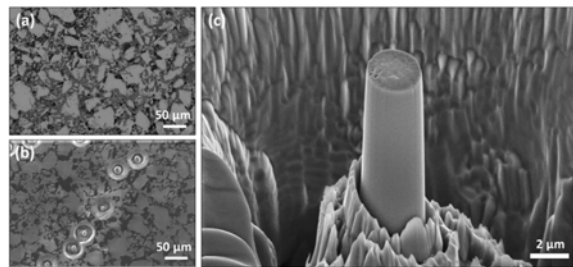


Figure 1. (a) SEM image of polycrystalline manganese metal surface, (b) A view of some micropillars prepared by FIB on the surface of Mn metal, and (c) A representative SEM image of 2.6 μm Mn micropillar in diameter. The image was taken at 54° tilt from the top view.

Crystallographic Slip for Manganese Pillars

Fig. 2 shows typical SEM micrographs of manganese pillars varying in diameter from $\sim 1 \mu\text{m}$ to $\sim 4.5 \mu\text{m}$. These Mn pillars were machined from randomly picked grains and compressed. It should be highlighted that without knowing the grain orientation, we couldn't tell which slip planes were engaged during compression from the chaotic slip bands. There was no substantial variation in deformation behavior between deformed manganese pillars with undetermined orientation. In the top right SEM image in Fig. 2, the clear slip traces are more apparent compared to other SEM images since there is no load controlling option in testing instrument. The testing instrument has only displacement-rate control mode. We were not able to control the load applied. Thus, the applied load was too high for some pillars to identify the slip traces. Also, the orientations of the grains are uncertain, the angle between the loading direction and the normal of the slip plane could not be calculated. In this study, we aimed to investigate the effect of pillar diameter on strength rather than aspect ratio or the effect of length. Researchers tend to give more attention to studying the effect of pillar diameter on the mechanical properties of micro- or nanoscale materials due to its significant influ-

ence, ease of precise control during fabrication (FIB and lithography), and its pronounced size-dependent behaviors in small-scale materials. Variations in pillar diameter often lead to more pronounced size effects in mechanical properties due to high surface-to-volume ratio, which becomes critical at smaller dimensions. Changes in diameter can create significant differences in stress distributions and deformation mechanisms compared to heights variation. For example, changes in diameter can influence the density of defects, stress concentrations, and surface effects (dislocation image force, dislocation starvation mechanism etc.) more prominently than variations in height. (41, 42)

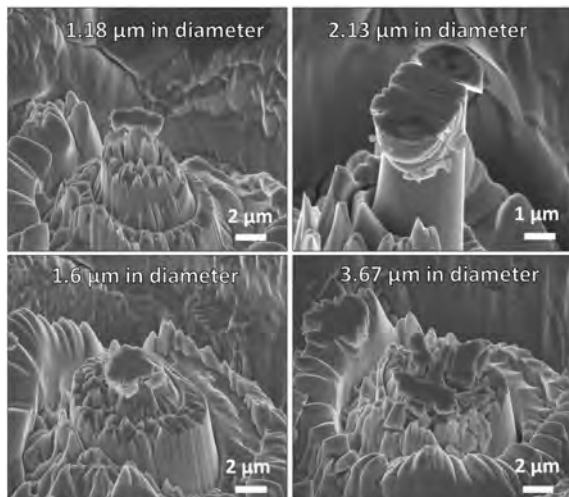


Figure 2. post deformation SEM images of Mn pillars with various diameters. On the surface of the pillars, a chaotic and brittle slip behavior was observed. SEM images were captured and adjusted at 36° from the top view.

Stress-Strain Curves and Size Effect Dependency

Fig. 3 indicates a representative engineering stress-strain plot for randomly selected orientations of manganese pillars with various diameters. This curve clearly showed the influence of sample size on the pillar strength. Since then, the stress has increased as the pillar size has reduced. At 4% strain, the flow stress reached 5.61 GPa for manganese pillars with a diameter of 1182 nm. Due to early plasticity, the yield stress at 0.2% strain is quite difficult to apply in these pillar experiments. Therefore, we have chosen a fixed strain (4%) in our pillar study. At 4% strain, the stress of the largest manganese pillar (4460 nm) was 4.53 GPa. The stress-strain plot for manganese metal shows a period of indistinct yield onset followed by strain hardening up to 10% strain. In general, the stress-strain curves of all tested manganese pillars showed high work hardening and smooth flow behavior, typically with strains up to 8-10%. However, the flow stresses remained constant without work hardening after 10% strain. No significant difference was found in the stress-strain be-

havior of all Mn pillars tested in unknown orientations. When compared to other BCC metallic pillars examined in the literature, the Mn pillars demonstrated considerably greater engineering stresses at 4% strain for a given diameter. The Mn pillars showed relatively higher engineering stresses for a specific diameter compared to other BCC metallic pillars tested in the literature (19, 22, 23, 34, 40). Our stress-strain results agree with previously reported only single study on Mn pillars, confirming that higher stresses (ranging between 4-6 GPa) are reached for all orientations. The steepness in linear region in stress-strain behavior of Mn pillars was also observed similar in previously reported study on Mn pillars (37).

A possible explanation for the higher strength could be related to the arbitrary chosen orientations leading to non-uniform slip behavior and the unknown Schmid factor causing higher stress values than other metallic pillars reported in the literature. The local dislocation density in the Mn sample was not measured. However, the metal specimen displayed homogeneous and isotropic grain shapes. Thus, we conclude that the local dislocation densities were not too high to strongly influence our experiments and arguments.

The effect of pillar size on strain hardening rate (SHR) lowers as pillar diameter increases. The SHR data was derived as the mean gradient of the stress-strain curve between 4% and 10% strain, which is consistent with earlier compression investigations (see Fig. 4). (19, 21, 23, 40, 43). The SHR data was precisely identified through data extraction using data reader function in the Origin Lab software. Although some scatter was observed in the SHR data, indications of a size effect were discernible. The tests conducted on a larger number of pillars will reduce the observed data scatter. Our analysis did not identify error bars or ranges in the SHR data. Experiments using Mn pillars with known orientation must be repeated to determine why the flow stress and SHR were too high. Further research into the size-dependent mechanical behaviors of Mn pillars with known orientation is required to offer a statistically confirmed stress-strain curves to detect the active slip system and a more precise size effect exponent. Maintaining consistent fabrication processes for pillar fabrication, specifically in terms of uniform diameters, alongside constant testing parameters, is anticipated to comparable stress-strain, SHR data, and size effect exponents. Repetition of these experiments is expected to yield results consistent with this expectation.

Fig. 5 depicts the stress at 4% strain as a logarithmic curve vs pillar diameter. Linear interpolation was used to get the size effect exponent for the Mn pillars. As observed with the randomly oriented Mn pillars, there is a less apparent size effect, with flow stress increasing as pillar size decreases. The size effect exponent for Mn pillars was found

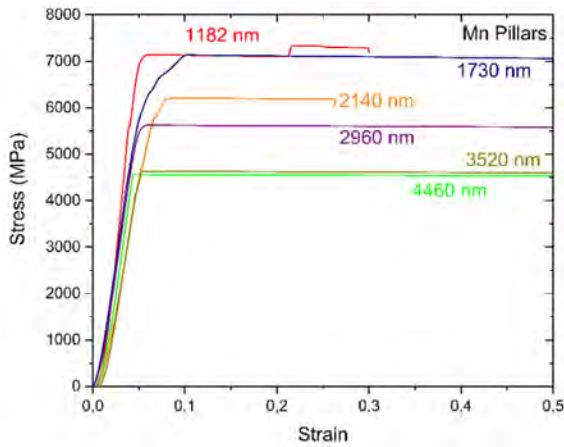


Figure 3. Typical stress-strain curves for compression tests conducted on Mn pillars

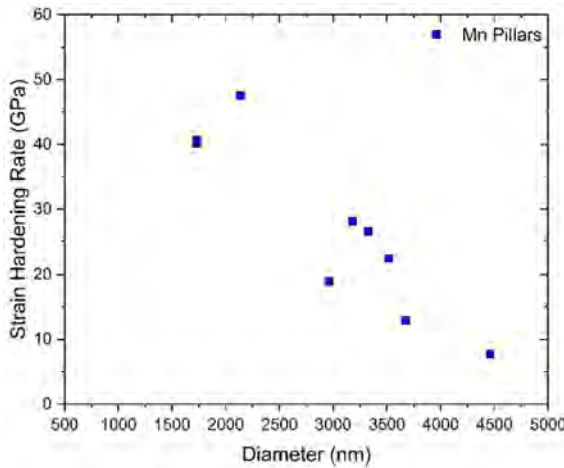


Figure 4. The relationship between strain hardening rate and manganese pillar diameters under compression.

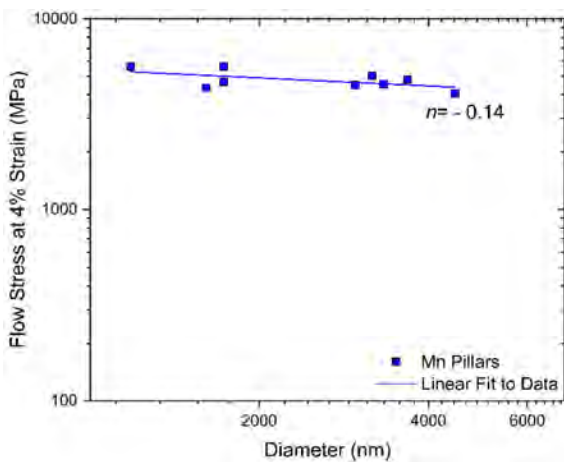


Figure 5. Logarithmic plot of engineering stress (at 4% strain) vs pillar diameter for compression tested Mn micropillars. The blue line represents a linear fit to the Mn data.

to be -0.14. According to the literature, the size exponents for BCC metals range between -0.1 and -0.8. The power law exponent of the Mn pillars agrees with prior research

on the BCC pillars. (19, 32, 34, 44). Kishida and colleagues (37) investigated how single crystal α -Mn micropillars with diameters ranging from 1 to 10.5 μm responded to compression testing concerning their crystal orientation. However, there does not appear to be a significant effect on yield stress due to sample size variations across the orientations studied. There is always uncertainty in determining the precise orientation of each pillar, which might cause variation in size effect data. Table 1 presents data from various reports on micropillars tests on several BCC metals.

Table 1. Data for the stress-size exponent, n , micro compression data with BCC metal pillars tested at ambient temperature.

Material	Pillar Orientation	Active Slip System	n	Plastic Strain	Ref.
Mn	Random Orientations	Unknown	-0.14	4%	This work
Fe	[001]	{101}<111>	-0.58	4%	(23)
Fe	[110]	{101}<111>	-0.61	4%	(45)
Fe	[123]	{101}<111>	-0.63	4%	(45)
V	[001]	{101}<111>	-0.56	4%	(23)
Nb	[001]	{101}<111>	-0.58	4%	(23)
Ta	[001]	{101}<111>	-0.4	4%	(44)
W	[111]	{101}<111>	-0.23	4%	(44)
Mo	[111]	{101}<111>	-0.37	4%	(44)

CONCLUSION

Single crystal manganese micropillars with randomly chosen crystallographic orientations were fabricated by FIB from a polycrystalline sample (varying in diameter from 1000-4500 nm) and deformed to measure their stress at 4% strain and deformation behavior. The following are the final thoughts:

- As the diameter of the manganese pillars decreased, the deformation behavior stayed constant and followed the same pattern. We were unable to discover an active slip mechanism due to the randomly picked grains.
- The stress-strain curves show that the flow stresses were higher compared to other BCC metals at specific diameters in the literature.
- The manganese pillars exhibited a less pronounced size effect, i.e. strength increased as pillar size decreased, resulting in a size effect exponent (n) of -0.14.
- Furthermore, the manganese pillars demonstrated strain hardening up to 10%, which increased as the pillar diameter decreased.

ACKNOWLEDGEMENT

This work was supported by Mus Alparslan University Scientific Research Project (BAP) of Mus Alparslan University under a project number of BAP-20-TBMY-4901-02.

We would like to thank the Eastern Anatolia High Technology Application and Research Center (DAYTAM) for access to the SEM and FIB.

CONFLICT OF INTEREST

Authors approve that to the best of their knowledge, there is not any conflict of interest or common interest with an institution/organization or a person that may affect the review process of the paper.

AUTHOR CONTRIBUTION

Halil Yilmaz: Conceptualization, Methodology, Investigation, Writing- original draft

Bulent Alkan: Investigation, Writing-review

Hasan Feyzi Budak: Methodology, Writing- review and editing

REFERENCES

1. Matricardi LR, Downing J. Manganese and manganese alloys. Kirk-Othmer Encyclopedia of Chemical Technology. 2000.
2. Sully A, Senderoff S. Manganese, Metallurgy of the Rarer Metals, Number 3. J Electrochem Soc. 1955;102(10):255Ca.
3. Verhoeven JD. Steel metallurgy for the non-metallurgist: ASM International; 2007. 220 p.
4. Martha S, Markovsky B, Grinblat J, Gofer Y, Haik O, Zinigrad E, et al. LiMnPO₄ as an advanced cathode material for rechargeable lithium batteries. J Electrochem Soc. 2009;156(7):A541.
5. Meaden GT. The general physical properties of manganese metal. Metallurgical Reviews. 1968;13(1):97-114.
6. Stelmashenko N, Walls M, Brown L, Milman YV. Microindentations on W and Mo oriented single crystals: an STM study. Acta Mater. 1993;41(10):2855-65.
7. Zhu T, Bushby A, Dunstan D. Materials mechanical size effects: a review. Mater Sci Technol. 2008;23(4):193-209.
8. Uchic MD, Dimiduk DM, Florando JN, Nix WD. Sample dimensions influence strength and crystal plasticity. Science. 2004;305(5686):986-9.
9. Greer JR, Oliver WC, Nix WD. Size dependence of mechanical properties of gold at the micron scale in the absence of strain gradients. Acta Mater. 2005;53(6):1821-30.
10. Kim J-Y, Greer JR. Tensile and compressive behavior of gold and molybdenum single crystals at the nano-scale. Acta Mater. 2009;57(17):5245-53.
11. Kiener D, Grosinger W, Dehm G, Pippan R. A further step towards an understanding of size-dependent crystal plasticity: In situ tension experiments of miniaturized single-crystal copper samples. Acta Mater. 2008;56(3):580-92.
12. Chen C, Pei Y, De Hosson JTM. Effects of size on the mechanical response of metallic glasses investigated through in situ TEM bending and compression experiments. Acta Mater. 2010;58(1):189-200.
13. Iqbal F, Ast J, Göken M, Durst K. In situ micro-cantilever tests to study fracture properties of NiAl single crystals. Acta Mater. 2012;60(3):1193-200.
14. Dimiduk D, Uchic M, Parthasarathy T. Size-affected single-slip behavior of pure nickel microcrystals. Acta Mater. 2005;53(15):4065-77.
15. Frick C, Clark B, Orso S, Schneider A, Arzt E. Size effect on strength and strain hardening of small-scale [111] nickel compression pillars. Mater Sci Eng A. 2008;489(1):319-29.
16. Ng K, Ngan A. Stochastic nature of plasticity of aluminum micropillars. Acta Mater. 2008;56(8):1712-20.
17. Kiener D, Motz C, Dehm G. Micro-compression testing: A critical discussion of experimental constraints. Mater Sci Eng A. 2009;505(1):79-87.
18. Kiener D, Motz C, Dehm G. Dislocation-induced crystal rotations in micro-compressed single crystal copper columns. J Mater Sci. 2008;43(7):2503-6.
19. Schneider AS, Kaufmann D, Clark BG, Frick CP, Gruber PA, Mönig R, et al. Correlation between critical temperature and strength of Small-Scale bcc pillars. Phys Rev Lett. 2009;103(10):105501.
20. Rogne BRS, Thaulow C. Effect of crystal orientation on the strengthening of iron micro pillars. Mater Sci Eng A. 2015;621:133-42.
21. Kaufmann D, Mönig R, Volkert C, Kraft O. Size dependent mechanical behaviour of tantalum. Int J Plast. 2011;27(3):470-8.
22. Kim J-Y, Jang D, Greer JR. Tensile and compressive behavior of tungsten, molybdenum, tantalum and niobium at the nanoscale. Acta Mater. 2010;58(7):2355-63.
23. Yilmaz H, Williams CJ, Risan J, Derby B. The size dependent strength of Fe, Nb and V micropillars at room and low temperature. Mater. 2019;7:100424.
24. Shan Z. In situ TEM investigation of the mechanical behavior of micronanoscaled metal pillars. JOM. 2012;64(10):1229-34.
25. Prasad KE, Rajesh K, Ramamurty U. Micropillar and macropillar compression responses of magnesium single crystals oriented for single slip or extension twinning. Acta Mater. 2014;65:316-25.
26. Mridha S, Arora HS, Lefebvre J, Bhowmick S, Mukherjee S. High temperature in situ compression of thermoplastically formed nanoscale metallic glass. JOM. 2017;69(1):39-44.
27. Shan Z, Li J, Cheng Y, Minor A, Asif SS, Warren O, et al. Plastic flow and failure resistance of metallic glass: Insight from in situ compression of nanopillars. Phys Rev B. 2008;77(15):155419.
28. Dubach A, Raghavan R, Löffler JF, Michler J, Ramamurty U. Micropillar compression studies on a bulk metallic glass in different structural states. Scripta Mater. 2009;60(7):567-70.
29. Cheng GM, Jian WW, Xu WZ, Yuan H, Millet PC, Zhu YT. Grain size effect on deformation mechanisms of nanocrystalline bcc metals. Mater Res Lett. 2012;1(1):26-31.
30. Dou R, Derby B. A universal scaling law for the strength of metal micropillars and nanowires. Scripta Mater. 2009;61(5):524-7.
31. Rogne B, Thaulow C. Strengthening mechanisms of iron micropillars. Philos Mag. 2015;95(16-18):1814-28.
32. Huang R, Li Q-J, Wang Z-J, Huang L, Li J, Ma E, et al. Flow stress in submicron BCC iron single crystals: sample-size-dependent strain-rate sensitivity and rate-dependent size strengthening. Mater Res Lett. 2015;3(3):121-7.
33. Han SM, Feng G, Jung JY, Jung HJ, Groves JR, Nix WD, et al. Critical-temperature/Peierls-stress dependent size effects in body centered cubic nanopillars. Appl Phys Lett. 2013;102(4):041910.
34. Lee S-W, Cheng Y, Ryu I, Greer J. Cold-temperature deformation of nano-sized tungsten and niobium as revealed by in-situ nano-mechanical experiments. Science China Technological Sciences. 2014;57(4):652-62.
35. Seeger A. Peierls barriers, kinks, and flow stress: Recent progress: Dedicated to Professor Dr. Haël Mughrabi on the occasion of his 65th birthday. Z Metallk. 2002;93(8):760-77.

36. Christian J. Some surprising features of the plastic deformation of body-centered cubic metals and alloys. *Metall Trans A*. 1983;14(7):1237-56.
37. Kishida K, Suzuki H, Okutani M, Inui H. Room-temperature plastic deformation of single crystals of α -manganese-hard and brittle metallic element. *Int J Plast*. 2023;160:103510.
38. Volkert CA, Lilleodden ET. Size effects in the deformation of sub-micron Au columns. *Philos Mag*. 2006;86(33-35):5567-79.
39. Schneider A, Clark B, Frick C, Gruber P, Arzt E. Effect of orientation and loading rate on compression behavior of small-scale Mo pillars. *Mater Sci Eng A*. 2009;508(1):241-6.
40. Torrents Abad O, Wheeler JM, Michler J, Schneider AS, Arzt E. Temperature-dependent size effects on the strength of Ta and W micropillars. *Acta Mater*. 2016;103:483-94.
41. Greer JR, Nix WD. Nanoscale gold pillars strengthened through dislocation starvation. *Phys Rev B*. 2006;73(24):245410.
42. Greer JR, De Hosson JTM. Plasticity in small-sized metallic systems: Intrinsic versus extrinsic size effect. *Prog Mater Sci*. 2011;56(6):654-724.
43. Kim J-Y, Greer JR. Size-dependent mechanical properties of molybdenum nanopillars. *Appl Phys Lett*. 2008;93(10):101916.
44. Yilmaz H. Mechanical properties of body-centred cubic nanopillars [PhD Thesis]: University of Manchester (Manchester, UK); 2018.
45. Yilmaz H, Williams CJ, Derby B. Size effects on strength and plasticity of ferrite and austenite pillars in a duplex stainless steel. *Mater Sci Eng A*. 2020;793:139883.